

CONFERENCE PROCEEDINGS

4th International Conference on Nanomaterials Science and Mechanical Engineering

**University of Aveiro
Portugal
July 6-9, 2021**



tema

university of aveiro

centre for mechanical technology and automation

CONFERENCE PROCEEDINGS

4th International Conference on Nanomaterials Science and Mechanical Engineering

**University of Aveiro
Portugal
July 6-9, 2021**



tema

university of aveiro

centre for mechanical technology and automation

Title

4th International Conference on Nanomaterials Science and Mechanical Engineering
Conference proceedings

Editors

Igor Bdikin
Gil Alberto Batista Gonçalves
Gonzalo Guillermo Otero Irurueta
Raul Simões

Publisher

UA Editora
Universidade de Aveiro

1st edition – September 2021

ISBN

978-972-789-707-0

DOI

<https://doi.org/10.48528/mp33-sh54>

Table of Contents

Table of Contents.....	4
Committees.....	6
CONFERENCE PROCEEDINGS PAPERS.....	8
Micro Electrical Discharge Machining μEDM: Analysis of the influence of geometrical, physical and electrical parameters on the machining performances.....	9
Conjugated poly(platina-yne)s for new materials applications.....	19
Effect of long baffles on forced convection heat transfer over multiple heated blocks.....	23
Use of infrared temperature sensor to estimate the evolution of transformation temperature of SMA actuator wires.....	31
Free vibration analysis of rotating single walled carbon nanotubes resting in elastic medium.....	34
Modeling and computational study of structures and physical properties of hydroxyapatite containing various defects: a review.....	42

The conference (4th International Conference on Nanomaterials Science and Mechanical Engineering, University of Aveiro, Portugal, July 6-9, 2021) looks for significant Modern Problems of Nanomaterials Science and Mechanical Engineering, to provide a platform to the global researchers and practitioners from both academia as well as industry to meet and share cutting-edge development in the fields, to give possibility for young scientists and students present results and find your place in the future world.

Organizing Committee ICNMSME2021

Prof. Dr. Robertt Angelo Fontes Valente (UA, Portugal)

Prof. Dr. Vítor António Ferreira da Costa (UA, Portugal)

Prof. Dr. António Manuel de Bastos Pereira (UA, Portugal)

Prof. Dr. Paula Alexandrina de Aguiar Pereira Marques (UA, Portugal)

Dr. Duncan Paul Fagg (UA, Portugal)

Dr. Igor Bdikin (UA, Portugal)

Dr. Gonzalo Guillermo Otero Irurueta (UA, Portugal)

Dr. Gil Alberto Batista Gonçalves (UA, Portugal)

Committees

Organizing Committee:

Prof. Dr. Robertt Angelo Fontes Valente

University of Aveiro, Portugal, Email: robertt@ua.pt

Prof. Dr. Vítor António Ferreira da Costa

University of Aveiro, Portugal, Email: v.costa@ua.pt

Prof. Dr. António Manuel de Bastos Pereira

University of Aveiro, Portugal, Email: abastos@ua.pt

Prof. Dr. Paula Alexandrina de Aguiar Pereira Marques

University of Aveiro, Portugal, Email: paulam@ua.pt

Dr. Duncan Paul Fagg

University of Aveiro, Portugal, Email: duncan@ua.pt

Dr. Igor Bdikin

University of Aveiro, Portugal, Email: bdikin@ua.pt

Dr. Gonzalo Guillermo Otero Irurueta

University of Aveiro, Email: otero.gonzalo@ua.pt

Dr. Gil Alberto Batista Gonçalves

University of Aveiro, Email: ggoncalves@ua.pt

Programme Committee:

Prof. Dr. Alfredo Manuel Balacó de Moraes (UA, Portugal)

Prof. Dr. Alexander N. Titov (Institute of Metal Physics, Russia)

Dr. Aliaksandr Shaula (UA, Portugal)

Prof. Dr. António Gil D'orey de Andrade Campos (UA, Portugal)

Prof. Dr. António Manuel de Amaral Monteiro Ramos (UA, Portugal)

Prof. Dr. António Manuel de Bastos Pereira (UA, Portugal)

Prof. Dr. António Manuel Godinho Completo (UA, Portugal)

Dr. Bagautdinov Bagautdin (JASRI/SPRING-8, Japan)

Prof. Dr. Binay Kumar (University Delhi, India)

Prof. Dr. Budhendra Singh (Central University of South Bihar, India)

Prof. Dr. Carlos Alberto Moura Relvas (UA, Portugal)

Prof. Dr. Dmitry Karpinsky (SPMRC NASB, Belarus)

Prof. Dr. Dmitry Kiselev (MISiS, Russia)

Dr. Duncan Paul Fagg (UA, Portugal)

Prof. Dr. Fernando José Neto da Silva (UA, Portugal)

Prof. Dr. Francisco José Malheiro Queirós de Melo (UA, Portugal)

Dr. Frédéric Gérard Barlat (UA, Portugal)

Dr. Gil Alberto Batista Gonçalves (UA, Portugal)

Dr. Gonzalo Guillermo Otero Irurueta (UA, Portugal)

Dr. Igor Bdikin (UA, Portugal)

Dr. Isabel Maria Alexandrino Duarte (UA, Portugal)

Prof. Dr. João Paulo Davim Tavares da Silva (UA, Portugal)

Prof. Dr. Joaquim Alexandre Mendes de Pinho da Cruz (UA, Portugal)

Prof. Dr. Jorge Augusto Fernandes Ferreira (UA, Portugal)

Prof. Dr. José Paulo Oliveira Santos (UA, Portugal)
Prof. Dr. Manoj Kumar Singh (JAIN University, India)
Prof. Dr. Margarida Isabel Cabrita Marques Coelho (UA, Portugal)
Prof. Dr. Maxim Silibin (MIET, Russia)
Prof. Dr. Mónica Sandra Abrantes de Oliveira Correia (UA, Portugal)
Prof. Dr. Nelson Amadeu Dias Martins (UA, Portugal)
Prof. Dr. Nikolai Sobolev (UA, Portugal)
Prof. Dr. Paula Alexandrina de Aguiar Pereira Marques (UA, Portugal)
Prof. Dr. Philip R. LeDuc (CMECS, USA)
Dr. Pukazh Selvan Dharmakkon (UA, Portugal)
Prof. Dr. Ricardo José Alves de Sousa (UA, Portugal)
Prof. Dr. Rui António da Silva Moreira (UA, Portugal)
Prof. Dr. Sergei Bozhko (ISSP, Russia)
Prof. Dr. Svetlana G. Titova (Institute of Metallurgy, Russia)
Prof. Dr. Vítor António Ferreira da Costa (UA, Portugal)
Prof. Dr. Vítor Manuel Ferreira dos Santos (UA, Portugal)
Prof. Dr. Vladimir Bystrov (IMPB-KIAM RAS, Russia)

Editorial Board:

Dr. Igor Bdikin (UA, Portugal)
Dr. Gil Alberto Batista Gonçalves (UA, Portugal)
Dr. Gonzalo Guillermo Otero Irurueta (UA, Portugal)
Raul Simões (UA, Portugal)

Technical Program Committee:

Dr. Duncan Paul Fagg (UA, Portugal)
Prof. Dr. Paula Alexandrina de Aguiar Pereira Marques (UA, Portugal)
Dr. Igor Bdikin (UA, Portugal)
Dr. Gonzalo Guillermo Otero Irurueta (UA, Portugal)
Dr. Gil Alberto Batista Gonçalves (UA, Portugal)
Dr. Sergey Mikhalev (UA, Portugal)
Dr. Pukazh Selvan Dharmakkon (UA, Portugal)
Raul Simões (UA, Portugal)

Conference Contacts

TEMA-icnmsme2021.aveiro@ua.pt

Telephone: +351 234 370 830

Conference Web

<http://icnmsme2021.web.ua.pt/>

CONFERENCE PROCEEDINGS PAPERS

Micro Electrical Discharge Machining μ EDM: Analysis of the influence of geometrical, physical and electrical parameters on the machining performances

Asmae Taфраouti *, Yasmina Layouni

Univ Lyon, Université Claude Bernard Lyon 1, CNRS, INSA Lyon, Ecole Centrale de Lyon, CPE Lyon,
INL, UMR5270, 69622 Villeurbanne, France

* Corresponding authors, E-mail: asmae.taфраouti@univ-lyon1.fr; yasmina.layouni@univ-lyon1.fr

Abstract

Micro Electrical Discharge Machining (μ EDM), also known as Micro Electrical Discharge Machining milling, is a non-contact machining technique for conductive and semiconductor materials. It is mainly adapted to machine hard materials. The principle of this process is the creation of electrical discharges between the micro-tool and the workpiece, the both are immersed in a dielectric. μ EDM is a complementary process to mechanical, laser micromachining, and silicon microtechnology techniques (RIE, DRIE, LIGA). This last one can reach a resolution of 50 nm, but they require the use of the cleanroom, so they are not suitable to be used in industry. However, the μ EDM milling resolution is limited to 20 μ m [1] because this process depends on several physical, geometrical, and/or electrical parameters. The goal of this paper is to characterize the electrical discharges obtained during μ EDM machining and to study the effect of several parameters, such as the micro-tool diameter (Φ), the applied voltage (V_{EE}) and the gap (the distance between the two electrodes) on the average discharges energy and the machined volume. The experimental results will be used to characterize the optimal parameters that provide a possibility to reach a machining resolution of 5 μ m.

From the results obtained in this study, we have concluded that the electric field is in the same order whatever the micro-tool diameter, it is equal to 6V/ μ m. This value determines the breakdown gap for a specific applied voltage. Concerning the average discharges energy, it is almost identical for the different micro-tools diameter ($\Phi=20\mu\text{m}$; $\Phi=40\mu\text{m}$; $\Phi=125\mu\text{m}$; $\Phi=250\mu\text{m}$). It depends only on the applied voltage and it is equal to $E=8\ \mu\text{J}$; $E=15\ \mu\text{J}$; $E=30\ \mu\text{J}$ for an applied voltage of $V_{EE} = 25\text{V}$; $V_{EE} = 50\text{V}$; $V_{EE} = 75\text{V}$ respectively.

Keywords: Micro EDM, Electrical discharges, Average discharges energy, Machined volume

1. INTRODUCTION

The microfabrication techniques are widely used in several applications: medical components [1], micro parts and molds [2], microfluidic [3], microelectronics [4], etc. They are based, generally, on mechanical or laser micromachining techniques, or others from silicon microtechnology (RIE, DRIE, LIGA). The Micro Electrical Discharge Machining μ EDM is a complementary process. It is based on the use of a cylindrical micro-tool that runs along a predefined pattern to machine a workpiece electrode. Two electrodes are immersed in a dielectric with a gap of a few micrometers [5]. The application of a voltage between the two electrodes leads to the generation of electrical discharges able to remove material from the

two electrodes. A positive polarization leads to remove material from the workpiece electrode and reduce the wear of the micro-tool electrode [1]. In order to have a high-resolution machining and a good surface condition, it is necessary to understand the effect of each parameter (micro-tool diameter, breakdown gap, applied voltage, dielectric, and capacitor) on the average discharges energy, the removed volume, and the shape of the final crater.

2. EXPERIMENTAL

2.1. Test bench

In all our experiments, we use the generator represented in Figure 1 where the capacitor C_c charges through R_c to the voltage V_{EE} and discharges through the plasma resistance during the breakdown. The charging and discharging voltage across the capacitor depend on the physical conditions during plasma creation. An oscilloscope is used to record, in real-time, the voltage and current points during the plasma breakdown (discharges) for the entire machining process. The micro-tool electrode used during machining is made of Tungsten (99.95%) [6] because it has a high melting temperature ($T=3695\text{ }^\circ\text{C}$) [1], which reduces the wear rate of the micro-tool electrode during machining. Also, it has good thermal conductivity, which allows the heat to dissipate quickly. While we use stainless steel for the workpiece electrode because it has a low melting temperature ($T=1510\text{ }^\circ\text{C}$) [1] and low thermal diffusivity which provides the diffusion of the discharge energy locally. The resolution of the machining, in-depth and width, depends on the micro-tool diameter. In our experiments, we fabricate micro-tools by electrochemical etching [1, 5]. They are cylindrical with a high aspect ratio which help us to achieve high resolution during machining.

Before machining, we polish the workpiece by a mechanical process, where several seed papers of different sizes are used. The goal of this step is to obtain a workpiece with low roughness and a shiny surface.

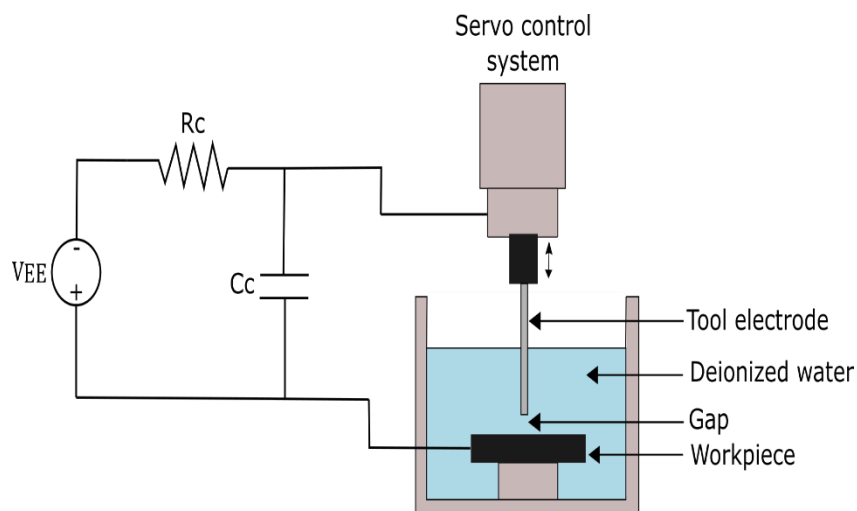


Figure 1. Micro Electrical Discharge Machining bench.

2.2. Protocol used in experiments

To characterize the discharges during machining, we have set up a protocol that allows to determine:

- the breakdown gap, in order to machine with the same gap value
- the average discharges energy
- the removed volume

2.2.1. Determination of the initial gap

Before a workpiece machining, we perform a preliminary step that allows us to know the breakdown gap in given conditions. The goal is to ensure that for the same machining conditions the initial gap between the two electrodes is the same. To do this, we follow the steps described in (Figure 2): (1) Apply, in air, a voltage of 1V between the two electrodes, (2) move down the micro-tool electrode with a step of 1 μm until mechanical/electrical contact is detected. (3) Move up the micro-tool electrode by a distance of 40 μm , this is the reference. At this distance, we have no discharge (no plasma creation for machining voltage $V_{EE} < 75\text{V}$ and micro-tool diameter $\Phi < 250 \mu\text{m}$). Once the reference is determined, we apply a voltage between the micro-tool and the workpiece (example: $V_{EE} = 25\text{V}$), after that, we add deionized water, and we move down the micro-tool, with the help of a piezoelectric, by a step of 1 μm until the creation of the plasma (breakdown or implosion of the plasma: series of discharges occur and extinguish after a lapse of time - a few seconds).

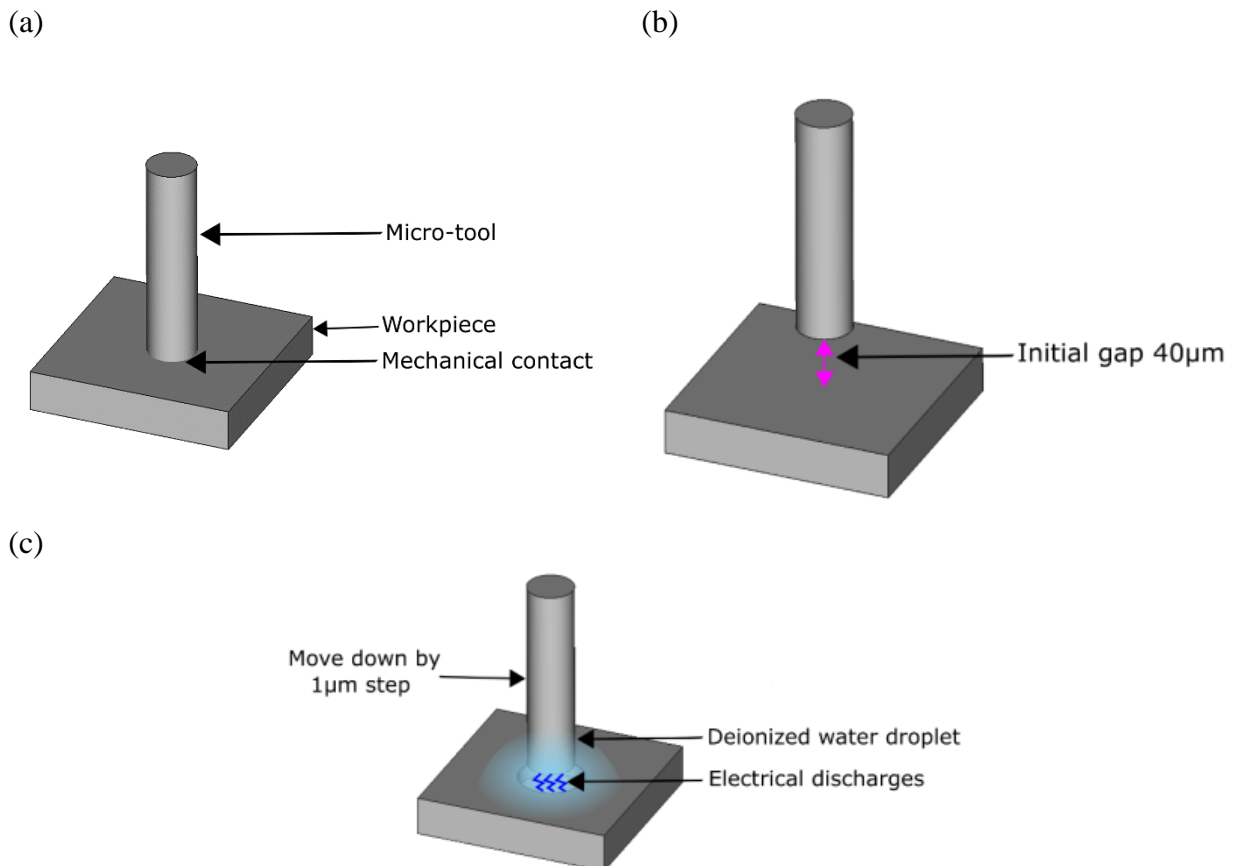


Figure 2. Process of the gap determination (a) Mechanical contact; (b) Move up the micro-tool with a distance of 40 μm ; (c) move down the micro-tool by 1 μm step.

The implosion of the plasma causes a local fusion of the material on the workpiece surface, forming a small crater. The gap is no longer the same, and we have no more discharges. Once the discharges disappear, we turn off the generator and rinse the debris with deionized water to evacuate the removed material and clean the micro-tool electrode. In the end, the micro-tool is moved up for a certain distance. The experiment is repeated 3 times in order to validate the reproducibility of the experiments.

2.2.2. Calculation of the average discharges energy

Figure 3 represents an example of a series of discharges when a voltage of 75V was applied. The average discharges energy is calculated, with the help of a script under Matlab, using eq.1. The discharges taken into account during our calculations are the discharges where the current is higher than 50mA (Figure 3b); because these discharges have higher energy than others where the energy is just some nJ (Figure 3a), and they appear before the breakdown, they are known as "streamers" [1].

$$E_{\text{average}} = \frac{\int_{t_{\text{min}}}^{t_{\text{max}}} U(t) * I(t) dt}{\text{Number of discharges}} \quad (1)$$

2.2.3. Calculation of the removed volume

To determine the crater depth according to its width, we used a profilometer. It lets us know the volume of the removed material for each crater. To simplify the calculation, we consider that the crater has the shape of a truncated cone.

$$V_{\text{removed}} = \pi \int_{z_{\text{min}}}^{z_{\text{max}}} R(z)^2 dz \quad (2)$$

$R(z)$ is the circle radius.

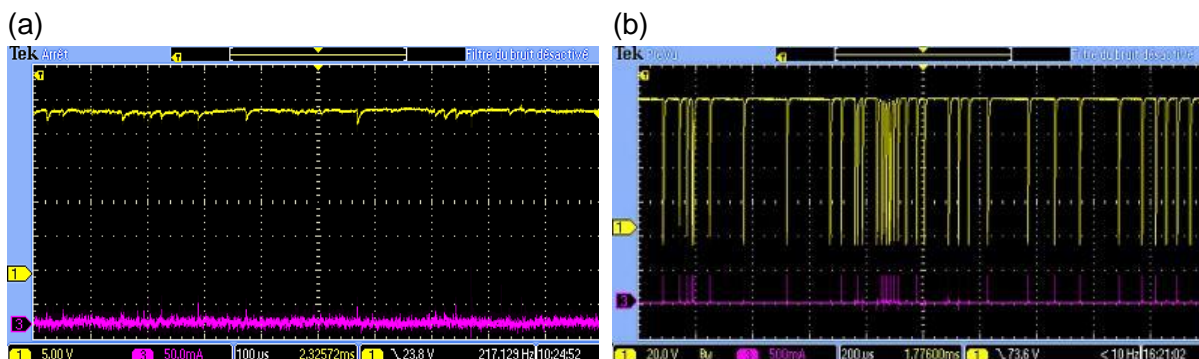


Figure 3. Series of discharges for an applied voltage of: (a) $V_{EE} = 25V$ et $C=10nF$ (streamers case); (b) $V_{EE} = 75V$ et $C=10nF$ (big discharges case).

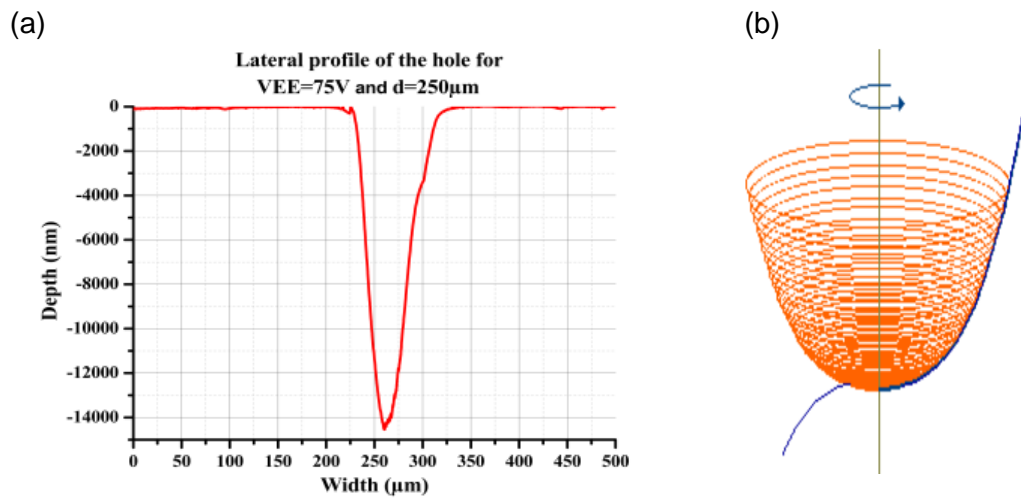


Figure 4. (a) crater profile after the first breakdown for: $V_{EE} = 75V$ and $\Phi=250 \mu\text{m}$, (b) the crater shape used to estimate the removed volume

2.2.4. Machining conditions

To study the effect of certain parameters on the average discharges energy and the removed volume, we have done several experiments. The machining conditions are summarized in Table 1.

Table 1. Machining conditions.

Electrical parameters	Geometric and physical parameters
$V_{EE} = 25V$; $V_{EE} = 50V$; $V_{EE} = 75V$	Tungsten micro-tool diameter: $\Phi=250 \mu\text{m}$; $\Phi=125 \mu\text{m}$; $\Phi=40 \mu\text{m}$; $\Phi=20 \mu\text{m}$
$C_c = 10 \text{ nF}$	Steel workpiece: 20 mm x 20 mm x 0,5 mm
$R_c = 500\Omega$	Deionized workpiece; gap

3. RESULTS & DISCUSSION

3.1. Breakdown gap

Using the protocol described in section 2.2.1, we have determined the breakdown gap for the applied voltages ($V_{EE} = 25V$; $V_{EE} = 50V$; $V_{EE} = 75V$). It is equal to $5\mu\text{m}\pm 1\mu\text{m}$; $10\mu\text{m}\pm 2\mu\text{m}$; $15\mu\text{m}\pm 2\mu\text{m}$ whatever the micro-tool diameter.

Figure 5 illustrates the variation of the electric field according to the micro-tool diameter, the electric field is quasi-constant, it is equal to $6V/\mu\text{m}$. From this figure, we can deduce the breakdown gap for any applied voltage.

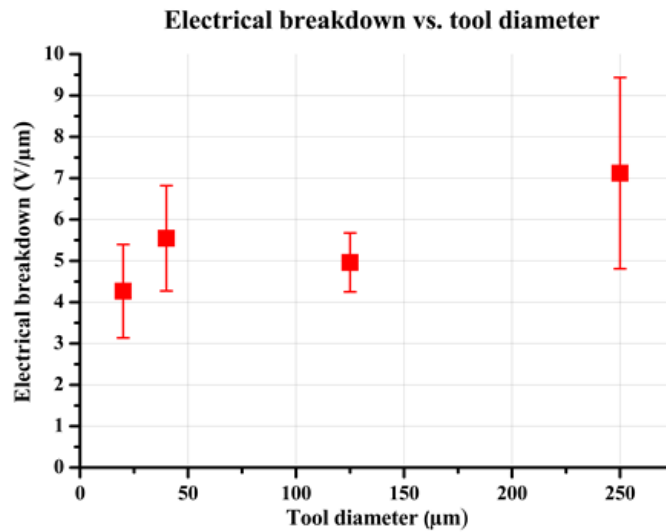


Figure 5. Variation of the electrical breakdown according to the micro-tool diameter.

3.1. Average discharges energy

In order to know the variation of the average discharges energy according to the micro-tool diameters, we have done three experiments under the same conditions at different applied voltages ($V_{EE} = 25V$; $V_{EE} = 50V$; $V_{EE} = 75V$) for each micro-tool diameter.

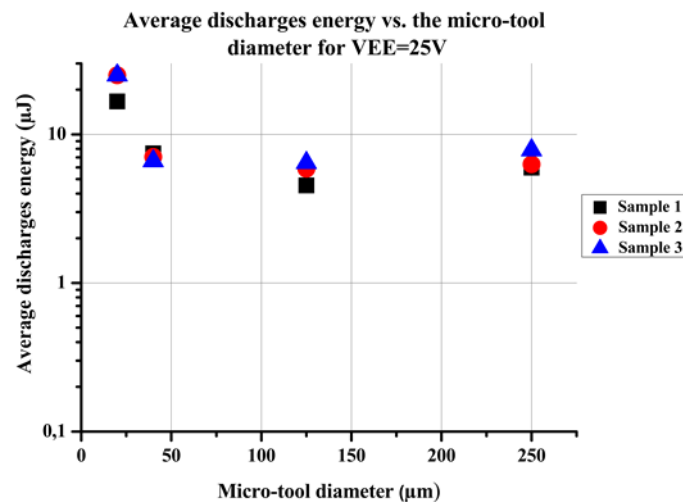


Figure 6. Average discharges energy for $V_{EE} = 25V$; $C=10nF$ and $gap=5\mu m \pm 1\mu m$.

Figure 6 represents the average discharges energy for different diameters (20μm; 40μm; 125μm; 250μm) and an applied voltage of $V_{EE} = 25V$. We can conclude that the average discharges energy is equal to $E_{moyenne} = 8\mu J$ and it does not depend on the micro-tool diameter.

For $V_{EE} = 50V$, it is around $E_{average} = 15\mu J$ (Figure 7), it also does not depend on the micro-tool diameter. The average discharges energy has doubled compared to the one obtained for an applied voltage of $V_{EE} = 25V$ because the electric field is also twice bigger.

Figure 8 shows the average discharges energy obtained for $V_{EE} = 75V$, it is around $E_{moyenne} = 15\mu J$ whatever the micro-tool diameter.

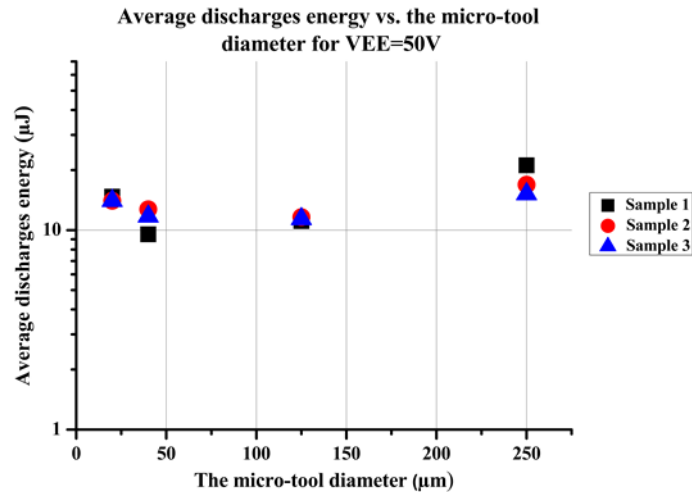


Figure 7. Average discharges energy for $V_{EE} = 50V$; $C=10nF$ and $gap=10\mu m \pm 2\mu m$.

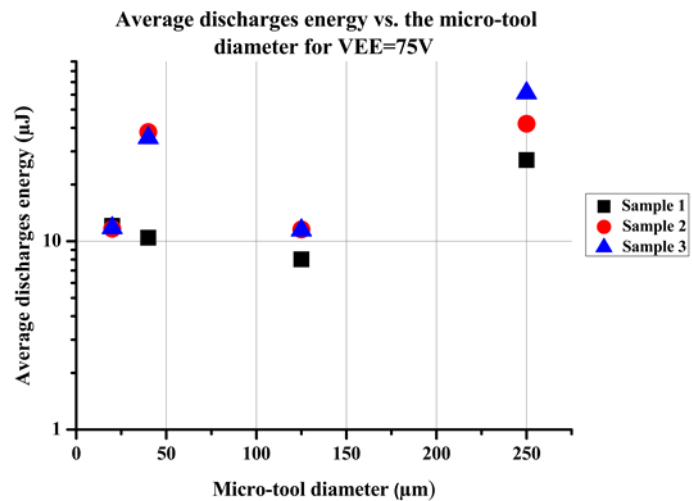


Figure 8. Average discharges energy for $V_{EE} = 75V$; $C=10nF$ and $gap=15\mu m \pm 2\mu m$.

3.2. Removed volume

We have calculated the removed volume after the first plasma breakdown. Figure.9; Figure 10 and Figure 11 represent the removed volume for the different micro-tools diameter and applied voltages of $V_{EE} = 25V$; $V_{EE} = 50V$; $V_{EE} = 75V$ respectively. We find that the removed volume is around $10^4 \mu m^3$ in the case of small micro-tools diameter ($\Phi=125 \mu m$; $\Phi=40 \mu m$; $\Phi=20 \mu m$)

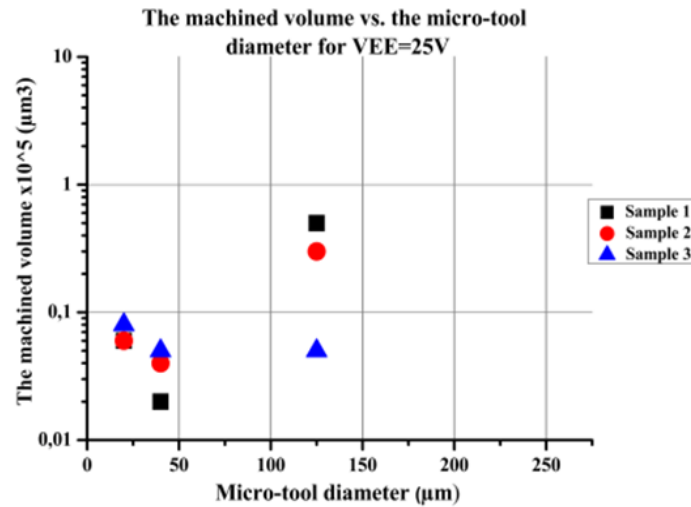


Figure 9. The removed volume for $V_{EE} = 25V$ & $C=10nF$.

whatever the value of the applied voltage ($V_{EE} = 25V$; $V_{EE} = 50V$; $V_{EE} = 75V$). However, the removed volume becomes significant in the case of a micro-tool diameter of $\Phi=250 \mu m$. It is around $10^6 \mu m^3$ for $V_{EE} = 50V$ and $V_{EE} = 75V$. For a voltage of $V_{EE} = 25V$ and a micro-tool diameter of $\Phi=250 \mu m$, we obtained just surface traces. Therefore, it is impossible to determine the removed volume in this case.

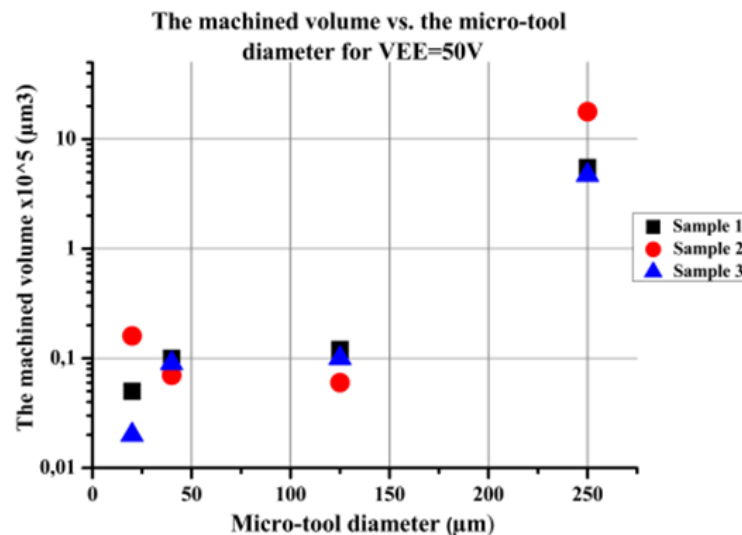


Figure 10. The removed volume for $V_{EE} = 50V$ & $C=10nF$.

From these results we can conclude that: (1) high micro-tool diameters are used to machine workpieces during the roughing phase where the removed volume is bigger than in case of an applied voltage of $V_{EE} = 25V$. (2) Small micro-tools diameter leads to remove a small material volume regardless of the applied voltage, which is advantageous during the finishing phase.

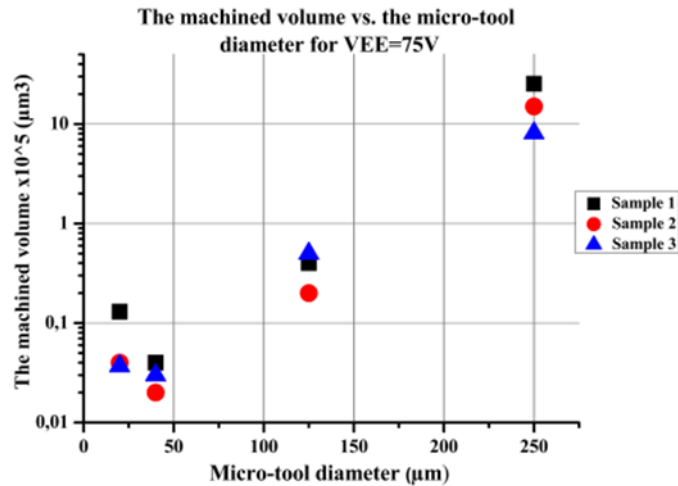


Figure 11. The removed volume for $V_{EE} = 75V$ & $C=10nF$.

3.4. Craters obtained after the first breakdown

To know the effect of the micro-tool diameter and the applied voltage on the crater shape and the surface condition, we have performed several experiments. Figure 12 represents the craters obtained for micro-tools diameter of $\Phi=250 \mu\text{m}$ and $\Phi=20 \mu\text{m}$ at different applied voltages ($V_{EE} = 25V$; $V_{EE} = 50V$; $V_{EE} = 75V$).

From these results, we can see that for an applied voltage of $V_{EE} = 25V$ and a micro-tool diameter of $\Phi=250 \mu\text{m}$, the removed volume is low because the discharges energy is also low in this case. However, an applied voltage of $V_{EE} = 50V$ and $V_{EE} = 75V$ leads to the formation of a crater where the removed material is important, and the maximal depth of the crater is equal to $27 \mu\text{m}$, $43 \mu\text{m}$ respectively.

Concerning the micro-tool diameter of $\Phi=20 \mu\text{m}$, we notice that the craters obtained have the same shape and almost the same maximum depth ($10 \mu\text{m}$) whatever the value of the applied voltage.

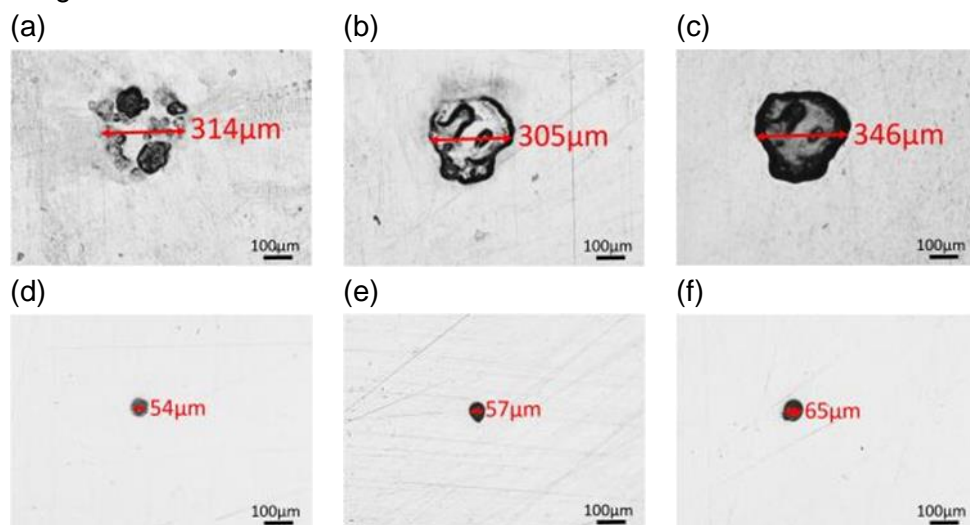


Figure 12. Shape of the craters obtained in the case of: (a) $\Phi=250\mu\text{m}$; $V_{EE} = 25V$, (b) $\Phi=250\mu\text{m}$; $V_{EE} = 50V$, (c) $\Phi=250\mu\text{m}$; $V_{EE} = 75V$, (d) $\Phi=20\mu\text{m}$; $V_{EE} = 25V$, (e) $\Phi=20\mu\text{m}$; $V_{EE} = 50V$, $\Phi=20\mu\text{m}$; $V_{EE} = 75V$.

Figure 13 represents an example of a hole obtained during drilling with a micro-tool diameter of $\Phi=250\mu\text{m}$ and an applied voltage of $V_{EE} = 50\text{V}$.

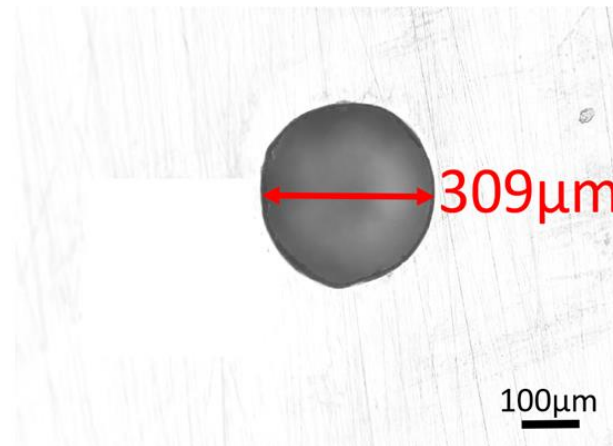


Figure13. Hole shape obtained for: $\Phi=250\mu\text{m}$ et $V_{EE} = 50\text{V}$.

4. CONCLUSION

It is important to know the influence of physical, electrical, and geometrical parameters on the machining resolution (surface condition and shape crater). We have done a quantitative and qualitative study of certain parameters. It was shown that the electric field is constant for the different micro-tools diameter, and it is around $6\text{V}/\mu\text{m}$. Concerning the average discharges energy, we conclude that it did not depend on the micro-tool diameter. The removed volume is in the same order for small diameters whatever the value of the applied voltage, it is around $10^4 \mu\text{m}^3$. However, it is equal to $10^6 \mu\text{m}^3$ for a micro-tool diameter of $\Phi=250 \mu\text{m}$. This study has demonstrated that micro-tools with high diameter could be used during the roughing phase in order to ensure fast machining and remove high material volume from the workpiece. Concerning the micro-tools with small diameters, they should be used in the finishing phase with low voltages in order to obtain craters with the least rough surface. An applied voltage of $V_{EE} = 50\text{V}$ gives satisfactory results: circular craters with less dark surface (because the micro-tool is less charred) than in the case of an applied voltage of $V_{EE} = 75\text{V}$. The voltage of $V_{EE} = 50\text{V}$ has been used in a hole machining (Figure13) and it will be part of another study [7] where the choice of the drilling parameters takes into consideration the removed volume, the hole shape, and the hole surface condition.

REFERENCES

- [1] G. Girardin, "Development of a μEDM process", PhD thesis, UCBL, 2013.
- [2] Uhlmann E., Piltz S and Doll U., "Machining of micro/miniature dies and moulds by electrical discharge machining", *J. Mat. Proc. Tech.*, **167**, 488–493 (2005).
- [3] I. Ait-Ali, P. Morin, V. Semet, M. Cabrera, and R. Ferrigno, "High precision machining strategy for the integration of electrochemical cells in Cyclic Olefin Copolymer microfluidic devices", *Procedia Engineering*, **47**, 450–453 (2012).
- [4] Lin, J., et al. 3-Dimensional graphene carbon nanotube carpet-based microsupercapacitors with high electrochemical performance. *Nano Lett.* **13**, 72–78 (2013).
- [5] R. Dahmani. "Optimization of a μEDM process", UCBL, Lyon (2015).
- [6] Goodfellow, Tungsten. [<https://www.goodfellow.com>].
- [7] A. Tafraouti, et al. Micro Electrical Discharge Machining (μEDM): holes drilling and characterization of the process parameters, *Nanomaterials Science & Engineering (in press)*.

Conjugated poly(platina-yne)s for new materials applications

Rayya A. Al Balushi ^{1*}, Ashanul Haque ², Muhammad S. Khan ^{3*}

¹ Department of Basic Science, College of Applied and Health Sciences, A' Sharqiyah University, Ibra 400, Oman

² Department of Chemistry, College of Science, University of Ha'il, Ha'il 81451, KSA

³ Department of Chemistry, Sultan Qaboos University, P.O. Box 36, Al Khod 123, Oman

* Corresponding authors, E-mail: rayya.albalushi@asu.edu.om, msk@squ.edu.om

Abstract

Conjugated poly(metalla-yne)s constitute an important class of fascinating materials in view of their potential applications in opto-electronic (O-E) devices such as photo-cells, field-effect transistors (FETs), photo switches, light emitting diodes (LEDs), liquid crystal displays (LCDs) and non-linear optics (NLOs). In poly(metalla-yne)s the photo-physical properties of transition metal fragments are coupled to those of the organic poly-yne)s. For example, the incorporation of heavy metal fragment such as bis(trialkylphosphine)Pt(II) along the polymer backbone introduces large spin-orbit coupling to allow light emission from the triplet excited state. In this context, Pt(II) poly-yne)s incorporating a wide variety of spacer groups have been widely investigated in our laboratory. Pt(II) poly-yne)s are excellent triplet emitters. The triplet states in Pt(II) poly-yne)s can be investigated by direct optical excitation. Consequently, the Pt(II) poly-yne)s can serve as model compounds to study the basic photo-physical properties of conjugated hydrocarbons poly-yne)s. The conjugated spacer is important in tuning the O-E properties of the Pt(II) poly-yne)s. Herein, we present the experimental and theoretical studies of some Pt(II) poly-yne)s and explore their potential for application in O-E devices.

Key Words: Conjugated poly(metalla-yne)s, Di-yne)s, Poly-yne)s, Opto-electronic devices

1. INTRODUCTION

Past two decades have witnessed a large volume of research on π -conjugated organic materials incorporating a variety of spacers and transition metal ions. It is due to their possible potential applications in the fabrication of opto-electronic (O-E) devices such as photo-voltaic cells, field-effect transistors (FETs), photo-switches, light emitting diodes (LEDs), liquid crystal displays (LCDs) and non-linear optics (NLO).[1,2] In this context, poly(metalla-yne)s, particularly Pt(II) poly-yne)s and diynes incorporating conjugated carbocyclic and heterocyclic spacers have been extensively investigated.[3] Basically, purely organic materials have low conductivity and less populated excited states, which limit their application in O-E devices. Fortunately, this issue could be tackled by incorporating a metal ion into the organic backbone, which dramatically improves the photo-physics of the resulting materials. The incorporation of Pt(II) in the polymer backbone introduces large spin-orbit coupling to allow light emission from the triplet (T₁) excited state, which is extremely efficient (~ 100% efficiency) at low temperature [4,5]. The long lived T₁ promote charge generation and thus enhances the efficiency of O-E devices.[6-8] Among different spacers, stilbene and azobenzene spacers are intriguing moieties due to planar conjugated structures, stability, suitable energy levels, low band-gap

and ability to form uniform films. Furthermore, they are well-known photo-responsive chromophores that undergoes photo- and thermal induced geometric isomerization.[9] A photo-switch molecule is a molecule that can switch between two different thermodynamically stable forms when external light is applied to it. Azobenzene and stilbene could be considered as photo-switch molecules because they are chromophores that can undergo reversible geometrical photoisomerization. Considering the potential of these two spacers and the intriguing features of Pt(II), we have [10, 11] investigated Pt(II) di-ynes and poly-ynes incorporating meta and para-azobenzene and para-stilbene spacers (Figure 1).

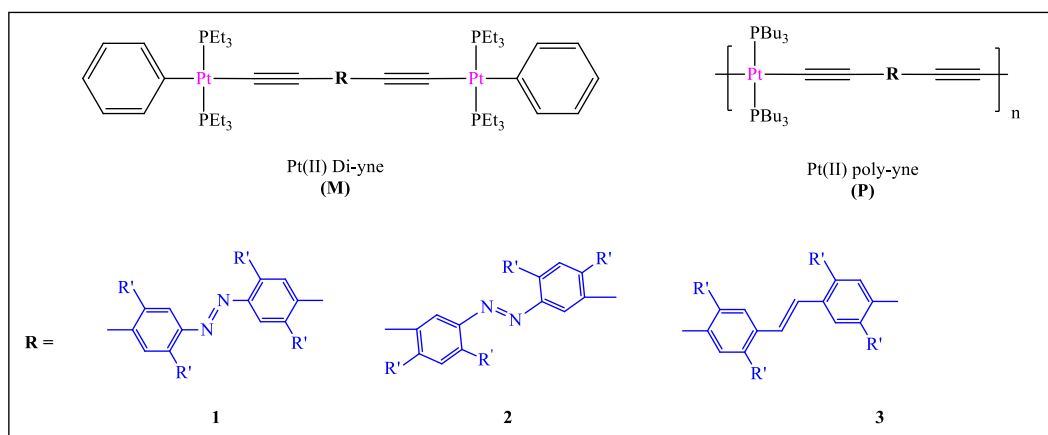


Figure 1. Pt(II) di-ynes and poly-ynes incorporating meta- and para-azobenzene and stilbene spacers.

2. STRUCTURE- PROPERTY RELATIONSHIPS

The X-ray crystal structures of para- azobenzene and stilbene spacers are shown in **Figure 2**. The crystal structure confirmed the *trans* arrangement of the central para- azobenzene and stilbene groups in Pt(II) di-ynes.

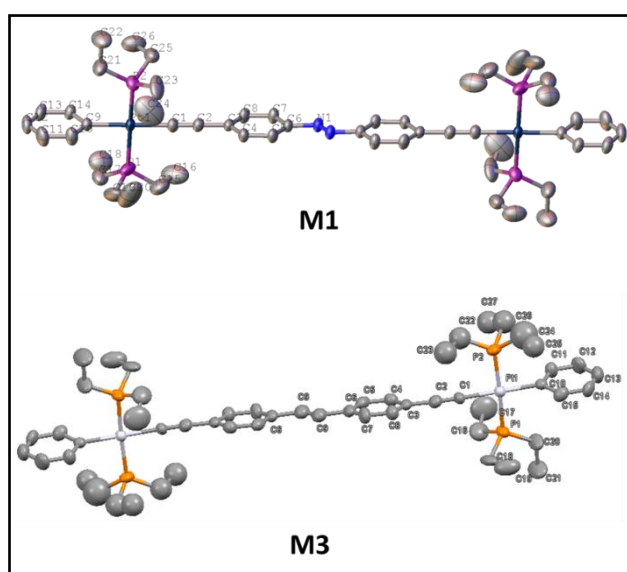


Figure 2. The crystal structure of Pt(II) di-ynes incorporating para- azobenzene (**M1**) and stilbene (**M3**) spacers.

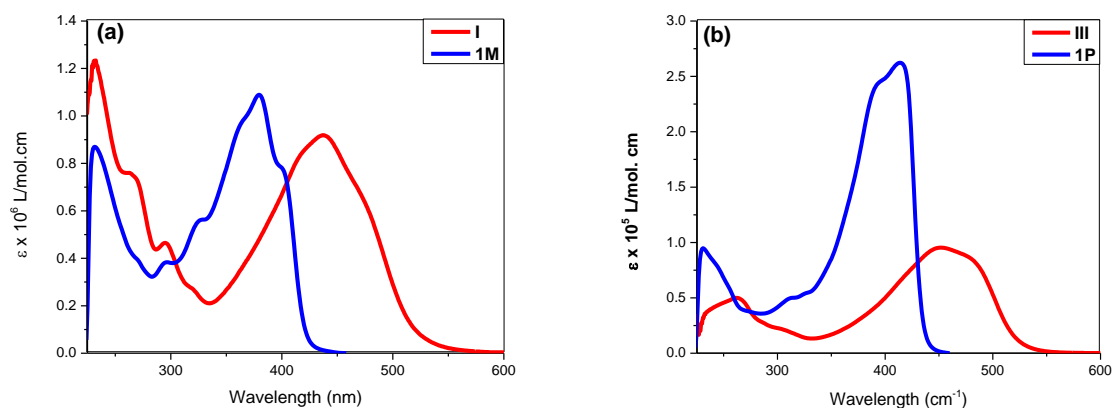


Figure 3. Optical absorption spectra of Pt(II) di-ynes incorporating (a) para-azobenzene (I) and para-stilbene (1M) spacer groups. (b) Pt(II) poly-ynes incorporating para-azobenzene (III) and stilbene (1P) groups.

Regarding the structure-property relationships in *para*-azobenzene and stilbene containing Pt(II) di-ynes and poly-ynes, we have carried out an extensive photo-physical experiments and DFT calculations. We found that delocalization within the molecular and polymeric units are significantly different in the two *para*-systems. This fact was evidenced by both the UV-vis. absorption spectroscopy and DFT calculations.

In the case of azobenzene, the presence of N-atoms caused more bathochromic shift than stilbene counterparts (Figure 3). This was attributed to the metal to ligand charge transfer (MLCT) electron excitations within the di- and the polymetallic complexes incorporating *para*-azobenzene spacers [10, 11].

3. PHOTO-ISOMERIZATION STUDY

Azobenzene and stilbene containing materials are well known for their ability to show morphological changes, which are attributed to trans-cis isomerization. This isomerization led to geometric change around the central moiety, which could be utilized in several applications. The isomerization process incorporating these groups depends on many factors such as structure, solvent, electron delocalization/conjugation. In this work, photo-induced morphological changes in Platinum(II) complexes containing *para*-stilbene and *para*-azobenzene spacer groups were investigated at different wavelengths in dichloromethane and toluene as solvent. Comparing absorption spectra taken in DCM, the absorption bands were red shifted in the case of toluene. It was interesting to note that there is no major change was observed by changing the solvent. On the other hand, at 254 nm which is a low wavelength a shift of the bands was observed which is an indication of cis-trans isomerization. The inclusion of Pt(II) centers into the organic ligands was found to affect the isomerization process more in stilbene system compared to azobenzene. However, in azobenzene systems, the cis-trans isomerization was more pronounced in the ligands compared to the Pt(II) di-ynes and poly-ynes. [10,11]

4. CONCLUSION

A series of Pt(II) di- and poly-ynes containing para-stilbene and azobenzene spacer groups have been investigated and their structure-property relationships have been compared. The materials of both studied systems underwent photo-induced reversible cis-trans isomerization in solution. The isomerization process in para-stilbene system has been found to be affected by the inclusion of the platinum(II) metal. Compared to para-azobenzene compounds, para-stilbene has indicated a higher ability to show photo-isomerization. For O-E applications, the judicious selection of spacers is necessary. The isomers of the spacers selected greatly influence the flow of electron in the molecule.

ACKNOWLEDGMENTS

RAA gratefully acknowledges the Ministry of Higher Education, Research and Innovation, Oman (Project No. BFP/RGP/EI/18/076) for funding and A' Sharqiyah University, Oman, for a research grant (ASU-FSFR/CAHS/DBS -01/2019). MSK acknowledges the Ministry of Higher Education, Research and Innovation (MOHERI), Oman (Grant: RC/ RG-SCI/CHEM/20/01) for funding.

REFERENCES

- [1] A. Haque, R. A. Al-Balushi, I. J. Al-Busaidi, M. S. Khan, and P. R. Raithby, [*Chem. Rev.*, **118**\(18\), 8474 \(2018\)](#).
- [2] J. S. Wilson, A. S. Dhoot, A. J. A. B.Seelay., M. S. Khan, A. Kohler, R. H. Friend, [*Nature*, **413**, 828 \(2001\)](#).
- [3] M. Mauro, A. Aliprandi, D., Septiadi, N. S. Kehr and L. De, [*Chem Soc Rev*, **43**, 4144 \(2014\)](#).
- [4] N. Chawdhury, A. Köhler, R. H. Friend, W-Y. Wong, J. Lewis, M. Younus, P. R.
- [5] Raithby, T. C. Corcoran, M. R. Al-Mandhary, and M. S. Khan, [*J. Chem. Phys.* **110**, 4963 \(1999\)](#).
- [6] J. S. Wilson, N. Chawdhury, M. R. A. Al-Mandhary, M. Younus, M. S. Khan, P. R. R. Raithby; A. Köhler, R. H. Friend, [*J. Am. Chem. Soc.*, **123**, 9412 \(2001\)](#).
- [7] L. S. Devi, M. K. Al-Suti, N. Zhang, S. J. Teat, L. Male, H. A. Sparkes, M. S. Khan, P. R. Raithby; A. Kohler, [*Macromol.*, **42**, 1131 \(2009\)](#).
- [8] A. Köhler, A. L. T. Khan, J. S. Wilson, C. Dosche, M. K. Al-Suti, H. H. Shah, M. S. Khan, [*J. Chem. Phys.*, **136**, 094905 \(2012\)](#).
- [9] U. H. Bunz, V. Enkelmann, L. Kloppenburg, D. Jones, K. D. Shimizu, J. B. Claridge, H.-C. zur Loye and G. Lieser, [*Chem. mat.*, **11**, 1416 \(1999\)](#).
- [10] T. A. Singleton, K. S. Ramsay, M. M. Barsan, I. S. Butler and, C. J., Barrett, [*J. Phys. Chem. B*, **116**\(32\), 9860 \(2012\)](#).
- [11] R. A. Al-Balushi, A. Haque, M. Jayapal, M. K. Al-Suti, J. Husband, M. S. Khan, O. F. Koentjoro, J. M. Skelton, K. C. Molloy and P. R. Raithby, [*Inorg. Chem.*, **55** \(21\), 10955 \(2016\)](#).
- [12] I. J. Al-Busaidi, A. Haque, J. Husband, N. K. Al-Rasbi, O. K. Abou-Zied, R. A. Al Balushi, M. S. Khan and P. R. Raithby, [*Dalton Trans.*, **50**, 2555 \(2021\)](#).

Effect of long baffles on forced convection heat transfer over multiple heated blocks

AMIRAT Hamza * and KORICHI Abdelkader

Laboratory of Mechanics, Physics and Mathematical Modeling (LMP2M),
University of Yahia Fares, Medea, Algeria

*Corresponding author, e-mail address: amirat.hamza@gmail.com

Abstract

The forced convection heat transfer over five heated blocks in a horizontal channel contains long baffles fixed at the upper wall, is investigated. The finite volume with Ansys Fluent © code is used as a numerical analysis tool. Simulations are performed for two cases with and without baffles. The study is limited to a steady-state and the calculations are run in an unsteady scheme to avoid unrealistic results and ensure that the flow still steady under the simulation conditions. The dimensions of the blocks are considered the same ($w=h=0.5$), the cooling process is done with air ($Pr=0.71$). The streamlines, isotherms, and the local Nusselt are illustrated to show the effect of the long baffles on the fluid flow, temperature, and heat transfer in both fluid and solid phases. The results show that the long baffles cause a significant heat transfer enhancement over the blocks due to changes in the flow behaviors.

Key Words: Electronic cooling, Finite volume method, Heated blocks, Heat transfer enhancement, Baffles.

Nomenclature

Symbols :	Re Reynolds number
A Exposed obstacle area, m^2	T Temperature, K
c_p Specific heat, $J \cdot kg^{-1} \cdot K^{-1}$	t Dimensionless time
d Dimensionless baffles thickness	u Dimensionless x-component of velocity
h Dimensionless heated block height	v Dimensionless y-component of velocity
h_c Convective heat transfer coefficient, $W \cdot m^{-2} \cdot K^{-1}$	w Dimensionless block width
H Dimensionless channel height	x, y Dimensionless cartesian coordinates
k Thermal conductivity, $W \cdot m^{-1} \cdot K^{-1}$	Greek symbols :
L Dimensionless distance between the baffles vertical centerline and the block front or rear face	μ Dynamic viscosity, $kg \cdot s^{-1} \cdot m^{-1}$
L_{in} Dimensionless distance between the inlet and the first block front face	θ Dimensionless temperature
L_{out} Dimensionless distance between the outlet and the last block front face	ρ Density, $kg \cdot m^{-3}$
n Normal coordinate	Subscripts :
Nu Nusselt number	f Fluid

\overline{Nu} Mean Nusselt number	s Obstacle peripheral distance, m^2
p Dimensionless pressure	$s/$ Solid
Pe Peclet number	m Mean
Pr Prandtl number	Superscripts :
q Dimensionless heat flux	* Dimensional

1. INTRODUCTION

Heat transfer enhancement in cooling presents a high challenge in today's and future technology. To meet the needs of the modern world, industrial systems are required to be more powerful, speedier, and with a longer lifetime under work which implies more heat generations. The temperature over limits makes damage any engineering system and for this reason, thermal researchers intervene with a lot of research papers to make the cooling process better. Bergles et al [1] introduced 13 techniques to increase the heat transfer rate. Yeh [2] briefly summarized the cooling techniques that are related to electronic equipment. Those techniques are categorized into two different types: "passive" and "active" methods. Passive techniques use no external power source, unlike active techniques which require an external power source. The convection heat transfer in a channel that contains multiple heated blocks is studied experimentally by [3] and numerically in [4-7]. Their results show that the weakest heat transfer portion over the blocks is located in the rear faces where is negative values of the local Nusselt number are captured. The poor heat transfer in these regions is due to the warm air vortex stuck in this area. To avoid this problem, Herman and Kang [8] used curved vanes to lead the flow into the inter blocks cavity and force the stuck flow to move. Their findings show a clear improvement in heat transfer but with important pressure losses, about twice to thrice the amount of the case without curved vanes. With the same curved vans shape Lorenzini-Gutierrez et al. [9] found that heat transfer is improved on the backsides of the blocks. In another technique, Cheng *et al.*, Sultan and Ali [10-12] used opening after the blocks to let the flow move throw the holes into or out of the channel naturally. Their results demonstrate that openings make the heat transfer better over the blocks especially on the rear faces. This study is an attempt to enhance the heat transfer over heated blocks countered in the power electronics cooling industry. The intent is to investigate the effect of using long baffles fixed at the upper wall of the channel, on the fluid flow and heat transfer.

2. PHYSICAL MODEL AND MATHEMATICAL FORMULATION

2.1. Setup description

The configurations involved in this investigation are shown in Figure 1. It consists of a 2D channel contained five heated blocks with identical sizes ($w=h=0.25$). Long baffles with constant length $l=0.875$ and thickness $d=0.025$ are fixed in the upper wall of the channel, for the first configuration (figure 1a). The second configuration is investigated without long baffles for a comparative reason (figure 1b). The horizontal distance between the baffle vertical centerline and the rear face of the next block is fixed at $L=0.125$. In both cases, a uniform heat

flux “ q ” is imposed at the bottom of each obstacle and a flow with a parabolic profile velocity is applied at the inlet.

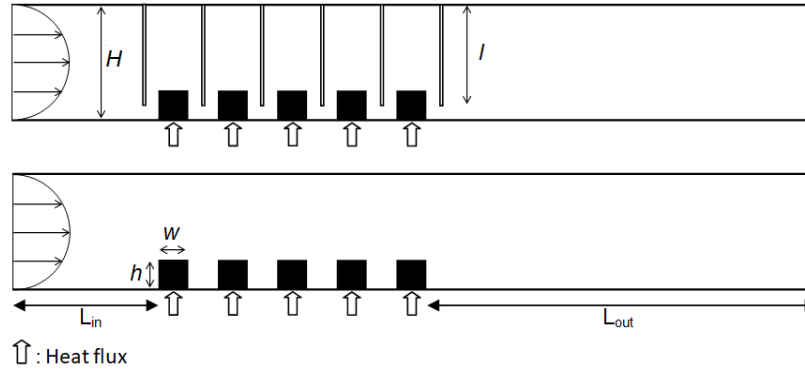


Figure 1. Schematic diagram of the simulated physical domain channel: (a) with long baffles, (b) without long baffles.

The flow is assumed to be laminar and incompressible; the fluid is Newtonian with constant thermo-physical properties. The buoyancy and viscous dissipation are neglected. Thus, the mathematical equations of the physical model in the non-dimensional form can be written as follows:

Mass:

$$\frac{\partial u}{\partial x} + \frac{\partial v}{\partial y} \quad (1)$$

x-momentum:

$$\text{Re} \frac{\partial u}{\partial t} + \text{Re}(u \frac{\partial u}{\partial x} + v \frac{\partial u}{\partial y}) = -\frac{\partial p}{\partial x} + (\frac{\partial^2 u}{\partial x^2} + \frac{\partial^2 u}{\partial y^2}) \quad (2)$$

y-momentum:

$$\text{Re} \frac{\partial v}{\partial t} + \text{Re}(u \frac{\partial v}{\partial x} + v \frac{\partial v}{\partial y}) = -\frac{\partial p}{\partial y} + (\frac{\partial^2 v}{\partial x^2} + \frac{\partial^2 v}{\partial y^2}) \quad (3)$$

Energy:

The fluid phase:

$$\text{Pe} \frac{\partial \theta_f}{\partial t} + \text{Pe}(u \frac{\partial \theta_f}{\partial x} + v \frac{\partial \theta_f}{\partial y}) = (\frac{\partial^2 \theta_f}{\partial x^2} + \frac{\partial^2 \theta_f}{\partial y^2}) \quad (4)$$

The solid phase:

$$\frac{\rho_{sl} \cdot c_{psl}}{\rho_f \cdot c_{pf}} \text{Pe} (\frac{\partial \theta_{sl}}{\partial t}) = \frac{k_{sl}}{k_f} (\frac{\partial^2 \theta_{sl}}{\partial x^2} + \frac{\partial^2 \theta_{sl}}{\partial y^2}) \quad (5)$$

Non-dimensional variables:

$$x = \frac{x^*}{H^*}; y = \frac{y^*}{H^*}; u = \frac{u^*}{u_m^*}; v = \frac{v^*}{u_m^*}; \theta = \frac{(T - T_0)}{(q'' \cdot H^* / k_f)}; \quad (6)$$

$$p = \frac{p^* \cdot H^*}{\mu_f \cdot u_m^*}; v_j = \frac{v_j^*}{u_m^*}$$

And the relevant non-dimensional numbers are:

$$\text{Re} = \frac{\rho_f \cdot u_m^* \cdot H^*}{\mu_f}; \text{Pr} = \frac{\mu_f \cdot c_{pf}}{k_f}; \text{Pe} = \text{Re} \cdot \text{Pr} \quad (7)$$

2.2. Boundary conditions

The boundary conditions are summarized in table 1:

Table 1. Boundary conditions.

Border of the geometry	Hydrodynamic conditions	Thermal conditions
Inlet	$\frac{\partial p}{\partial x} = 0; u = 6y(1-y);$ $v = 0$	$\theta_f = 0$
Outlet	$\frac{\partial u}{\partial x} = \frac{\partial v}{\partial x} = 0;$ The pressure is equal to the ambient pressure.	$\frac{\partial \theta_f}{\partial x} = 0$
Channel walls	$u = v = 0$	$\frac{\partial \theta_f}{\partial x} = 0$
Block bases	$u = v = 0$	$q = 1$
Solid-Fluid interface	$u = v = 0$	$\theta_f = \theta_{sl};$ $k_f \frac{\partial \theta_f}{\partial n} = k_{sl} \frac{\partial \theta_{sl}}{\partial n}$

The inlet and outlet distances are chosen to be $L_{in}=3$ and $L_{out}=20$, respectively. The choice is made after a lot of calculation cases for different inlet and outlet distances.

2.3. Numerical solution and validation

The governing equations of the physical model presented above are solved numerically using the finite volume method. The simulation is performed using the software Ansys Fluent® and the Simple algorithm developed by Patankar [13] is employed. The implicit second-order scheme is used for time discretization while the second-order upwind and central second-order differencing schemes are chosen for the convective and diffusive terms respectively. The grid independence is checked for four grid sizes 590×45, 935×75, 1350×110, and 1950×145 at $\text{Re}=1000$. The choice of the grid distribution of 1350×110 is judged to be sufficient for the Reynolds number investigated here, where the difference between local Nusselt values was obtained using the two mesh sizes 1350×110 and 1950×145 does not exceed 2% (figure 2a). The validity of the calculations is investigated by comparison with the work of Young and Vafai [4]. As it appears in figure 2b, a great agreement is obtained and the maximum deviation is less than 3%. The dimensionless time step is chosen between 10^{-5} and 10^{-3} to ensure unsteady

calculations convergence. All calculations are run iteratively in the unsteady state until reaching the steady-state unless reducing Reynolds number to still in steady-state flow. The residuals for all independent variables are fixed at 10^{-6} .

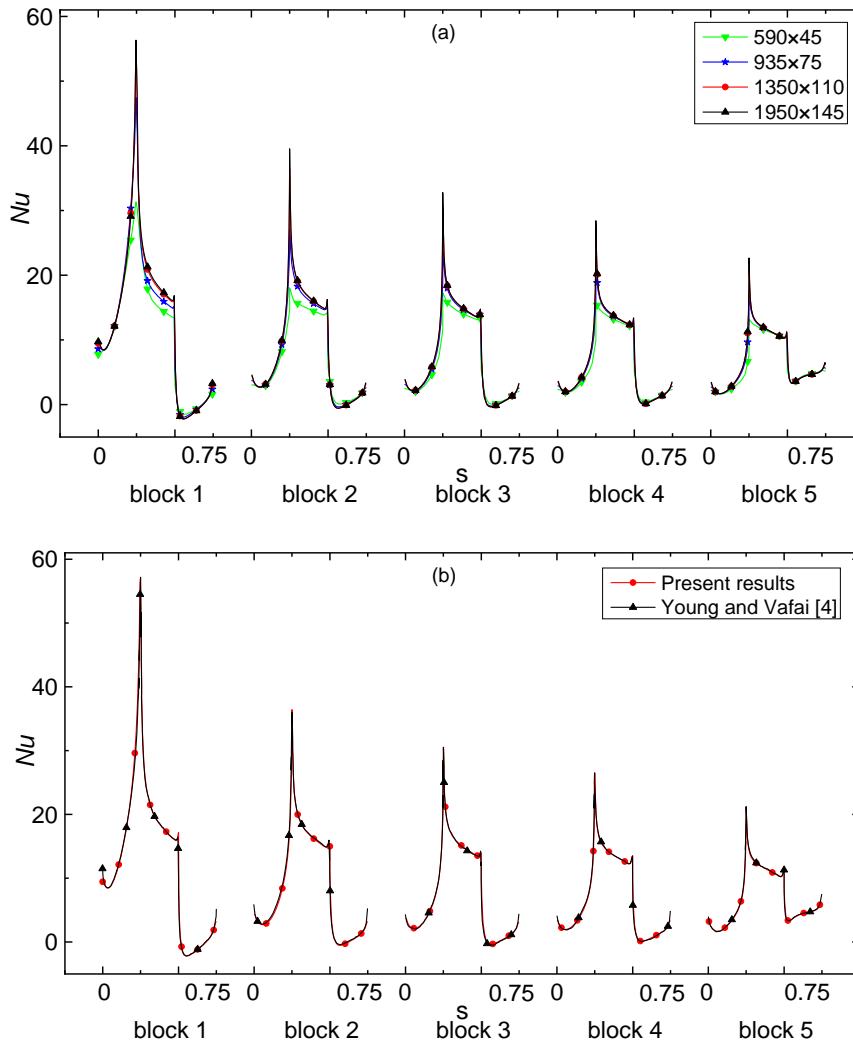


Figure 2. Validation and grid independence: (a) Grid independence (b) Comparison of present results with those of Young and Vafai [4].

3. RESULTS AND DISCUSSION

The results are summarized as streamlines temperature contours and local Nusselt number (eq. 8).

$$Nu_x = \frac{h_c \cdot H^*}{k_f} = -\frac{1}{\theta_s} \cdot \frac{\partial \theta_f}{\partial n} \quad (8)$$

h_c is heat transfer coefficient and “ n ” denotes the normal coordinate.

3.1. Streamlines

As it appears in figure 3a, the streamline goes forward in a smooth motion till they hit the first block and baffle. The gaps between the baffles are filled with three recirculation zones: a big clockwise zone, conducted by the main channel flow, this vortex approximately takes all the space between the baffles. The shear in the vicinity of the front and rear faces of each baffle leads to the creation of two other co-rotating vortexes on both sides of the baffles. The long length of the baffle makes the flow penetrate the gaps between the blocks, which breaks the stagnation of the warm air stuck in these regions as detected for the case without baffles, figure 3b. A moderate size vortex is shown above each block's horizontal face. Due to the sudden change in the flow passage section caused by the combined effect of the baffle and block, superposed two large vortexes are formed in the back stream of the last baffle. These two vortexes appear like a plug, reducing the main flow to a thin layer near the bottom wall. Unlike the case with long baffles, a moderate size vortex is detected after the last block in the channel without long baffles.

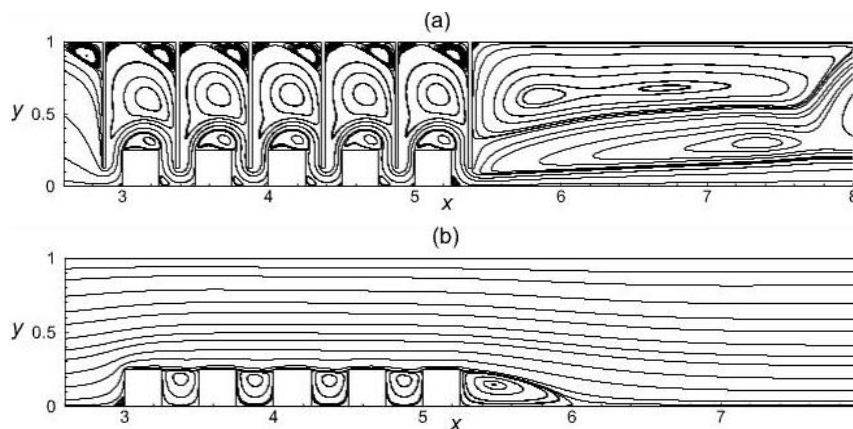


Figure 3. Streamlines for $Re=100$ with: (a) with long baffles and (b) without long baffles.

3.2. Isotherms contours

The isotherms contours are presented for both cases with and without baffles in figure 4. As shown the presence of baffles generates a higher temperature gradient in the solid phase. All blocks are cooled regularly and the temperature gradients in the solid appear very close to those in the fluid phase (figure 4a). For the case, without baffles, the temperatures increase through the blocks with the flow direction until achieving quite high values for the last block (figure 4b). The lowest temperature is captured on the upper corner of the front face followed by the upper corner of the rear face, while the maximum temperature is recorded on the back lower corner. In terms of the thermal field, it is clearly shown that the long baffles bring

significant changes to the isothermal shape in the solid and fluid phases. As it appears the temperature of the blocks is reduced with the long baffles.

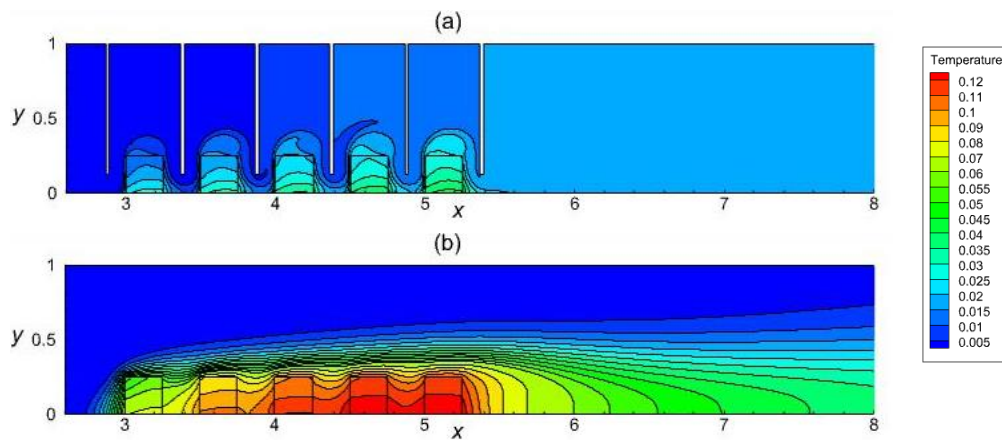


Figure 4. Isotherms for $Re=100$ with: (a) with long baffles and (b) without long baffles.

3.3. Local Nusselt number

To show the effect of the baffles on the heat transfer, the mean Nusselt number for the cases with ($Re=100$) and without long baffles ($Re=100$ and 1000) are presented in Figure 5. As it can be seen, the heat transfer is increased with the baffles ($Re=100$) more than 3 times better than the case without long baffles at $Re=100$. Moreover, the local Nusselt number values for the case with baffles at $Re=100$ are about two times much higher than the case without baffles at $Re=1000$. The improvement is due to the increase of the flow velocity over the blocks and the elimination of the warm recirculation vortex after each block.

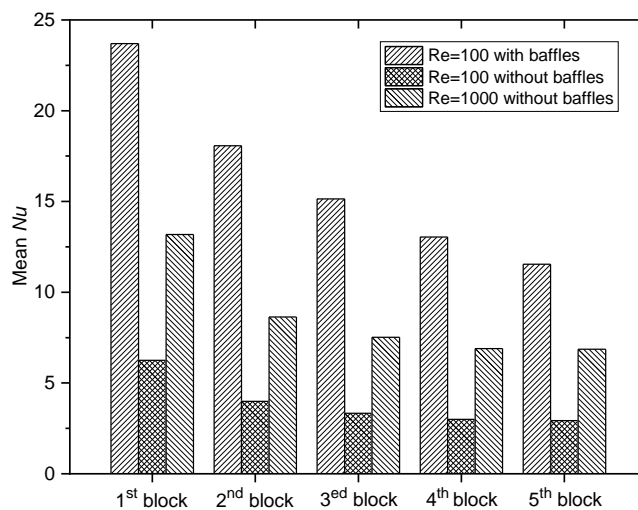


Figure 5. Mean Nusselt number with and without long baffles for $Re=100$ and $Re=1000$.

4. CONCLUSIONS

In this study, the forced convection heat transfer over five heated blocks with and without long baffles is studied numerically. The calculations are performed for $Re=100$, 1000 at constant baffles length ($l=0.875$) and width ($d=0.025$). The results show that the heat transfer is improved. The main observations are briefly summarized as follows: The presence of the long baffles makes the inter blocks cavities no more occupied by the warm vortexes and the flow structure is changed. Concerning temperature contours, the temperature in the solid and fluid phases is decreased significantly compared to the case without long baffles. For the heat transfer quantification, the enhancement exceeds 3.5 and about 2 times better compared to the cases without baffles for $Re=100$ and $Re=1000$, respectively.

REFERENCES

- [1] A.E. Bergles, V. Nirmalan, G.H. Junkhan, and R.L. Webb, *Bibliography on augmentation of convective heat and mass transfer II*, Heat Transfer Laboratory Report HTL-31, ISU-ERI-Ames- 84221, Iowa State University, Ames (1983).
- [2] L. Yeh, [*Journal of Electronic Packaging, Transactions of the ASME*, **117**, 333-339 \(1995\)](#).
- [3] J. S. Nigen and C. H. Amon, [*Journal of Fluids Engineering*, **116**, 499-507 \(1994\)](#).
- [4] T. J. Young and K. Vafai, [*International Journal of Heat and Mass Transfer*, **41**, 3279-3298 \(1998\)](#).
- [5] E. Arquis, M. A. Rady and S. A. Nada, [*International Journal of Heat and Fluid Flow*, **28**, 787-805 \(2007\)](#).
- [6] M. H. Yang, R. H. Yeh and J. J. Hwang, [*Energy Conversion and Management*, **51**, 1277-1286 \(2010\)](#).
- [7] G. Imani, M. Maerefat and K. Hooman, [*Numerical Heat Transfer, Part A: Applications*, **62**, \(2012\)](#).
- [8] C. Herman and E. Kang, [*International Journal of Heat and Mass Transfer*, **45**, 3741-3757 \(2002\)](#).
- [9] D. Lorenzini-Gutierrez, A. Hernandez-Guerrero, J. L. Luviano-Ortiz and J. C. Leon-Conejo, [*Applied Thermal Engineering*, **75**, 800-808 \(2015\)](#).
- [10] Y. P. Cheng, T. S. Lee, and H. T. Low, [*Applied Thermal Engineering*, **28**, 1826-1833 \(2008\)](#).
- [11] G. I. Sultan, [*Microelectronics Journal*, **31**, 773-779 \(2000\)](#).
- [12] R. k. Ali, [*Applied Thermal Engineering*, **29**, 2766-2772 \(2009\)](#).
- [13] S. V. Patankar, *Numerical Heat Transfer and Fluid Flow*, 1st Edition, CRC, New York (1980).

Use of infrared temperature sensor to estimate the evolution of transformation temperature of SMA actuator wires

Maria Clara S. de Castro * and Tadeu Castro da Silva *

Department of Mechanical Engineering, Universidade Federal Fluminense, Rua Passo da Patria, 156, Niteroi Rio de Janeiro, 24210-240, Brazil

*Corresponding authors, e-mail address: castromaria@id.uff.br; tadeucastro@id.uff.br

Abstract

Shape memory alloys (SMAs) can be used as actuators with application of temperature gradients, altering material's crystallographic phase while it reaches transformation temperatures, and it extends macroscopically. Measuring temperature is essential when applying SMAs.

It's possible to measure temperature of SMA with any standard temperature measuring instrument, except when used on small size scales, such as actuator wires. In this work, we attempted to focus an infrared sensor on a thin SMA wire with 150 micrometers diameter and measure its temperature during thermal cycling procedures, characterizing some material properties such as the evolution of transformation temperatures and hysteresis loops.

Key Words: Actuator wires, Infrared sensor, NiTi, Shape memory alloys, Temperature

1. INTRODUCTION

Shape memory alloys can undergo processes of temperature-induced phase transformations and can be used as actuators. Temperature gradients through the forward and reverse martensitic transformations results in fully recoverable deformations of values up to 5.5% of their initial length, explaining the success of these alloys as actuators. There are four important transformation temperatures in the process of heating and cooling SMA, they are: martensite start (M_s) and finish (M_f) temperatures that occur during cooling and austenite start (A_s) and finish (A_f) temperatures that occur during heating. It is known that thermal cycling influences thermal properties of SMAs, reducing characteristic transformation temperatures [1].

It is not possible to use thermocouples or other standard temperature measurement instruments on thin wires, it is common to use a relation between electric current applied to a wire and its temperature to be able to estimate the phase transformation temperatures [2].

In this work, some NiTi wire specimens with 150 μm diameter are subjected to thermal cycling and investigated for changes in their thermodynamic properties such as the evolution of transformation temperatures, hysteresis loops and the linear relationship between the austenitic (A_s and A_f) and martensitic (M_s and M_f) transformation temperatures and applied stress of 150 MPa. In order to find more reliable methods of measuring temperature, an infrared (IR) sensor is focused in the specimens while they are cycled through the forward and reverse martensitic transformations, between 25 to about 120°C. It's needed to aim the

specimen with the aid of converging lenses to use IR sensors in that kind of application, trying to focus the sensor on such small specimen is the biggest challenge of the work.

2. MATERIALS AND PROCEDURES

A 0.150 mm in diameter commercial NiTi (54 at.% Ni) actuator wire was used in the present study. The wire is marketed by SAES Getters under the brand name *SmartFlex*[®] 150.

The actuator wire temperature was determined with the use of active and passive IR sensors in a spectral band of 8-14µm and with temperatures ranging from 25 to 120°C. In order to measure total hemispheric emissivity, the apparatus uses an active source and an IR detector connected to the controlling block through optical fibre cables. The apparatus developed for measuring emissivity was presented in Ref [3]. Tangent lines in the hysteresis loops give the value of the phase transformation temperatures of the specimens according to the F2005 ASTM standard. Differential scanning calorimeter (DSC 8500 model, PerkinElmer[®]) was used to estimate the transformations temperatures of the material when no stress is applied, then its results can be used to compare this work results.

3. EXPERIMENTAL RESULTS

Figure 1 shows the change in hysteresis loops in the early cycles. (strain vs temperature plot during cycling). Table 1 summarizes the Phase transformation temperatures obtained. As it can be observed, phase transformation temperatures differed below in all cases.

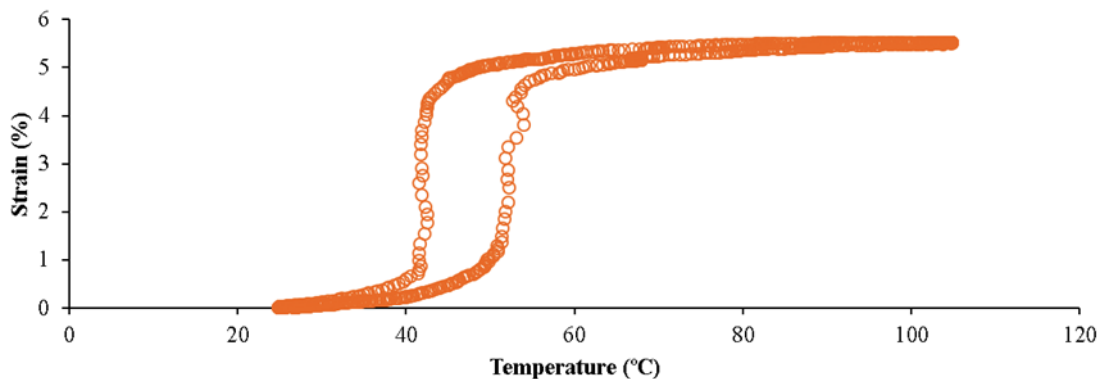


Figure 1. Early hysteresis loop of a NiTi alloy subject to thermal cycles and 150 MPa stress.

Table1. Phase transformation temperature of wire.

<i>SmartFlex</i> [®] 150	Phase transformation temperatures				Hysteresis
	M_f (°C)	M_s (°C)	A_s (°C)	A_f (°C)	$(A_p - M_p)$ (°C)
Experimental	41.40	44.58	49.70	55.80	-
DSC test	38.38	41.39	83.42	87.48	44.29

The difference observed between the transformation temperatures is justified, in part, by the changes that occur in the microstructure due to thermomechanical cycling [1].

4. CONCLUSIONS

The evolution of transformation temperatures and hysteresis loops was experimentally analysed utilizing a sensitive optical system equipped with IR sensor to measure the temperature. For the temperature range analysed, data reveal that sensors can be used to estimate the temperature of thin SMA actuators (≤ 500 micrometers), despite its difficulty to focus on. Any movement disorder between the sensor and the specimen resulted in oscillation in hysteresis loops plots. More samples should be analysed to verify the evolution of transformation temperatures of Shape Memory Alloy actuator wires subjected to thermal cycles. Differential scanning calorimeter (DSC) can be used to estimate the transformations temperatures of the material when no stress is applied, then its results can be used to compare this work results.

ACKNOWLEDGMENTS

This work has been supported by the ANP (Brazil's National Oil, Natural Gas and Biofuels Agency, Grant PRH-ANP/MCT number 48610.201153/2019-39).

REFERENCES

- [1] A.R. Pelton, G.H. Huang, P. Moine, R. Sinclair. Effects of thermal cycling on microstructure and properties in Nitinol. [*Materials Science and Engineering: A*, **532**, 130-138, \(2012\)](#).
- [2] MMSF Nascimento, CJ Araújo, JS Rocha Neto AMN Lima, Electro-Thermomechanical Characterization of Ti-Ni Shape Memory Alloy Thin Wires. [*Materials Research*, **9** \(1\), 15-19 \(2006\)](#).
- [3] TC Da Silva, et al. Emissivity Measurements on Shape Memory Alloys. In: [*Quantitative Infrared thermography conference, QIRT \(2016\)*](#).

Free vibration analysis of rotating single walled carbon nanotubes resting in elastic medium

Abdelkadir Belhadj^{1,2 *}, Abdelkrim Boukhalfa² and Sid. A. Belalia²

¹ DC Engineering & Project Management, Sonatrach, Algiers, Algeria

² Computational Mechanics Laboratory, Department of Mechanical Engineering,
Faculty of Technology, University of Tlemcen, Tlemcen, Algeria

*Corresponding author, e-mail address: abdelkadir.belhadj@univ-tlemcen.dz

Abstract

In this paper, a computational structural dynamic analysis based on Eringen's elastic constitutive model is done to investigate the free vibration of SWCNT resting in an elastic medium of Winkler type. The theory of nonlocal elasticity is applied on the classical Hooken equations, Governing equations have been generated by applying the Hamilton's principles. For solving differential equations system, the generalized differential quadrature method (GDQM) has been chosen to discretize the equations; a new technique for boundary conditions imposition has been used in the Matlab's code. The effect of the elastic coefficient parameter on the rotation of the small scale structure is discussed in order to understand the behaviour of the spinning SWCNT embedded in an elastic medium. Results of this study can serve as good guidance for next generation nano-machines.

Key Words: Vibration, SWCNT, GDQM, Rotation, Nanobeam

1. INTRODUCTION

As many sciences and techniques are involved in various engineering and domestic applications, nanomaterials are achieving significant attractiveness in modern nanotechnologies. Due to their exceptional physical, chemical, mechanical and electrical properties, researchers in nanomechanics have conducted many researches to develop new nanomaterials using different emerging techniques to understand their behavior. Nanostructures are widely used as nanobeams, nanoplates and nanoshells, nanobeams based single walled carbon nanotubes (SWCNT) [1] are applied as nanosensors, nanoprobes, nanowires, nano-resonators, nano-actuators, material reinforced nanostructure. Belhadj et al. [2-4] have studied the vibration of rotating SWCNT by using the Euer-Bernouli beam model and nonlocal elasticity; they have investigated the effect of boundary conditions, small-scale effect and the angular velocity on the fundamental frequency parameters. Hussain et al. [5] have investigated the characteristics of rotating functionally graded cylindrical shell resting on Winkler and Pasternak elastic foundation; they have examined the effect of elastic medium with the simply supported edge. Kumar Jena et al. [6] studied the free vibration of single walled carbone nanotubes resting on exponentially varying elastic foundation using the differential quadrature method; they have shown the effect of the elastic foundation on the fundamental frequency for different boundary conditions.

2. ERINGEN'S THEORY OF NONLOCAL ELASTICITY

Eringen [7] has introduced the theory of non-local elasticity to account for the small-scale effect. Unlike the classical theory of elasticity, the non-local theory consider long-range inter-atomic interaction and yields results dependent on the size of a body. In the following, the simplified form of the Eringen's nonlocal constitutive equation is employed:

$$[1 - (e_0 a)^2 \nabla^2] \sigma^{nl} = \sigma^l \quad (1)$$

where ∇^2 is the Laplacian operator, $(e_0 a)^2$ is nonlocal parameter,

a - internal characteristic length

e_0 - constant.

nl - non local

l - local

3. TRANSVERSE VIBRATION OF A ROTATING SWCNT EMBEDDED IN AN ELASTIC MEDIUM

The aim purpose of this study is to model the free vibration of a rotating SWCNT (Figure 1) by using Euler-Bernoulli beam theory, equations of motion to be developed using Hamilton's principle of virtual works.

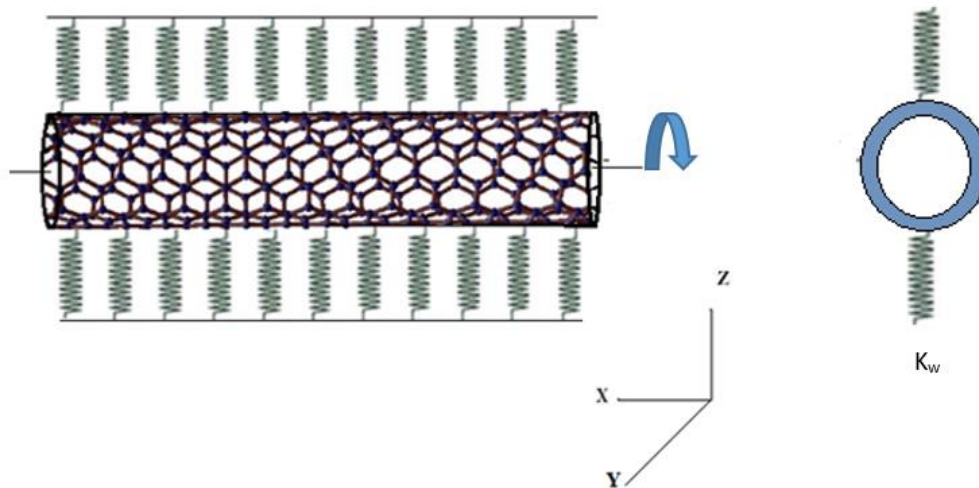


Figure 1. SWCNT embedded in an elastic medium.

By using Bernoulli principle:

$$\int_{t_1}^{t_2} (\delta U + \delta V - \delta K) dt = 0 \quad (2)$$

Whereas: $\delta U, \delta V, \delta K$ are the strain energy variation, potential energy variation and the kinetic energy variation, respectively.

The governing equations system is developed as following:

$$N - (e.a)^2 \frac{d^2 N}{dx^2} = EA \frac{du}{dx} \quad (3)$$

$$M_y - (e.a)^2 \frac{d^2 M_y}{dx^2} = EI \frac{d^2 v}{dx^2} \quad (4)$$

$$M_y - (e.a)^2 \frac{d^2 M_y}{dx^2} = EI \frac{d^2 v}{dx^2} \quad (5)$$

By replacing the expressions of N, M_y and M_z

$$\rho A \left[\ddot{u} - (e.a)^2 \frac{d^2 \ddot{u}}{dx^2} \right] = EA \frac{d^2 u}{dx^2} \quad (6)$$

$$\rho A \left[\ddot{v} - (e.a)^2 \frac{d^2 \ddot{v}}{dx^2} \right] + \rho I \left[\dot{v} - (e.a)^2 \frac{d^2 \dot{v}}{dx^2} \right] - 2\Omega \left(\dot{w} - (e.a)^2 \frac{d^2 \dot{w}}{dx^2} \right) = EI \frac{d^4 v}{dx^4} \quad (7)$$

$$\rho A \left[\ddot{w} - (e.a)^2 \frac{d^2 \ddot{w}}{dx^2} \right] + \rho I \left[\dot{w} - (e.a)^2 \frac{d^2 \dot{w}}{dx^2} \right] + 2\Omega \left(\dot{v} - (e.a)^2 \frac{d^2 \dot{v}}{dx^2} \right) = EI \frac{d^4 w}{dx^4} \quad (8)$$

Longitudinal, lateral and transverse deflection to be respectively:

$$u(x, t) = ue^{i\omega t}, v(x, t) = ve^{i\omega t}, w(x, t) = we^{i\omega t}$$

By introducing, the elastic foundation where the nano SWCNT is resting:

$P(x) = -kx$ exanimated on the SWCNT because of the elastic medium which is opposite to the deviation of the nanostructure, this expression is also effected by the nonlocal model as:

$$P(x) - (e.a)^2 \frac{d^2 p(x)}{dx^2} = -k \left[w - (e.a)^2 \frac{d^2 w}{dx^2} \right] \quad (9)$$

$$-\rho A \omega^2 \left(1 - (e.a)^2 \frac{d^2}{dx^2} \right) u - EA \frac{d^2 u}{dx^2} = 0 \quad (10)$$

$$\begin{aligned} -\rho A_y \omega^2 \left(1 - (e.a)^2 \frac{d^2}{dx^2} \right) v + \rho I \omega \cdot j \left(1 - (e.a)^2 \frac{d^2}{dx^2} \right) v - 2\Omega \left(1 - (e.a)^2 \frac{d^2}{dx^2} \right) j \omega w \\ - EI \frac{d^4 v}{dx^4} + k \left[v - (e.a)^2 \frac{d^2 v}{dx^2} \right] = 0 \end{aligned} \quad (11)$$

$$\begin{aligned} -\rho A_z \omega^2 \left(1 - (e.a)^2 \frac{d^2}{dx^2} \right) w + \rho I \omega \cdot j \left(1 - (e.a)^2 \frac{d^2}{dx^2} \right) w + 2\Omega \left(1 - (e.a)^2 \frac{d^2}{dx^2} \right) j \omega v \\ - EI \frac{d^4 w}{dx^4} + k \left[w - (e.a)^2 \frac{d^2 w}{dx^2} \right] = 0 \end{aligned} \quad (12)$$

4. GENERALIZED DIFFERENTIAL QUADRATURE METHOD

Generalized differential quadrature method (GDQM) [8-9] is widely used for solving multiscale applied mechanics problems; its philosophy is based on computing the derivatives of the functions constituting the governing equation. Each derivative is formulated by a sum of values at its neighboring points.

$$\left. \frac{d^n f}{dx^n} \right|_{x=x_i} = \sum_{j=1}^N C_{ij}^{(n)} f(x_j) \quad i = 1, 2, \dots, N; n = 1, 2, \dots, N - 1 \quad (13)$$

Where $C_{ij}^{(n)}$ is the weighting coefficient of the n th order derivative, and N the number of grid points of the whole domain, ($a = x_1, x_2, \dots, x_i, \dots, x_N = b$)

According to Shu and Richard rule [13], the weighting coefficients of the first-order derivatives in direction ξ , ($\xi = \frac{x}{L}$) are determined as:

$$C_{ij}^{(1)} = \frac{P(\xi_i)}{(\xi_i - \xi_j) \cdot P(\xi_j)} \quad i, j = 1, 2 \dots N, i \neq j \quad (14)$$

$$C_{ij}^{(1)} = - \sum_{\substack{j=1 \\ j \neq i}}^N C_{ij}^{(1)}$$

Where: $P(\xi_i) = \prod_{j=1}^N (\xi_i - \xi_j) \quad i \neq j$

The second and the higher order derivatives can be computed as:

$$C_{i,j}^{(2)} = \sum_{k=1}^N C_{i,k}^{(1)} \cdot C_{k,j}^{(1)} \quad i = j = 1, 2 \dots N. \quad (15)$$

$$C_{i,j}^{(r)} = \sum_{k=1}^N C_{i,k}^{(1)} \cdot C_{k,j}^{(r-1)} \quad i = j = 1, 2 \dots N.$$

$$r = 2, 3 \dots m \quad (m < N)$$

Throughout the paper, the grid points are assumed based on the well-established Chebyshev-Gauss-Lobatto points

$$\xi_i = \frac{1}{2} \left(1 - \cos \frac{(i-1)\pi}{N-1} \right) \quad i = 1, 2 \dots N \quad (16)$$

the boundary conditions used for the free vibration of rotating nonlocal shaft are:

Simply supported beam

$$w(\xi = 0) = \frac{\partial^2 w(\xi=0)}{\partial \xi^2} = 0 \quad \text{and} \quad w(\xi = 1) = \frac{\partial^2 w(\xi=1)}{\partial \xi^2} = 0 \quad (17)$$

Let us introduce the following non-dimensional terms:

$$\xi = \frac{x}{L}, \quad U = \frac{u}{L}, \quad V = \frac{v}{L}, \quad W = \frac{w}{L}$$

$\lambda^2 = \frac{EI}{\rho AL^4} \omega^2$ the frequency parameter

The angular velocity parameter $\gamma^2 = \frac{\rho A \Omega^2 L^4}{EI}$ the hubradius $\delta = \frac{x}{L}$

$K = \frac{kL^4}{EI}$ The winkler elastic modulus parameter, $\mu = \frac{e_0 a}{L}$ the nonlocal parameter

The equations (10), (11) and (12) become than:

$$\frac{\lambda^2}{L^2} \left(1 - \mu^2 \sum_{j=1}^N B_{i,j} \right) U_j - EA \sum_{j=1}^N B_{i,j} U_j = 0 \quad (18)$$

$$\begin{aligned}
 & -\lambda^2 \left(1 - \mu^2 \sum_{j=1}^N B_{i,j} \right) V_j + \Gamma \cdot \lambda \cdot j \left(1 - \mu^2 \sum_{j=1}^N B_{i,j} \right) V_j + \frac{2\gamma^2}{\rho\pi\delta^2 L^2} \cdot j \left(1 - \mu^2 \sum_{j=1}^N B_{i,j} \right) W_j \\
 & - \sum_{j=1}^N D_{i,j} V_j + K \left[1 - \mu^2 \sum_{j=1}^N B_{i,j} \right] V_j = 0
 \end{aligned} \tag{19}$$

$$\begin{aligned}
 & -\lambda^2 \left(1 - \mu^2 \sum_{j=1}^N B_{i,j} \right) W_j + \Gamma \cdot \lambda \cdot j \left(1 - \mu^2 \sum_{j=1}^N B_{i,j} \right) W_j + \frac{2\gamma^2}{\rho\pi\delta^2 L^2} \cdot j \left(1 - \mu^2 \sum_{j=1}^N B_{i,j} \right) V_j \\
 & - \sum_{j=1}^N D_{i,j} W_j + K \left[1 - \mu^2 \sum_{j=1}^N B_{i,j} \right] W_j = 0
 \end{aligned} \tag{20}$$

5. RESULTS AND DISCUSSIONS

In this section, results of our study are reported here after solving a complex Eigen problem by developing a Matlab code using GDQM technique. The nonlocal governing differential equation is solved using sufficient numbers of grid points which is taken as 15 as prove our previous studies. The effects of elastic medium, of small-scale parameter or nonlocal parameter, lower and higher angular velocities are investigated, and the related graphs are plotted. For the present study, the properties of the nonlocal nanobeams are considered that of a SWCNT. An armchair SWCNT with chirality (5,5) is considered. With a Young's modulus $E=2.1$ TPa, the length- radius ration is taken as $L=80d$, $d=1$ nm, a density $\rho=7800$ kg/m³, and a moment of inertia $I=\pi d^4/64$.

The validation of our results have been insured by comparing the flexural frequency parameters with Chakraverty [10] results for simply supported beam simply supported beam. Table 1 shows that the first four frequency parameters computed by as present good agreement with those cited in literature.

Table 1. Comparison of First four frequency parameters of Euler-Bernoulli nanobeam for different boundary conditions and scaling effect parameters.

	$\mu^2 = 0$		$\mu^2 = 0.3$		$\mu^2 = 0.5$	
	<u>Present</u>	<u>Chakraverty[14]</u>	<u>Present</u>	<u>Chakraverty</u>	<u>Present</u>	<u>Chakraverty</u>
SS	3.1416	3.1416	2.6800	2.6800	2.3022	2.3022
	6.2832	6.2832	4.3013	4.3013	3.4404	3.4604
	9.4243	9.4248	5.4413	5.4422	4.2885	4.2941
	15.5035	15.5665	6.3646	6.3633	4.9731	4.9820

We define the variations of the frequency parameter λ^* and the variation of the angular velocity parameter γ^* :

$$\lambda^* = \frac{\lambda}{\lambda_0} \quad \gamma^* = \frac{\gamma}{\lambda_0}$$

λ_0 : frequency parameter at a zero angular velocity. $\lambda_0 = \lambda_{0f} = \lambda_{0b}$

λ : other frequency parameter.

The table 2 presents the variation of the forward and backward frequency parameters with the variation of the nonlocal parameter and the Winkler elastic parameter for a simply supported beam. It is remarkable that the frequency parameter has decreased since the nanorotor was embedded in an elastic medium. By increasing the winkler elastic parameter K ($K=10^2, 10^3, 10^4$) the frequency parameter decreased, By going up through the small scale the frequency parameter become smaller than the local ones ($\mu^2=0$).

Figure 2 shows the Campbell diagram for different Winkler elastic parameter for simply supported nanorotor, it shows that the backward frequency parameter is decreasing with the increase of the Winkler elastic parameter and the forward frequency parameter inversed when $\gamma^* = 1$, this is due to the mathematical ratio effect. The angular velocity parameter can have a crucial effect on the stability of the system at weak elastic foundations. So, since the elastic foundation (stiffness) is important the frequency parameters are decreasing.

Table 2 Frequency parameters for different nonlocal parameter and different Winkler elastic medium for simply supported beam.

K	γ	$\mu^2 = 0.1$		$\mu^2 = 0.3$		$\mu^2 = 0.5$	
		λ_b	λ_f	λ_b	λ_f	λ_b	λ_f
10²	0	2,7341	2,7341	2,4031	2,4031	2,0252	2,0252
	1	2,4103	3,2669	2,1174	2,7093	1,7488	2,3345
	2	2,0917	3,5386	1,8674	3,0152	1,4724	2,6444
	3	1,763	3,8103	1,5453	3,3217	1,1961	2,9542
	4	1,4397	4,082	1,2590	3,6277	0,9193	3,2636
	5	1,0341	4,3537	0,9733	3,9333	0,6434	3,5732
10³	0	2,6198	2,6198	2,1785	2,1785	1,8409	1,8409
	1	2,296	3,1526	1,8547	2,7113	1,5171	2,3737
	2	1,9774	3,4243	1,5361	2,983	1,1985	2,6454
	3	1,6487	3,696	1,2074	3,2547	0,8698	2,9171
	4	1,3254	3,9677	0,8841	3,5264	0,5465	3,1888
	5	1,0198	4,2394	0,7785	3,7981	0,3809	3,4605
10⁴	0	2,5203	2,5203	2,142	2,142	1,7847	1,7847
	1	2,1965	3,0531	1,8182	2,6748	1,4609	2,3175
	2	1,8779	3,3248	1,4996	2,9465	1,1423	2,5892
	3	1,5492	3,5965	1,1709	3,2182	0,8136	2,8609
	4	1,2259	3,8682	0,8476	3,4899	0,4903	3,1326
	5	1,1203	4,1399	0,7142	3,7616	0,3847	3,4043

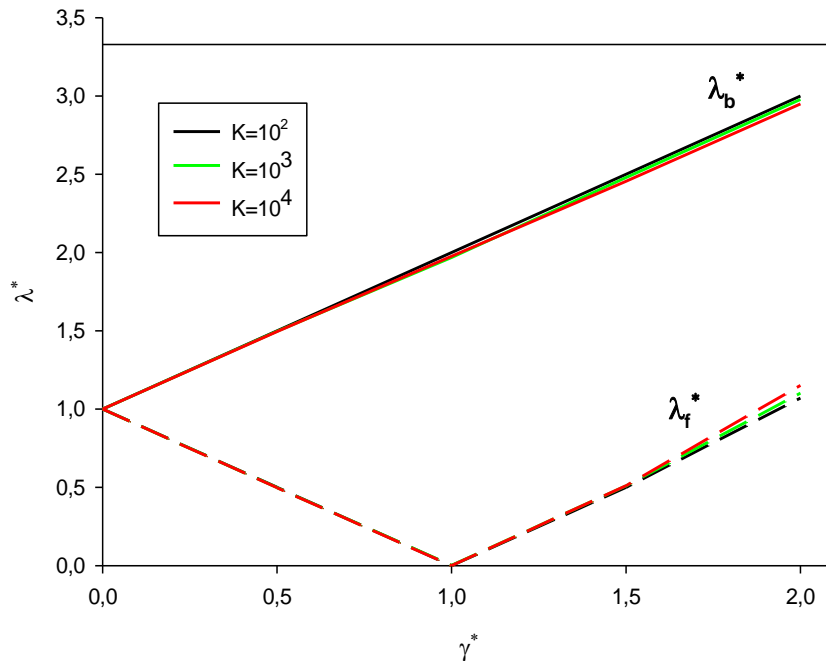


Figure 2. Campbell diagram for different Winkler elastic parameter for simply supported nanorotor.

Figure 3 illustrated the variation of the frequency parameter with the variation of the angular velocity (Campbell diagram) for different nonlocal parameter; it is remarkable that the increase of the nonlocal parameter has decreased the variation of the frequency parameter since a known value of angular velocity parameter.

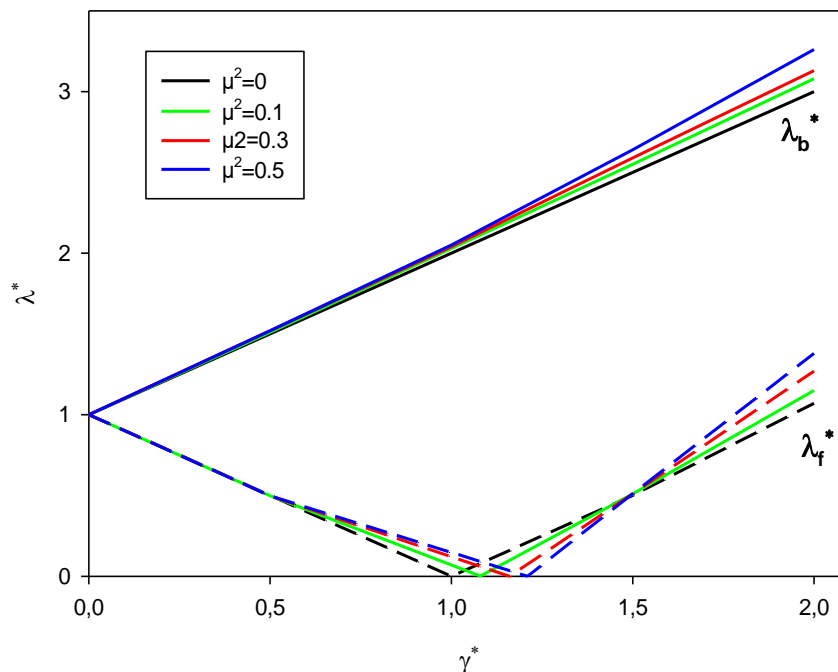


Figure 3. Campbell diagram for different nonlocal parameter for simply supported beam.

CONCLUSION

In this paper, a free vibration analysis has been studying the rotary inertia of single walled carbon nanotubes resting in an elastic medium of Winkler type, governing equations have been generated based on Hamilton principle and getting discretised using the generalized differential quadrature method for a simply supported boundary condition. Obtained results are found having good agreement with other studies, Campbell diagrams have been employed to show the rotary inertia behaviour of the spinning SWCNT inside elastic foundation.

The Winkler elastic parameter has affected the frequency parameters (backward and forward), and the angular velocity parameter. By improving the elastic parameter the frequency parameters decreased. The nonlocal parameter has also an inverse effect on the frequency parameters.

In this study, the effect of the elastic coefficient parameter on the rotation of the small scale structure is discussed in order to understand the behavior of the spinning SWCNT embedded in an elastic medium that can serve as good guidance for next generation nano-machines.

REFERENCES

- [1] S. Iijima, *Nature* **345**, 56-58 (1991).
- [2] A. Belhadj, A. Boukhalfa, and S. A. Belalia, *Eur. Phys. J. Plus*, **132**, 513 (2017).
- [3] A. Belhadj, A. Boukhalfa, and S. A. Belalia, *Nanomat. Sci. & Eng.*, **2** (3), 103-112. (2020).
- [4] A. Belhadj, A. Boukhalfa, and S. A. Belalia, *Mathematical Modelling of Engineering Problems*, **4**(1), 33-37, (2017).
- [5] M. Hussain, M. N. Naeem, M. R. Inventible, *Proc IMechE Part C: J Mechanical Engineering Science*, 4342-4356 2018.
- [6] S. K. Jena, S. Chakraverty, *Curved and Layer. Struct.*, **5**, 12874-8 (2018).
- [7] A.C. Eringen, *J. Appl. Phys.* **54**, 4703-4710 (1983).
- [8] R. Bellman, B.G. Kashef, J. Casti, *J. Comput. Phys.* **10** (40), 40-52 (1972).
- [9] C. Shu, B.E. Richards, in Proceedings of 3rd International Conference on Advanced in numerical Methods in Engineering: Theory and Applications, Swansea, Vol. 2, 978-985 (1990).
- [10] S. Chakraverty, L. Behera, *Physica E* **67**, 38-46 (2015).

Modeling and computational study of structures and physical properties of hydroxyapatite containing various defects: a review

V. S. Bystrov¹ *, E. V. Paramonova¹, A. V. Bystrova^{1,5}, L. A. Avakyan²,
J. Coutinho³, N. V. Bulina⁴

¹ *Institute of Mathematical Problems of Biology, Keldysh Institute of Applied Mathematics, RAS, Pushchino, 142290, Russia*

² *Physics Faculty, Southern Federal University, Rostov-on-Don 344090, Russia*

³ *Department of Physics and I3N, University of Aveiro, 3810-193 Aveiro, Portugal*

⁴ *Institute of Solid State Chemistry and Mechanochemistry, Siberian Branch, Russian Academy of Sciences, Novosibirsk, 630128 Russia*

⁵ *Riga Technical University, Riga, LV-1658, Latvia*

*Corresponding author, e-mail address: vsbys@mail.ru

Abstract

This review presents modeling and computer studies of the structural and physical properties of hydroxyapatite (HAP) containing various defects. HAP is a well-known material that is actively used in various fields of medicine (bone and dental implantology) and nanotechnology, in ecology and photocatalytic processes, and even in the fight against cancer (as a means of targeted drug delivery). However, all the features of the structure and properties of HAP, especially their changes under the influence of various HAP defects, are still insufficiently studied. At present, more and more theoretical studies of HAP, both stoichiometric and HAP with various defects, are being carried out using modern density functional theory (DFT) methods with hybrid functionals and the theory of many-particle perturbations. First of all, oxygen and OH group vacancies are important defects in HAP, which significantly affect its properties. The properties of HAP are also influenced by various interstitials and substitutions of atoms in the HAP crystal lattice by others. This review article presents and analyses the results of calculations by various DFT methods of HAP structures with these different defects, primarily with oxygen and hydroxyl vacancies. Comparative analysis of calculations by different methods is carried out. The results obtained show that after the computer structural optimization of HAP with various defects, not only the parameters of the crystallographic cells of the HAP change, but also their properties such as electronic, optical, and mechanical. This leads to a significant change in the entire energy band structure of HAP, which affects electronic transitions and changes the effective band gap, etc. The paper analyses the obtained results of modeling and calculations of HAP containing various defects, the applied calculation methods and the features of the effect of defects on the properties of HAP, which are important for practical applications.

Key Words: Hydroxyapatite, Modeling and calculations, Density functional theory, Defects, Vacancies, Interstitials, substitutions, Structural properties, Optical properties, Band gap, Nanomaterials, Implants

1. INTRODUCTION

Recent studies of the structure and physicochemical properties of hydroxyapatite (HAP) have convincingly shown that real samples (both natural and synthetic), especially of biological origin (from the bone tissues of mammals, fish, and molluscs), are quite different from ideal ones crystallographic models of HAP [1-6]. It turned out that these HAP structures with defects that promote better biocompatibility, adhesion, attachment of the bone cells and their proliferation, since they are closer to biological HAP, which has its own structural heterogeneities [1-4]. But what properties are most important here?

HAP samples with defects close to biological ones have not only “incorrect” stoichiometry (their composition, as a rule, differs from the Ca/P ratio ~ 1.67 [9-12]), but also have a number of numerous defects (oxygen vacancies and whole OH groups, impurities, interstitials and substitutions of a number of atoms in the crystallographic lattice) [13 – 22]. Moreover, the distribution of all these defects in the sample volume is uneven, stochastic and depends on many conditions: temperature, pressure, heating and cooling rates, the composition of the environment, humidity, etc. [19]. It is clear that theoretical models and any high-precision calculations using a variety of modern methods reflect only part of this complex multicomponent system of heterogeneous HAP structures. Nevertheless, developing these models and carrying out more and more detailed calculations, we can distinguish the features of various studied structural defects and correlate their properties with the experimentally observed data [4-9].

Thus, various defects have different effects on the change in the properties of a regular HAP periodic lattice. At the same time, it is known that the basic structure of HAP has such characteristic features as extended structural channels formed by OH groups [5-9, 13, 16]. This feature leads to the possibility of proton movement along these channels [16, 17] and the appearance in HAP of defects such as vacancies of protons, oxygen, and whole OH groups [2, 4, 5, 7, 9, 14-20]. When the sample is heated to certain temperatures (about $\sim 500-700$ °C or about $\sim 700-900$ K [16-20]), OH groups leave the samples quite easily and HAP is dehydrated [7, 19, 20]. During subsequent cooling, OH groups from the environment are reintroduced into the channels. But their concentration changes (depending on the humidity of the environment, etc.) and a partial concentration of OH vacancies will remain in the sample, which significantly affects their properties [2, 4, 19, 20].

Other characteristic defects in HAP are oxygen vacancies [2, 4-6, 8, 9, 21, 22]. Moreover, they can be both from the OH group and from the PO₄ group (and of different types depending on the position of the oxygen atom and the symmetry of the given atomic group [8]). Their formation is possible at higher temperatures (of the order of $\sim 1100 - 1300$ °C or about $\sim 1000 - 1100$ K) [19, 20] or under radiation exposure [23].

The next important defects are possible interstitials (in particular, the insertion of hydrogen atoms or protons [2, 4, 5]) and replacement of atoms in the structure of HAP by others atoms in HAP unit cell lattice (for example, Fe/Ca, Sr/Ca [5, 24-29]) and others (such as Mg/Ca, Se/Ca, Si/P, etc) [5]. It is very important for many practical applications, because it changes the HAP surface electrical potential [2, 4] and leads higher adhesion and proliferation of various osteo-cells on HAP surface, that improves the biocompatibility of the implant.

Basically, the properties of HAP are determined precisely by the presence of various structural defects, such as oxygen and hydroxyl vacancies, interstitials and substitutions of ions, atoms in the structure of HAP [1-4]. Various modern methods of computer modeling and calculations are used to study them, including first principles *ab initio* and density functional theory (DFT) methods [5 - 9, 30-51].

During last time, using modern methods of density functional theory (DFT) and new software tools (AIMPRO, VASP, and Quantum Espresso (QE) [7, 8, 38-52]) in modeling and computer studies of the properties of HAP structures with these different types of defects, it was found that the forbidden band gap E_g of an ideal (defect-free) HAP lattice turns out to be much larger than the data of measurements of the optical absorption characteristics of usual HAP samples [2, 4, 18, 19] show, and can reach values of the order of $\sim 7.4 - 7.8$ eV [7, 35]. That is, this significantly exceeds the experimentally observed values for the HAP samples used in practice ($E_g \sim 4 - 5$ eV) [2, 4, 9, 20]. These recent model studies of the HAP structure with defects have convincingly shown that the deviations of the calculated band gap E_g of the ideal stoichiometric HAP crystal from the experimentally recorded values are caused precisely by the presence of defects in the HAP structure [2, 4-9, 36, 37].

Recently, calculations of oxygen vacancies (from PO_4 and OH groups with different symmetry) and total OH-group vacancies in the HAP structure were carried out and these oxygen and OH vacancies were investigated both in the local charge density approximation (LDA) of density functional theory (DFT) [5, 6, 38, 42,43] and in the generalized gradient approximation (GGA) of DFT [48 -50], including the use of the modern new types of hybrid DFT functionals and the theory of many-particle perturbations [7, 8, 39, 41, 44-52]. These studies of the structural and electronic properties of oxygen vacancies using hybrid DFT functionals were carried out both in the single unit cell model and in the model of large HAP supercell model ($2 \times 2 \times 2 = 8$ unit cells) [7, 8] in the plane wave formalism [46, 47, 51] and in the GGA [48-50].

These calculations and studies have shown that, under equilibrium conditions, oxygen vacancies arise not only in the form of a simple vacant oxygen site (in a neutral charge state) [8], but can also be in the form of extended structures occupying several crystal fragments (especially in a double plus charge state) [8, 36, 37]. In this case, the connection between the presence of defects and changes in the optical properties of HAP and the level of its photoelectronic work function is clearly traced [2, 4, 5]. In fact, for any different approaches and methods of DFT calculations, it is oxygen vacancies that play their decisive role here, changing the optical absorption width E_g of an ideal HAP crystal from its large characteristic values to a lower level of the order of $\sim 3.6 - 4.2$ eV, which is usually recorded on HAP experimental samples.

It is important to note that the possible levels of optical absorption for OH vacancies in HAP, established in this case in the calculations, lie in the region of $\sim 1.6 - 2.0$ eV and they are practically not observed in the experiment, even at a significant concentration of OH vacancies. However, in this case, in general, an increase in the optical absorption of HAP samples up to the value $E_g^* \sim 5.3 - 5.4$ eV is observed. Based on the analysis of the calculated density of electronic states (DOS) of HAP data, this can be explained by the fact that in this case the intensity of the recorded peak of DOS from OH vacancies (located approximately in the middle

of the band gap) turns out to be very low in comparison with the intensity of the main DOS peaks (especially, the top of the valence band E_v and the bottom of the conduction band E_c , that determine the usual forbidden band gap $E_g = E_c - E_v$). Therefore, this transition is difficult to detect experimentally. This turns out to be possible only by the photo-luminescence method, upon excitation of a significant number of electrons and from deep valence band levels into the conduction band by the method of synchrotron irradiation [53]. However, in this case, the changed value of the band gap E_g is experimentally recorded. These questions, as well as the questions of statistics (and dynamics) of accumulation and annealing of defects in different unit cells of the entire volume of the crystal, remain so far rather difficult problems for further research.

It should be noted that, as already indicated above, in [8], the possibility of the existence in HAP, in addition to the usual neutral oxygen vacancies, also of charged oxygen vacancies, was shown. Moreover, these charged vacancies (with a charge $Q = +1, +2$) create not point defects, but formations extended in space [8]. These new structural extended (or bridging structures) defects can play an important role in changing the properties of electrically charged HAP. The study of transitions between the energy levels of such more complex defects (including at different levels of the charge state of the HAP crystal, and different types of its conductivity: electron n-type, or hole p-type) showed that the transition of electrons can also include a phononless transition with energy $\sim 3.6\text{--}3.9$ eV [8, 36, 37]. This mechanism can also explain the onset of absorption at $3.4\text{--}4.0$ eV in the experimental observation of photocatalysis in HAP under constant UV illumination (along with other approaches associated with the formation of oxygen vacancies in HAP from PO_4 groups, etc.). Moreover, here it is also necessary to take into account the Franck-Condon effect influence [36,37].

In general, these studies are still far from complete and require further continuation. In this review, we present some recent and also new data on the study of defects, primarily oxygen vacancies of various types and vacancies of the OH group, obtained by various modern methods of computer simulation and quantum mechanical calculations.

2. COMPUTATIONAL DETAILS AND MAIN MODELS

The calculations of pristine and defective HAP structures and properties were carried out from first principles using DFT by AIMPRO code (in Local Density Approximation (LDA)) [5, 6, 38, 42, 43] and by VASP [7, 8, 39, 44-48] (in Generalized Gradient Approximation (GGA) according to Perdew, Burke, Ernzerhof (PBE) approach [49] and with Becke three-parameter (B3LYP) hybrid functional [49, 50]) in partial combination with semi-empirical quantum-chemical (QM) PM3 method from HypemChem 8.0 package [40]. More computational details are all described in works [5 - 8]. Some recent calculations were made using Quantum ESPRESSO [41]. Some earlier calculations were performed using one unit cell model of hexagonal HAP P6_3 [5, 6] (see below Fig. 1 and Fig. 2). The main peculiarity of the next study is the introduction of the supercells model made up of $2 \times 2 \times 2 = 8$ polar HAP unit cells (space group P6_3) for hexagonal HAP phase both for pristine and defective HAP with OH and oxygen vacancies [7, 8] (see below Fig. 3).

3. MAIN RESULTS AND DISCUSSIONS

Hydroxyapatite (HAP) have the general chemical formula $\text{Ca}_5(\text{PO}_4)_3\text{OH}$ [10]. HAP solidifies in the form of an ionic molecular crystal, either of hexagonal ($\text{P6}_3/\text{m}$) or monoclinic ($\text{P2}_1/\text{b}$) symmetry, depending from conditions, and has unit cells enclose two or four formula units, respectively [10-13].

The crystal structure and unit cell parameters of HAP with both $\text{P6}_3/\text{m}$ and $\text{P2}_1/\text{b}$ symmetries, and its atomic positions, were determined using x-ray diffraction [11] (Table 1).

Table 1. Unit cell parameters a, b, c [Å] (from [11]).

Phase	Group	a , Å	b , Å	c , Å
Hexagonal	$\text{P6}_3/\text{m}$	9.417	9.417	6.875
Monoclinic	$\text{P2}_1/\text{b}$	9.480	18.960	6.830

HAP usually crystallizes in a hexagonal crystal system (space group $\text{P6}_3/\text{m}$) under normal conditions, according to temperature and stoichiometry, but can also exist as a monoclinic structure (space group $\text{P2}_1/\text{b}$) [1–5, 9–13]. As noted by Elliot [10], direct synthesis of monoclinic phase usually requires very strict adherence to the correct stoichiometry, with a Ca:P ratio of 1.67 [4, 9, 10–13].

One of the common structural peculiarities of HAP structure is connected with the pseudo-one-dimensional character of the apatite structure. Ca and OH^- ions form a long chain along the main structural c axis [9, 10–19], usually named the ‘columnar’ or ‘channel’ structure, often being named as an ‘OH-channel’ in HAP.

For the $\text{P6}_3/\text{m}$ phase consisting from two chemical formula units the HAP general formula is $[\text{Ca}_{10}(\text{PO}_4)_6(\text{OH})_2]$, where the hydroxyl units OH shows stochastic orientation along OH channels.

Thus, according to X-ray data, this actually makes the material mirror-symmetric along the main axis, which runs along the OH channel. Conversely, when all OH blocks show the same alignment along the hexagonal axis, the mirror plane is lost and the space group symmetry drops to P6_3 . The ordering of the dipoles in the OH-channels, which interact with the chains of the OH-channel, also affects the property of the monoclinic phase. If OH^- ions are oriented in parallel, HAP has non-centrosymmetric ordered structure (space group P2_1), which could reveal piezoelectric properties [17, 18, 36, 37].

The structure of HAP, used to study the effect of defects on its properties, is primarily based on its initial pristine stoichiometric structural phase – hexagonal P6_3 , with a unit cell consisting of 44 atoms and containing structural OH channels with 2 hydroxyl OH groups in each unit cell [5-9, 13-20]. Depending on the orientation of these OH groups, the cells can have different symmetry groups (Table 1): $\text{P6}_3/\text{m}$ - for the hexagonal disordered phase (when the orientation of the OH groups is random) and P6_3 - for the hexagonal ordered phase (when the orientation of the OH groups is parallel and directed in the same direction, which creates its own internal polarization, similar to ferroelectrics (see below, for example, in [36, 37])).

3.1. One unit cell model

First, we consider one unit cell model of hexagonal HAP ($P6_3$) lattice and several its defects, such as, OH-vacancy and O-vacancies. In this section we analyse the calculation results obtained by the DFT methods in local density approximation (LDA) using AIMPRO software [5, 38] and in generalized gradient approximation (GGA) using VASP [7, 8, 39] (and some recent using Quantum ESPRESSO [41]) software with various DFT functional PBE [48], including hybrid functional HSE [54] and B3LYP [49, 50]. The initial stoichiometric HAP unit cell for pure lattice in $P6_3$ hexagonal phase is presented on Fig. 1.

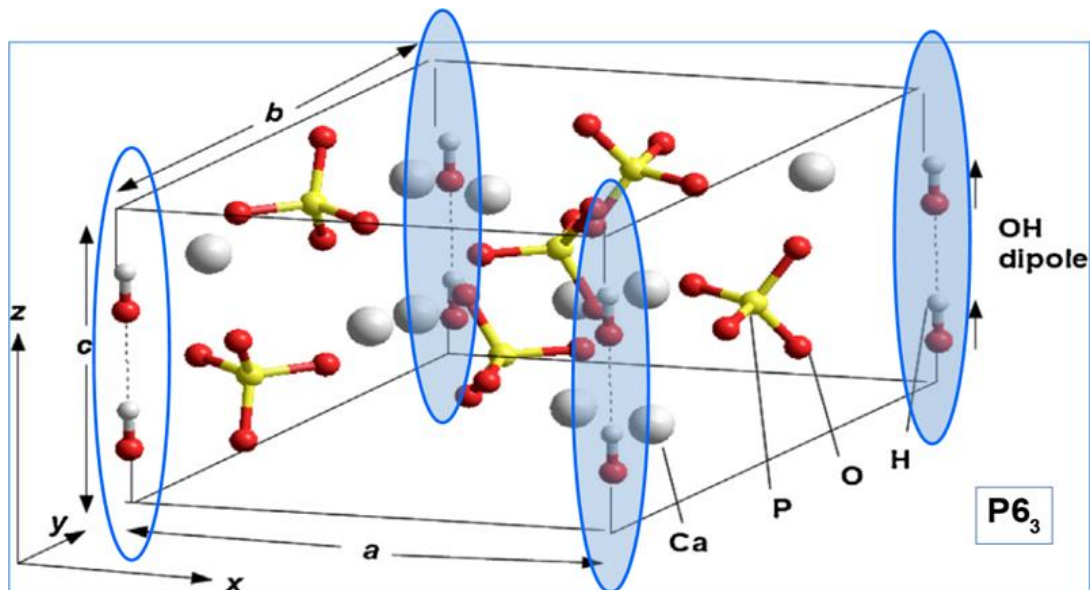


Figure 1. One unit cell model of the Hydroxyapatite (HAP: $\text{Ca}_{10}(\text{PO}_4)_6(\text{OH})_2$) – in $P6_3$ hexagonal phase. All OH groups are oriented in the same direction. They are positioned at the four corners of the unit cell, but only one pair in one corner belongs to this unit cell, the other three pairs belonging to neighbouring unit cells (e.g., one OH per unit cell). (modified and reproduced with permission from ref. [5]; IOP Publishing, 2015).

This HAP one unit cell consist from 44 atoms and contain two OH groups in each periodical unit cell. To indicate this moment in Fig. 1, one OH channel with 2 OH groups is marked with a transparent oval, and the other 3 OH channels are marked with semitransparent ovals (these $3 \times 2 = 6$ OH groups are not included in the unit cell and belong to other periodically repeating unit cells).

The HAP unit cell model, containing several defects in the atomic positions of all the vacancies used in this work, is shown in Fig. 2. Here we indicate OH-vacancy and various types of O-vacancies in the HAP unit cell, as deviations from the initial stoichiometric hexagonal HAP structure [6]: 1) An O-vacancy in the OH group of an OH-channel structure (blue circle in Fig. 2); 2) A full OH-vacancy from this OH-channel structure (purple circle in Fig. 2); 3) Various cases of O-vacancies from different positions in PO_4 groups (green circles in Fig. 2).

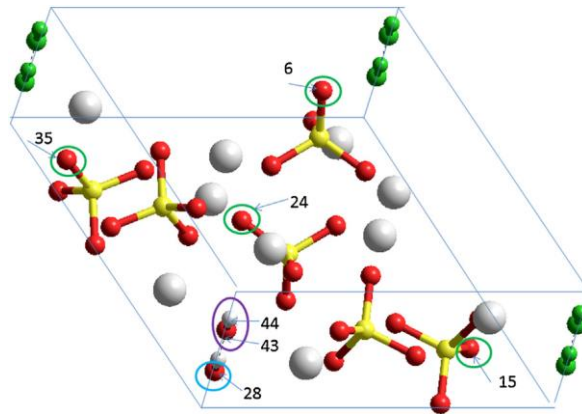


Figure 2. Models and scheme of the atomic positions selected and deleted for modelling presentation of various vacancy-defects in the HAP hexagonal unit cell with initial 44 atoms. Indicated in the coloured circles are: (1) in blue – oxygen atom (number 28) from an OH group for creation of an O-vacancy in the OH-channel; (2) in purple – OH group full (with atom numbers 43 and 44) for creation of a complete OH-vacancy; (3) in green – oxygen atoms (with numbers 6, 15, 24, 35) from various differently positioned PO_4 groups corresponding to an O-vacancy in PO_4 groups. The green atoms on the other three corners indicate other OH groups, which belong to neighbouring periodical repeated unit cells. (Reproduced with permission from ref. [6]; Elsevier, 2016).

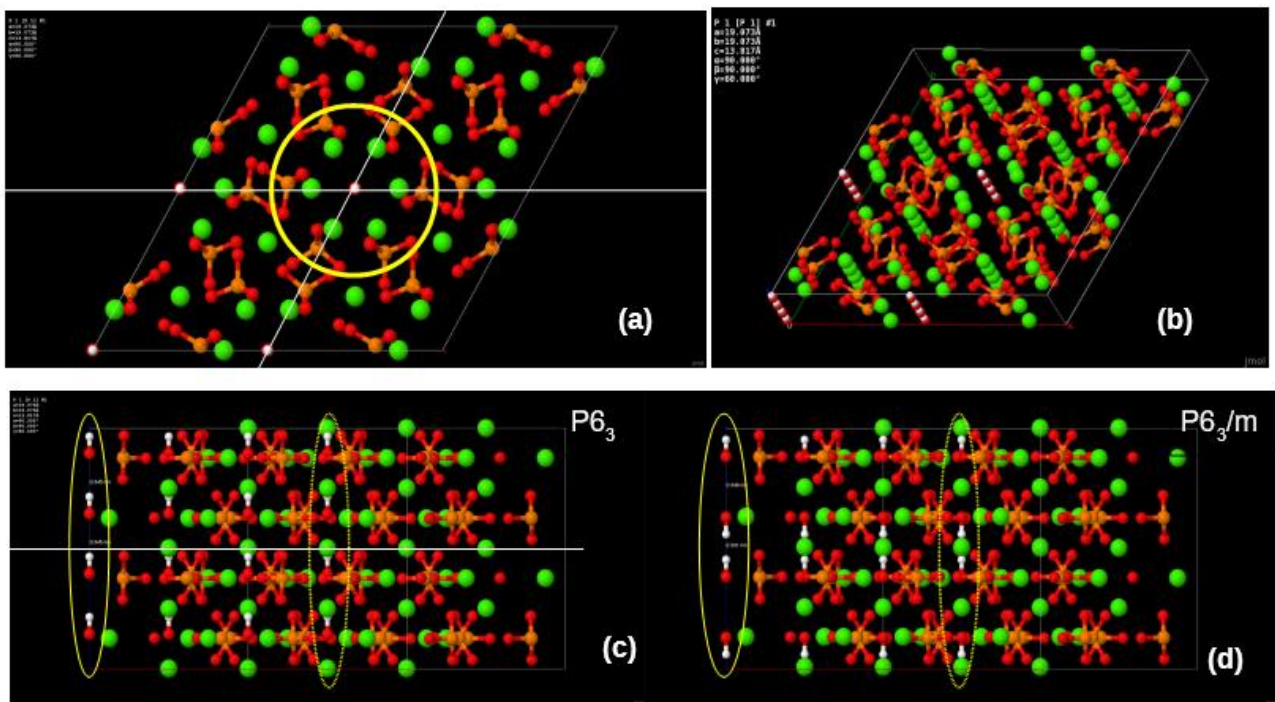


Figure 3. Images of supercell models with $2 \times 2 \times 2 = 8$ unit cells of HAP (visualization using Jmol after DFT calculations: a) top view - along the c axis of the OH channel (a yellow circle highlights the main central part around one OH channel); b) supercell model in isometric projection; c) HAP supercell model in lateral projection for the $P6_3$ phase (OH groups are parallel oriented (ordered) in OH channel along c axis and therefore can create a summarily polar state); d) HAP supercell model in lateral projection for the $P6_3/m$ phase (OH groups are anti-parallel oriented (disordered) in OH channel along c axis and therefore can create a summarily non-polar state).

3.2. Supercell model

The main feature of our more detailed study is the introduction of the super-cells model made up of $2 \times 2 \times 2 = 8$ polar HAP unit cells (with space group $P6_3$) for hexagonal HAP ordered phase (both for initial pristine stoichiometric and defective HAP with oxygen vacancies and with full OH group vacancy) [7, 8].

It should be note that this phase demonstrates polar ferroelectric state with the total polarization along c-axis, due to OH groups oriented parallel and along the OH-channels. While the disordered phase of hexagonal HAP (with space group $P6_3/m$) forms non-polar paraelectric state, due to compensation of an opposite anti-parallel orientation of OH groups, which are along these OH channels [36, 37].

3.3. Main structural and mechanical properties of HAP

We start by the analysing on the structural and mechanical properties of initial stoichiometric HAP and HAP with following defects: OH-vacancy and various O-vacancy types. Table 2.1 and 2.2 compare the calculated structural data (unit cell lattice parameters and volume) and bulk modulus (for some cases) with the respective experimental data. Table 2.1 presents the data of pristine stoichiometric HAP (computed by various methods and from different experimental data) and data of HAP with one full OH-vacancy. Table 2.2 consists of calculated data for various types of O-vacancies.

Table 2.1. Data of HAP lattice parameters and bulk modulus for pristine HAP and HAP with OH-vacancy.

Property	Experim. [11]	Experim. [55]	Experim. [56] ([57])	AIMPRO (LDA) [5, 6]	PBE VASP (GGA)	PBE (GGA)/supercell ^{***} [7, 8]	B3LYP/supercell ^{***} [7, 8]	HSE06 [7]	PBE0 [7]
Initial stoichiometric HAP (hexagonal $P6_3$)									
a, Å	9.417	9.4236	9.4205 (9.4248)	9.4732	9.3628	9.537	9.5770	9.481	9.477
c, Å	6.875	6.8802	6.8828 (6.8860)	6.9986	6.8454	6.909	6.8767	6.859	6.851
V, Å ³	527.99	529.13	528.99 (529.71)	543.92	519.69	546.07	546.22	533.95	532.88
B, GPa	89 ± 1 ^{*)}			82 ± 2	-	82 ± 3	86 ± 2	83 ± 3	82.8±0.3
HAP with OH-vacancy									
a, Å		9.4155 ^{**)}		9.4883	9.4210	9.537	9.5770	-	-
c, Å		6.8835 ^{**)}		7.0018	6.880	6.909	6.8767	-	-
V, Å ³		528.48 ^{**)}		545.905	528.83	546.07	546.22	-	-
B, GPa				78 ± 2					

^{*)} References [58, 59]

^{**)} Data from Bulina N.V. experiment (cooling from 1100 °C in He atmosphere: *see comment in the text*)

^{***)} For supercell simulations the cell parameters were not varied and were fixed to those obtained for perfect stoichiometric HAP. The positions of the atoms were relaxed on PBE(GGA) level. After that the single point hybrid DFT (B3LYP, HSE) calculation were performed to obtain the total energy.

Tables 2.1 and 2.2 include the results obtained with LDA method (in earlier calculations using AIMPRO [5, 6]) and with GGA approximation on the various DFT exchange-correlation functionals: PBE, HSE06, B3LYP, and PBE0 (using VASP calculations [7, 8]).

The calculated lattice parameters for initial pristine stoichiometric HAP lattice within the PBE level approach are in good agreement with the previous known PBE results (see [48-51] and references therein).

They show the usual $\sim 1\%$ overestimation on relation to the experimental data. This is known to be mostly due to an artificial over-delocalization of the electronic density when the GGA approach is employed. It is shown that the calculations using B3LYP results in improvement of c lattice parameter, but parameter a is still overestimated by $\sim 1\%$ [7]. This confirms previous reports that B3LYP generally overestimates the experimental lattice parameters as well [35]. On the other hand, our result differs from the previous B3LYP calculations of HAP, where a was underestimated by $\sim 1\%$ [35]. More discussion about the reasons of these discrepancy was given in [7].

Table 2.1 also indicates that the lattice parameters calculated within hybrid DFT are generally closer to the experiments than those obtained using the semi-local functional. The best results are obtained for PBE0 with a deviation of $< 0.6\%$ on relation to the experiments [7].

It should be noted, that the results obtained earlier in the LDA approximation are the closest to the experimental data on the lattice parameter a (even slightly better than in the case of a PBE0 with deviation less than 0.6%), while the value of the parameter c turned out to be more overestimated here (the deviation is almost 1.8%).

The bulk modulus (B) were obtained here as usually by fitting the Birch-Murnaghan equation of state [5, 61]. The calculated bulk modulus show reasonable agreement with the experiments (see data in 2nd column of Table 2.1, Refs. [58, 59]). The errors (shown in the table) were obtained from the standard fitting procedure. B3LYP calculations show deviation from the measurements by about 3% only, while other methods underestimate the experimental value of B by 7% - 8% . This level of accuracy is in line with typical discrepancies found for many other insulating materials [60]. It is interesting again to note, that LDA approximation shows here the same value of B as on PBE (GGA) level.

Experimental data on stoichiometric natural and synthetic samples should be used and analyzed rather carefully, since there may be impurity ions (carbonate, nitrate) that affect the lattice parameters. Therefore, the composition of stoichiometric hydroxyapatite should be confirmed by other analytical methods (for example, IR data), in addition to diffraction methods, which is usually used to determine the lattice parameters. Also, synthetic stoichiometric HAP should be well annealed at high temperatures in moisture air atmosphere. Table 2.1 provides experimental data that mostly meet these requirements [11, 55-59]. Below in the section 3.3.1 we will discuss this data in comparison with our calculations.

In Table 2.2, the results of calculations are presented in more detail for the presence of various types of oxygen vacancies in HAP. Here, a complete optimization of the HAP structure (cell parameters and ion relaxation) was carried out only by methods LDA (AIMPRO) and PBE (GGA) in the one unit cell model, since such an optimization has not yet been performed for the supercell.

Table 2.2. The calculated HAP lattice parameters with various type of the O-vacancy.

Property	Type of O-vacancy	AIMPRO (LDA) [5, 6]	PBE - VASP (GGA)
HAP with O-vacancy from OH (one u.c. HAP P6 ₃ model)			
a, Å	-	9.4539	9.3437
c, Å	-	7.0028	6.8463
V, Å ³	-	542.03	517.64
HAP with O-vacancy from PO ₄ (one u.c. model HAP P6 ₃ model)			
	O in various positions PO ₄ *)		
a, Å,	V_O1 (O6)	9.4599	9.3570
	V_O2 (O15)	9.4630	9.3520
	V_O3 (O30,O35)	9.4581	9.3544
	V_O4 (O24)	9.47295	
aver. a, Å		9.4635±0.005	9.3545±0.005
c, Å	V_O1 (O6)	6.9884	6.8139
	V_O2 (O15)	6.9890	6.8242
	V_O3 (O30,O35)	6.9893	6.8402
	V_O4 (O24)	6.97822	
aver. c, Å		6.9890±0.005	6.8261±0.005
V, Å ³	V_O1 (O6)	541.60	517.86
	V_O2 (O15)	542.01	518.33
	V_O3 (O30,O35)	541.47	517.45
	V_O4 (O24)	542.31	
aver. V, Å ³		541.85±0.3	517.88±0.1

*) O-vacancy from PO₄: Atom O — is in various positions of PO₄ (and from different PO₄ groups, in according with Fig. 2)

3.3.1. Defects (OH and O vacancies) influence on structural and mechanical properties.

Let us now consider the effect of defects (oxygen vacancies and OH group vacancies) in the HAP structure on the change in its structural and mechanical properties.

1) *Influence of OH-vacancy.* The data calculated by LDA (AIMPRO) show that the relative changes in the lattice parameters of HAP after the appearance of an OH vacancy (in one HAP unit cell) both increase by small values: $\delta a \sim 0.15\%$ and $\delta c \sim 0.05\%$.

At the same time, calculations using PBE (GGA) show that the value of the lattice parameter also relatively increases by $\delta a \sim 0.6\%$, and the parameter c increases by $\delta c \sim 0.5\%$.

For comparison with experimental data, we use here the results of experiments on heating and cooling HAP samples, which should lead to the escape of some OH groups from the OH channel and the formation of OH vacancies in HAP.

In situ diffractometric studies carried out in the group of Dr. N.V. Bulina showed that the cooling of apatite sample in helium atmosphere, heated to a temperature of 1100 ° C, leads to a decrease in parameter **a** and an increase in parameter **c**. The Table 2.1 shows the obtained experimental data. In such conditions, OH vacancies formed at high temperatures remain up to room temperature and the cooled sample is oxyhydroxyapatite (OHAP) containing vacancies of OH groups.

The changes obtained in the lattice parameters in the presence of OH vacancies in comparison with those known for pristine stoichiometric HAP turned out to be as follows: the relative changes were the largest for the parameter **a**, the decrease was up to $\delta a \sim -0.016\%$, and for the parameter **c**, an increase by about $\delta c \sim 0.5\%$.

If we compare with the initial experimental data [11], then the changes are similar. Thus, these obtained data are very close to the calculated data in the main trend of changes in the lattice parameters during the formation of an OH vacancy: a slight decrease in the lattice parameter **a** (and in the calculations there is an increase) and a noticeable increase in **c** value for all cases due to the formation of an OH vacancy in the HAP sample.

As for the volumes of the cells, with both methods of calculation, a relative increase in volume was obtained (Table 2.1). For Bulina's experimental data, the volume slightly decreased. But, if we compare it with the initial volume of [11], then it also increased.

It is important that the calculation results show a similar character of the cell parameters measurement. This means that the chosen model and calculation method are correct and allows us to investigate in more detail the physical reasons for this phenomenon [19].

In this case with OH vacancy in HAP sample, the calculated values of the volume modulus B (performed after the LDA method optimised calculation) showed its decrease, that is, this can lead to a decrease in the mechanical strength of HAP samples.

It seems that the presence of any vacancy, including the OH group, should increase the lattice parameters, which is what we get. However, it is likely that in the experiment, out of 2 vacancies of OH groups, one disappears, and it is occupied by the O^{2-} ion (that is, the hydrogen atom H also disappears here and one oxygen ion remains - this is already forming oxyapatite (OAP)). This is possible and leads to the following observed change in the lattice parameters: HAP ($a = 9.4236 \text{ \AA}$ $c = 6.8802 \text{ \AA}$) goes into OHAP ($a = 9.4155 \text{ \AA}$ $c = 6.8835 \text{ \AA}$). Moreover, some recent experimental data show that if OAP is formed here, then the lattice parameters should be as follows: OAP ($a = 9.4057 \text{ \AA}$ $c = 6.8938 \text{ \AA}$).

Unfortunately, we have not yet performed calculations of the exact OAP models. It would be very interesting and useful, and we will definitely do it in the near future.

2) *Influence of O-vacancy from OH group.* In this case (presented in Table 2.2), the calculated values of the unit cell parameters give some relative decrease in the parameter **a** (both for the LDA (AIMPRO) and GGA (PBE/VASP) methods), while the **c** parameter also decreases when calculated by the LDA method, but slightly increases when calculated by the GGA method. Experimental data we have not for this case.

3) *Influence of O-vacancy from PO₄ group.* In this case (presented in Table 2.2), the calculated values of the unit cell parameters were considered for different positions of oxygen atoms that create O-vacancies (for example, see Fig 2). For the model of one unit cell, these positions were selected and calculated by the LDA method in the works [5, 6] and here in the Table 2.2 these data are given. Similarly the calculation using GGA (PBE) method was performed.

These O-vacancies were computationally investigated in more detail by the GGA PBE and B3LYP methods in the work [8] in the HAP 2x2x2 supercell model. We will analyse this data separately below in the Section 3.4.3, devoted to supercell model.

For the cases of O-vacancies from the PO₄ group indicated in this Table 2.2, the results obtained by both LDA and GGA (PBE) methods show that both the unit cell parameters **a** and **c** decrease, despite some of their differences for different positions of the selected oxygen atoms, which creating these O-vacancies. Experimental data for structural analysis in these case we haven't now. But these cases demonstrate very interesting and important results of their electronic and optical properties, that will be analysed below.

3.4. Electronic and optical properties

3.4.1. Electronic properties of pure HAP by various methods

As a result of LDA calculations (using AIMPRO software [38]) and GGA calculations (using VASP with functional PBE [39, 48]) the distributions of the density of states of electrons by energy (DOS) corresponding to the filling of energy levels in the scheme with electrons and the energies of HAP according to the band theory were obtained [5-9, 36, 37]. This makes it possible to determine the main parameters - the position of the top of the valence band E_v , the bottom of the conduction band E_c and the value of the forbidden band gap $E_g = E_c - E_v$, as well as the position of additional energy levels E_i induced by defects in the internal range of E_g .

The question now is how defects change this entire band energy structure of the states of electrons. And how close it will be to the experimental values, when creating certain defects in HAP structure. For calculations at the first stage [5, 6], the defects simulated were created by vacancies and interstices into one hexagonal unit cell of HAP consisting of 44 atoms (Fig. 1). In Figure 2 schematically shows examples of simulated HAP structures with defects such as oxygen vacancies from the OH and PO₄ groups, as well as a vacancy of the entire OH group. For more details and precise calculations with various DFT hybrid functional we use supercell model consisting of 352 atoms (8 unit cells) (Fig.3) [7, 8].

First we consider HAP without any defect in initial pristine stoichiometric hexagonal phase P6₃ symmetry. Figure 4 (Left figures: a, b, c) shows examples of DOS for perfect stoichiometric defect-free HAP (taking into account both deeper energy levels in the valence band and in the vicinity of the forbidden band) obtained in LDA calculations [5, 6]. Similar GGA calculations were carried out using VASP software [39]. Figure 4c show results of DOS from GGA (with PBE functional). Note that the calculations using the LDA and GGA (PBE) approximations generally do not fundamentally differ here, the difference is only in the energies - GGA (PBE) gives a larger value of the band gap $E_g \sim 5.26 \pm 0.05$ eV (for perfect stoichiometric HAP)

compared to calculations by the LDA method, which give $E_g \sim 4.6 \pm 0.05$ eV. These data are close to results of other authors [30-35].

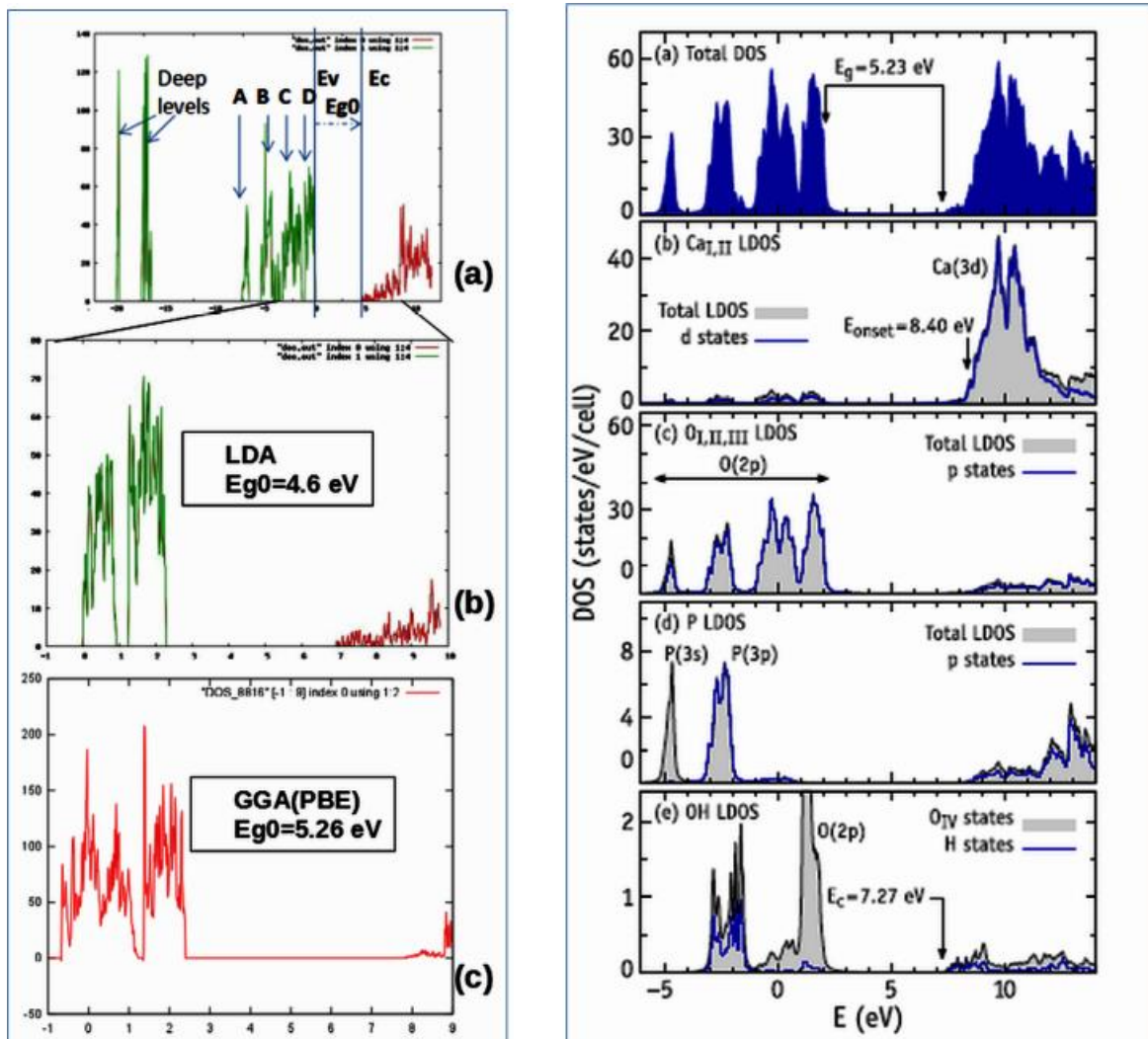


Figure 4. Left figures: Density of electronic states (DOS) for HAP unit cell: (a) Initial perfect stoichiometric HAP with 44 atoms in hexagonal $P6_3$ unit cell lattice, including deep levels and A,B,C,D peaks in valence band computed in LDA by AIMPRO; (b) the same with main energies around E_g ; (c) the same computed in GGA (PBE) by VASP; (Data presented here obtained after calculations using AIMPRO (LDA) [38] and using VASP (PBE-GGA) [39]);

Right figures: Total density of states of bulk HAP (a) and local densities of states projected on calcium (b), oxygen in PO_4 units (c), phosphorous (d), and oxygen and hydrogen in OH units (e). In (b)–(d), the contribution to the LDOS with the dominant angular momentum is represented as a thick line. The results were obtained using the PBE exchange-correlation functional. ((Reproduced with permission from [7]; AIP Publishing, 2018).

Figure 4 (Right figures: (a) - (e)) shows the total DOS of a HAP unit cell obtained within PBE more precise and detailed calculations [7, 8], including also local density of states (LDOS) [7]. The shadow plots on subsequent figures [right Figs. 4(b) – 4(e)] depict the LDOS projected on several atomic species.

Note here that the calculations using both GGA (PBE) approach do not fundamentally differ here, the difference is only small in the energies; first GGA (PBE) gives a value of the band gap $E_g \sim 5.26 \pm 0.05$ eV, while second PBE gives a value $E_g = 5.23$ eV, that is in the accuracy frame and in line with calculations of other authors by this method [9, 30-37].

Along with the LDOS of right Figs. 4(b)–4(d), we plot a thick line representing the dominant angular-momentum component for the corresponding species. In right Fig. 4(e), we distinguish states projected on OIV and H atoms that form OH molecules. At first glance, Figs. 4(b) and 4(c) suggest that the upper end of the valence band is mostly made of O(2p) states, while the conduction band bottom is mostly made of Ca(3d) states. From Figs. 4(c) and 4(d), we find phosphorous 3s-3p states mixing with oxygen 2s-2p states between 5 and 2 eV and they are far below from the band gap region. All these results are in line with reports of other authors [9, 18, 19, 30-37].

3.4.2. Electronic band structure of perfect stoichiometric HAP

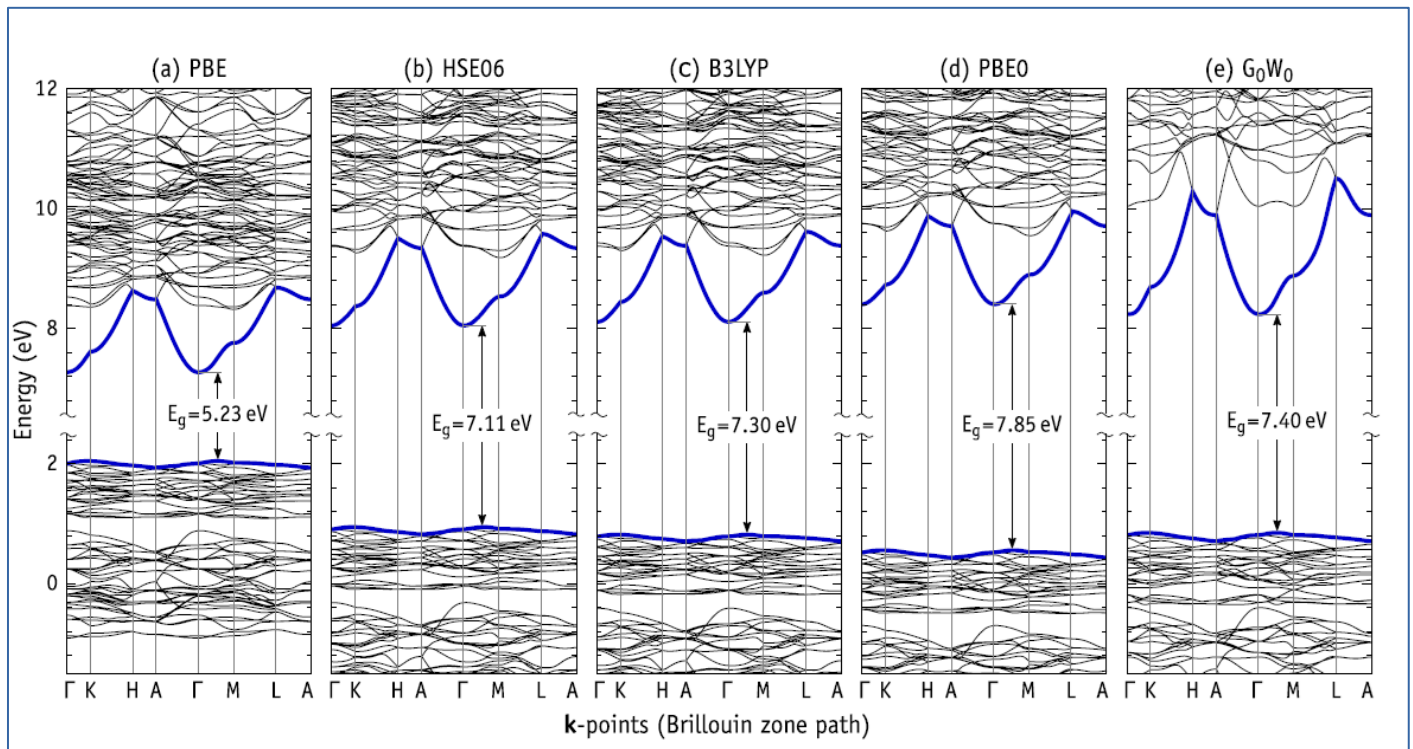


Figure 5. Electronic band structure of bulk perfect stoichiometric hydroxyapatite along a path with breaks at k-points of high symmetry. The calculations were carried out using DFT using functionals: (a) PBE - in the generalized gradient approximation (GGA), and hybrid functionals: (b) HSE06, (c) B3LYP and (d) PBE0, as well as (e) using the method multi-particle perturbations G0W0 using the wave functions of the PBE functional. The maximum valence and minimum conduction bands are shown in bold lines. Indirect transitions determining the band gap E_g are also shown for each case. (Reproduced with permission from [7]; AIP Publishing, 2018).

Further calculations of HAP perfect stoichiometric structure and properties were developed and performed in [7] using various DFT hybrid functionals. These results obtained demonstrate rise of E_g for perfect stoichiometric HAP with using of more developed functional and method. We discussed this point below.

Interesting that the energy scale of above DOS calculations is directly comparable to the band structure obtained in [7] calculations (see Fig. 5 (a) for PBE).

Figures 5(a)–5(d) compare the electronic band structure obtained using different exchange-correlation functionals (PBE, HSE06, B3LYP, and PBE0) with the analogous *G0W0* quasi-particle calculation shown in Fig. 5(e) [7]. The band energies along the several high-symmetry directions were obtained by interpolation of the first-principles data using Wannier90 [62].

The shape of the PBE band structure in Fig. 3(a) is indistinguishable from that reported by Slepko and Demkov [34] displaying a low-dispersive valence band top and a high dispersive conduction band bottom (thick bands). Dispersion of the conduction band minimum states is considerably more pronounced along directions parallel to the *c*-axis (Γ –*A*, *K*–*H* and *M*–*L*), indicating a stronger carrier delocalization and mobility along the main axis. This property could be explored for tuning HAP electrical conductivity through n-type doping or for photo-current measurements. On the other hand, p-type doping is not expected to be beneficial. The valence band top states show very little dispersion, and their heavy holes imply a relatively lower mobility.

Also in agreement with [34] we find HAP to be an indirect-gap material with $E_g = 5.23$ eV at the PBE level. The conduction band minimum is located at $\mathbf{k} = \Gamma$, while the valence band top energy was found somewhere along Γ –*K* or Γ –*M*. The valence band maximum along Γ –*M* is only 0.1 meV higher than the one along Γ –*K*. We note that this picture was the same regardless of the functional used, including when using the *G0W0* method.

The band structure obtained within the HSE06 level is shown in Fig. 5(b). The increase in the band gap width by more than 30% with respect to the PBE result is self-evident. Using HSE06, we obtain $E_g = 7.11$ eV. Often, the band energies are offset in order to lock the valence band top at the origin of the energy scale. We did not follow this procedure and that allowed us to disclose how the gap change depends on the shift of both valence band and conduction band states.

Figures 5(b)–5(d) show that admixing a fraction of Fock exchange with the semi-local exchange energy has a profound effect on both valence and conduction band states. Consequently, the use of hybrid functionals has implications not only to the accuracy of calculated defect-related or inter-band transitions (e.g., observed in luminescence or UV-VIS absorption) but also to transitions involving core or vacuum states (e.g., observed in electron photoemission or core electron energy loss spectroscopy) [7].

The gap of the B3LYP band structure depicted in Fig. 5(c) is 0.6 eV narrower than that reported by Corno *et al.* [35] using the same functional. Again, the difference is likely to be due to the unsuitability of the atomic-like basis employed in [35], which resulted in the under-screening of the band structure. The band gap width and the band gap edge energies obtained at the B3LYP-level are closer to the *G0W0* results than any other functional.

So, it should be noted and concluded here, that with the rise of each next developed type of DFT functional the total electronic band structure of pure HAP changes: the energies of the valence band top is down and the bottom of the conduction band is up. As a result, the band gap width $E_g = E_c - E_v$ increases (see Fig. 5 a - e).

This trend of the calculated band gaps agrees with that obtained by Garza and Scuseria [63] for an eclectic mix of semiconductors and insulators. Accordingly, HSE06 and B3LYP showed a closer correlation with the experiments (the former giving slightly smaller gaps overall), whereas inclusion of larger fractions of exact exchange, like in PBE0, led to an overestimation of E_g . This ordering also suggests that the gap width obtained within G0W0 ($E_g = 7.4$ eV) should be close to the real figure.

Another interesting point should be noted here, regarding the origin of the bottom of the conduction band, in particular, the highly dispersive bands shown in Fig. 5, the situation here is somewhat controversial. In [34], an analysis of the LDOS at the conduction bottom indicated that the lowest energy bands originated from Ca(4s) states.

Authors [7] argue that this view finds several difficulties. First, in [7] authors find the onset of the Ca-LDOS ($E_{\text{onset}} = 8.40$ eV) located ~ 1 eV above the conduction band minimum energy. Within that energy range, all that can be related to Ca are the flat Ca(3d) bands above 8.4 eV. Second, right Fig. 4(e) shows that states just above E_c have a considerable localization on OH molecules.

Interestingly, that in this case the highly dispersive bands that form the bottom of the conduction band of HAP are anti-bonding states from an infinite ...OH–OH... hydrogen bridge sequence (along OH-channel through all HAP crystal structure), much like a 1D-ice phase. This statement finds support in the band structure of hexagonal ice (see, e. g., Figs. 4 and 6 in [64, 65]). From comparison these band structure images with Fig. 5(a), it becomes immediately evident that the dispersion shape of the lowest conduction band of HAP is analogous to that of the hexagonal ice.

In this relation, it is interesting to note that nano-confined water [66] inside hydrophilic cavity (or inner channel) inside so-called peptide nanotube (such as, e.g., the diphenylalanine nanotube) has structure close to the one-line hexagonal ice structure [66, 67]. So, we should note here that it is some common property in tubular or columnar molecular-like periodical crystal structure, which could be observed in these related structures.

3.4.2. Electronic band structure of defective HAP (with OH- vacancy and O-vacancies)

In Figure 6 examples of DOS in the results of GGA (PBE) calculations are given for defects in HAP structure, such as, O vacancies from the OH group, O vacancies from the PO_4 group, and a full vacancy of the OH group, based on HAP unit cell model with 44 atoms (see also than data of calculated energies of the electronic band structure's basic states in Table 3).

These data are close to results of other authors [19, 30-34]. The results obtained also lead to a small shift in all level energies for defects in the calculations of the GGA (PBE) methods relative to LDA (Table 3). Both methods predict the changes in band gap E_g and of the electron work function $\Delta\phi$, that can experimentally measure [2, 4, 9, 53].

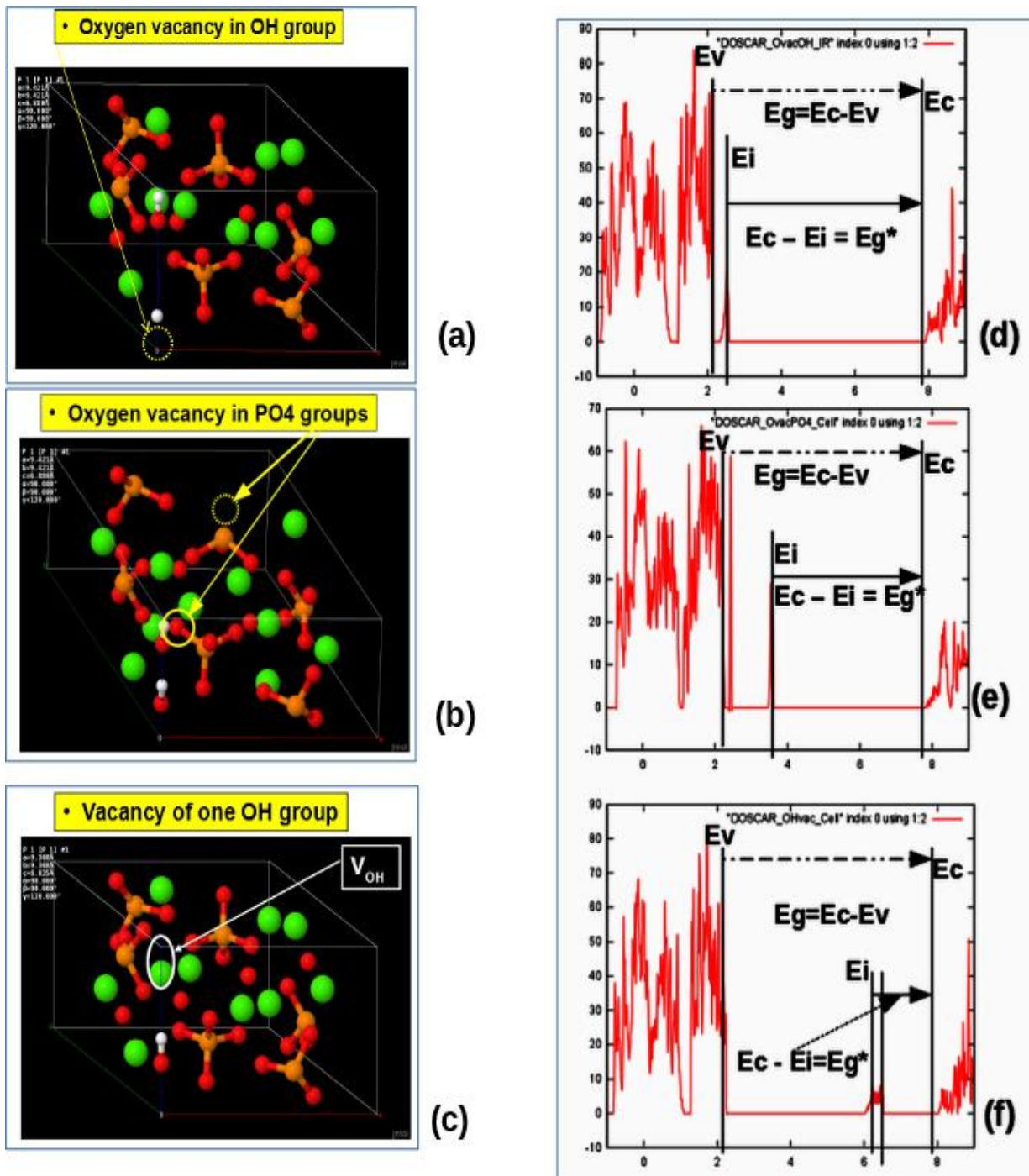


Figure 6. Density of electronic states (DOS) for HAP unit cell with defects: (a) HAP unit cell model with O vacancies from the OH group; (b) HAP unit cell model with O vacancies from the PO₄ groups (this may be with O atom from different positions); (c) full vacancy of the OH group from HAP unit cell model; (d) DOS for case of the O vacancy in OH group; (e) DOS for case of the O vacancy in PO₄ group; (f) DOS for case of the full OH vacancy. (Data presented here obtained by calculations firstly using AIMPRO (LDA) [5, 6, 38] and then VASP (GGA) [39], similar to our works [4-8]). (Reproduced with permission from [5]; IOP Publishing, 2015).

Table 3. Calculated data for HAP defects by two various approaches (aver. error = ± 0.05 , ± 0.1 eV) [4-6].

Defect type	LDA				GGA (PBE)			
	$E_g = E_c - E_v$, eV	$\Delta E_g = E_g^* - E_g \sim \Delta\phi$, eV	$E_i - E_v^*$, eV	$E_g^* = E_c^* - E_i$, eV	$E_g = E_c - E_v$, eV	$\Delta E_g = E_g^* - E_g \sim \Delta\phi$, eV	$E_i - E_v^*$, eV	$E_g^* = E_c^* - E_i$, eV
HAP in $P6_3/m$	4.6	-	-	-	5.26	-	-	-
$O_{(OH)}$ vac	5.15	+0.55	0.1 (1 occ.)	5.05	5.72	+0.46	0.27	5.45
OH vac	5.49	+0.89	3.11-3.82 peaks: 3.40 3.53 3.66 ($\frac{1}{2}$ occ.)	2.38-1.67 peaks: 2.09 1.96 1.83	5.75	+0.49	3.66-4.28 peaks: 3.96 4.11 4.17	1.97-1.35 peaks: 1.78 1.63 1.57
Ovac(PO_4) ^{*)}								
V_O1 (O6)	4.734		1.346	3.388	5.416		1.045	4.115
V_O2 (O15)	4.768		1.300	3.468	5.246		1.212	4.034
V_O3 (O30,O35)	4.735		1.347	3.388	5.326		1.142	4.184
V_O4 (O24)	4.5614		0.9557	3.6057				
aver. $O_{(PO_4)}$ -vac	4.70 ± 0.2	+0.15	1.14 ± 0.3	3.52 ± 0.3	5.34 ± 0.2	+0.08	1.13 ± 0.2	4.11 ± 0.2

^{*)} Ovac PO_4 – Atom O in various positions of PO_4 (and may be in the different PO_4 group, in according with Fig. 2).

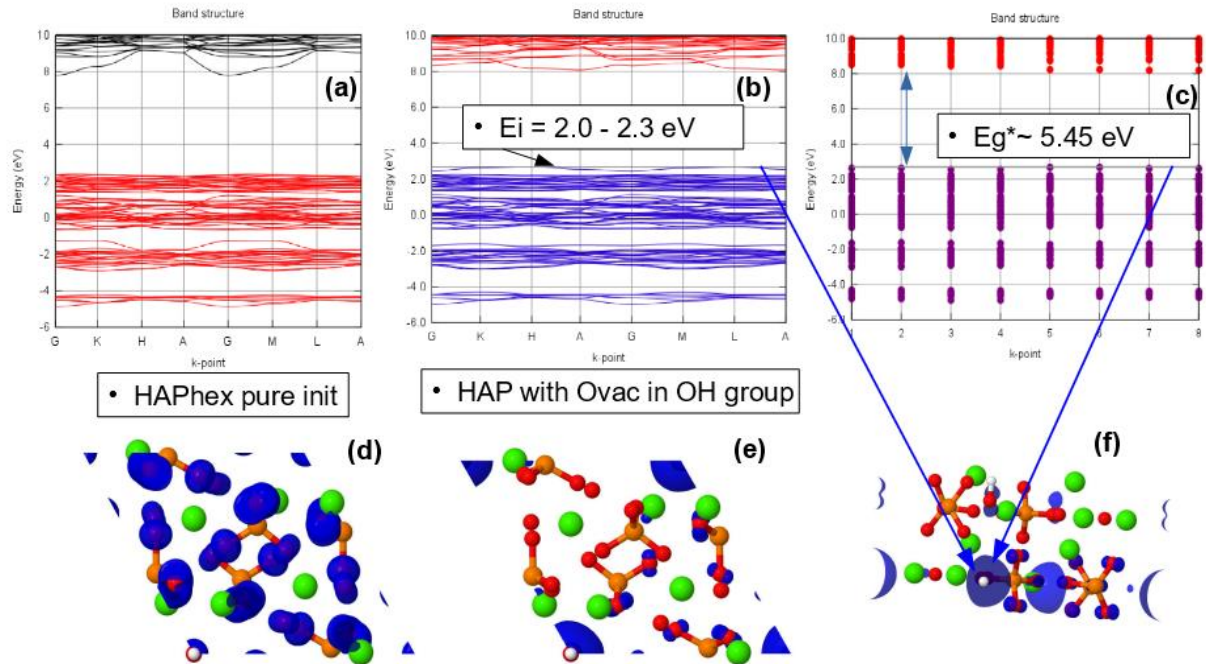


Figure 7. Band structure and partial charge density distribution for O-vacancy from OH group in hexagonal HAP (for one unit cell model): a) and d) band structure and partial charge density (top view) of initial pure HAP; b) and e) band structure and partial charge density (top view) for HAP with O-vacancy in OH group (local energy level $E_i \sim 2.0 - 2.3$ eV is close to the top of valence band $\Delta E = E_i - E_v \sim 0.1 - 0.3$ eV); c) band structure distribution along k-points with local energy level led to optical $E_g^* \sim 5.45$ eV; f) partial charge density for electrons with their eigenvalues around the energy level E_i of the O-vacancy in HAP (side view of the unit cell).

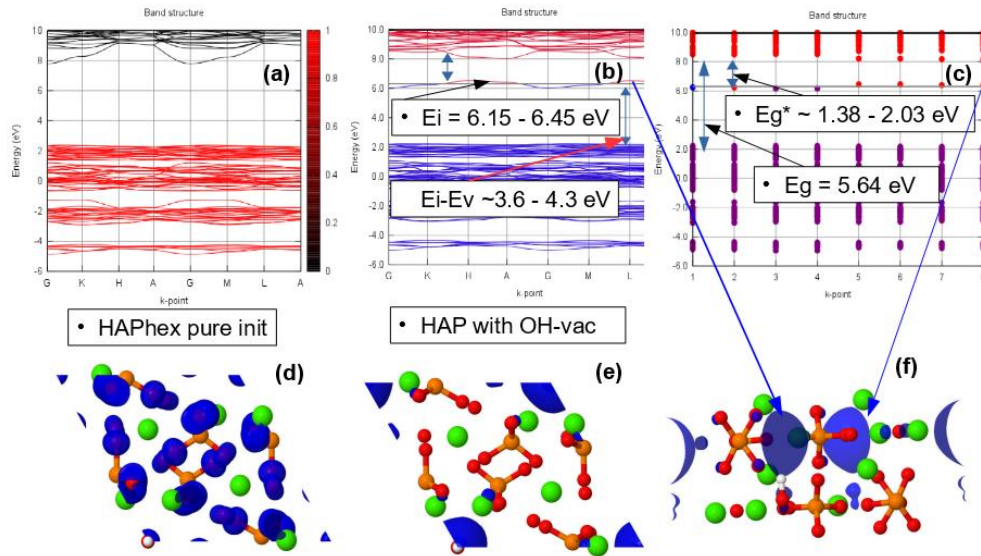


Figure 8. Band structure and partial charge density distribution for OH-vacancy in hexagonal HAP (for one unit cell model): a) and d) band structure and partial charge density (top view) of initial pure HAP; b) and e) band structure and partial charge density (top view) for HAP with OH-vacancy (local energy level $E_i \sim 6.15-6.45$ eV is the middle of the forbidden band and with $\Delta E = E_i - E_v \sim 3.6-4.3$ eV); c) band structure distribution along k-points with local energy level led to optical $E_g^* \sim 1.38-2.03$ eV in comparison with total $E_g \sim 5.64$ eV; f) partial charge density for electrons with their eigenvalues around the energy level E_i of the OH-vacancy in HAP (side view of the unit cell).

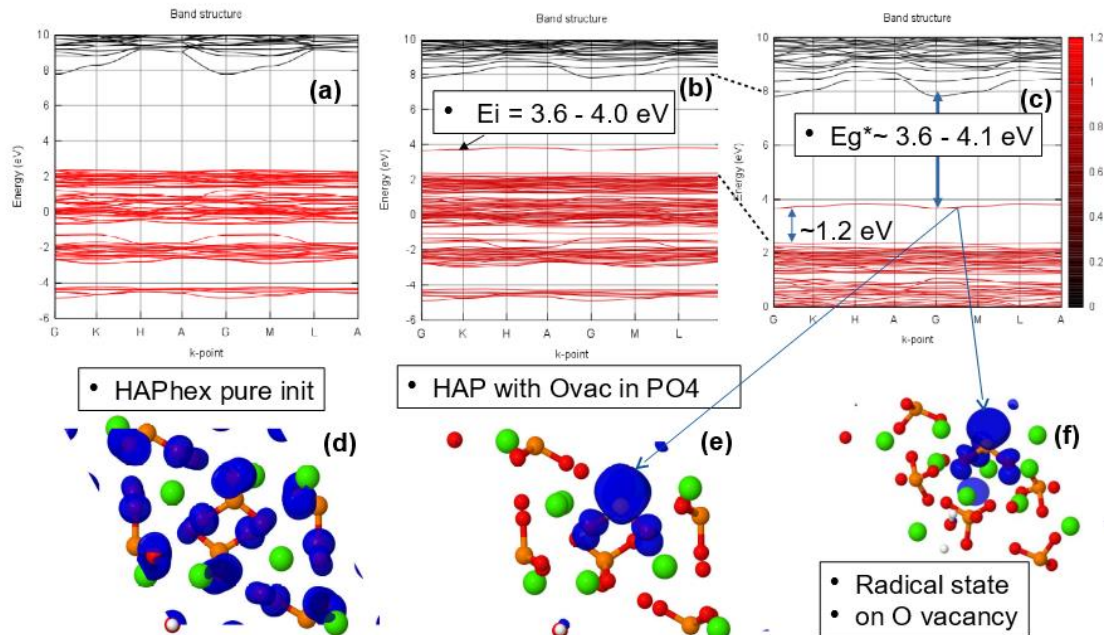


Figure 9. Band structure and partial charge density distribution for O-vacancy from PO_4 group in hexagonal HAP (for one unit cell model): a) and d) band structure and partial charge density (top view) of initial pure HAP; b) and e) band structure and partial charge density (top view) for HAP with O-vacancy from PO_4 (local energy level $E_i \sim 3.6-4.0$ eV is the middle of the E_g band and with $\Delta E = E_i - E_v \sim 1.1-1.3$ eV); c) band structure distribution along k-points with local energy level led to optical $E_g^* \sim 3.6-4.1$ eV in comparison with total $E_g \sim 5.34$ eV; f) partial charge density for electrons with their eigenvalues around the energy level E_i of the O-vacancy of PO_4 group in HAP (side view of the unit cell).

Figures 7, 8, 9 below show examples of the band structure and the partial charge density for electrons with their eigenvalues in the range specified around the energy level E_i of corresponding defect structure for several main defects in HAP, obtained after optimized VASP calculations in one unit cell model.

These results clearly show that it is precisely the oxygen vacancies of the PO_4 group that provide the optical band with the energy $E_g^* \approx 3.6 - 4.2$ eV, which is usually observed in many experimentally prepared samples [4-6, 19-22, 36, 37, 53]. All these samples in the manufacturing process undergo heat treatment at temperatures $T = 1000 - 1200$ °C (that is, $= 700 - 1000$ K) and this leads to the formation of not only OH vacancies, but also a multitude of O vacancies [19-22] (especially from the PO_4 group). This leads to the observed optical absorption and optical band width $E_g^* \approx 3.6 - 4.2$ eV, while the band gap of the defect-free perfect stoichiometric HAP turns out to be wider and equal to $E_g \approx 5.4$ eV and more (in the GGA PBE calculations).

Further development of the calculations was the transition to calculations from one unit cell to a super-cell model consisting from of **2x2x2=8 unit cells**, (space group $P6_3$, comprising a total of 352 atoms), as well as the application of the hybrid functional PBE (for 1st step optimization) in combination with B3LYP (for 2nd step calculation) using DFT method [7, 8]. This made a possibility to classify different types of oxygen vacancies of the PO_4 group more correctly and accurately, that increases the calculation accuracy and to *highlight not only neutral defects, but new more complex types of defects - extended charged complex oxygen vacancies*.

3.4.3. Oxygen originated complex HAP defects in supercell model

Performing these series of calculations, it was found that different types of defects arise, if the symmetry of the atomic group associated with different spatial arrangement of various atoms in the PO_4 group. Besides, usual oxygen vacancy V_O , here arises complex extended defects, that depend on their charge state $Q = 0, +1, +2$. (Figure 10) [8, 36, 37]. The O vacancy of OH group influences the formation of new complex defects because of charge Q variation.

Crystalline HAP has oxygen atoms on four symmetry in equivalent sites, which are referred to as oxygen types I-IV. Types I, II, and III are in the phosphate units, while type IV oxygen atoms are located in the OH^- anions. These are denoted as O(I), ..., O(IV) and are shown in the upper half of Figure 10, where portions of bulk HAP are depicted. We note that PO_4 groups have two nearly symmetric O(III) atoms which are superimposed in the upper view of bulk HAP in Figure 10.

Among the many vacancy structures investigated, those shown in Figure 10 a-e are the most relevant as they showed lower energy. Metastable structures with more than 2 eV above the ground state (for each particular charge state) will not be discussed. Figure 10a describes the formation of a pyramidal PO_3 structure, where removal of the O(I) atom in "Bulk HAP" highlighted using a bright red color, leads to $V_{O(I)}$ as shown in the lower part of the figure, where a "Defective HAP" region is shown.

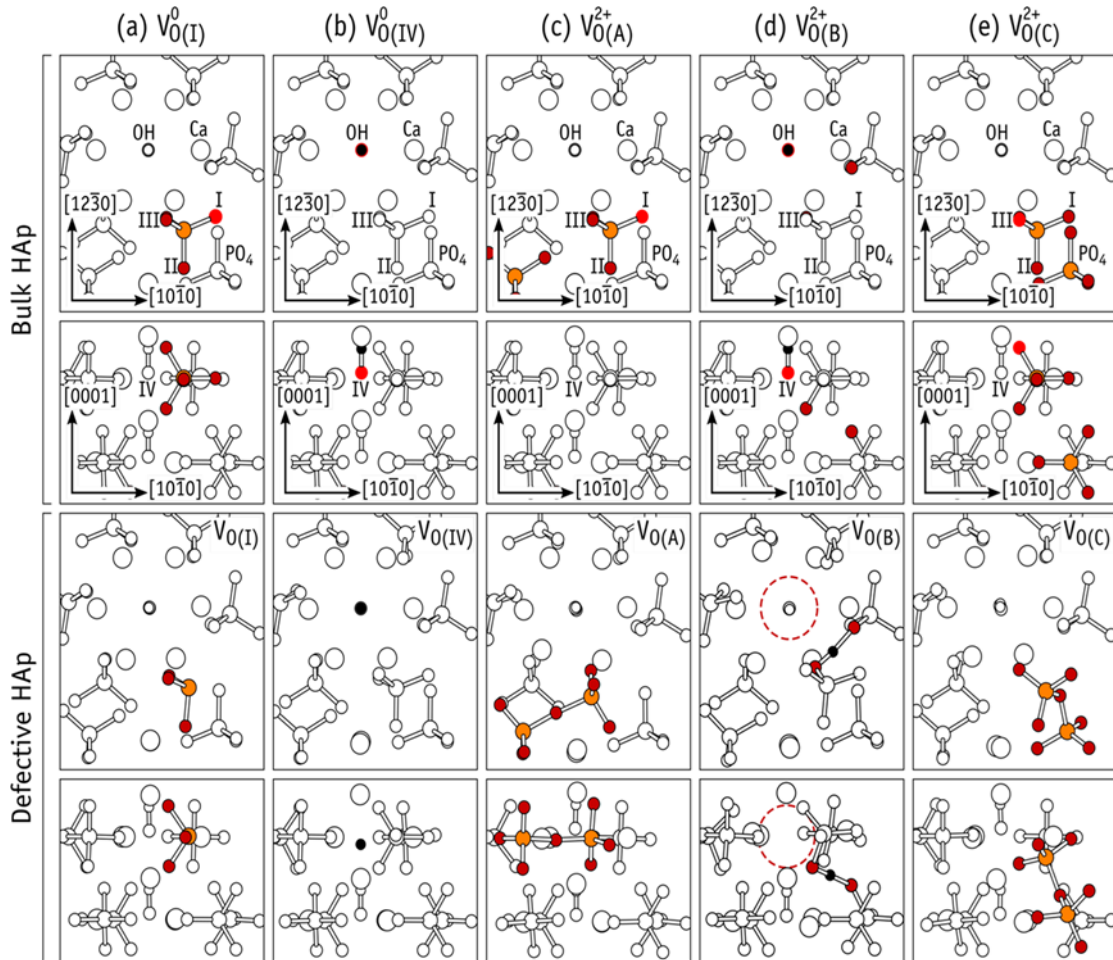


Figure 10. Diagrams showing “Bulk” (upper half) and “Defective” (lower half) HAP. For each row pair, upper and lower rows display the same structures viewed along the [0001] and [12 $\bar{3}$ 0] directions of the hexagonal lattice, respectively. Formation of structures I, IV, A, B, and C of V_O defects is explained in columns (a–e), respectively. Only atoms belonging to the core of the defect are colored (P, O, and H atoms are shown in orange, red, and black, respectively). Vacancies were created by removing the bright red O atom shown in the “Bulk” figures. Upon atomic relaxation, the resulting structures are those in the corresponding “Defective” figures. Reprinted with permission from [8]. (Reproduced from [8]. Copyright (2019) American Chemical Society).

Analogous structures for $V_{O(II)}$ and $V_{O(III)}$ were obtained as well. In the neutral charge state, the resulting $[\text{PO}_3^{3-}]_{\text{PO}_4^0}$ structures display a fully occupied sp^3 orbital on the P atom, resembling the phosphine molecule. This is shown in Figure 11a, where an isosurface of the electron density corresponding to the highest occupied state is represented in blue for the specific case of $V_{O(III)}^0$.

Figure 11b shows the case of a missing O(IV) atom, leaving an isolated H atom in the OH channel. This defect can be rationalized as the removal of neutral O from OH^- , leaving a hydride anion, and maintaining charge neutrality of the whole system. In the neutral charge state, we have a $[\text{H}^-]_{\text{OH}^0}$ structure, where after structural relaxation, the hydride species becomes located close to the site of the missing O(IV) atom (compare lower diagrams of bulk and defective HAP in Figure 10b).

The density corresponding to the highest occupied state of $V_{O(IV)}^0$ is represented in Figure 11b, which clearly shows the formation of a hydride anion in the OH channel. Figure 11e shows the OH-vacancy defect [7]. In $V_{O(I)}-V_{O(IV)}$ defects, all atoms (but the missing oxygen) remain essentially close to their original crystalline coordinates, hence the use of subscripted O(I)–O(IV) labels to identify their structure. However, additional structures, hereafter referred to as **extended structures**, were also found for the oxygen vacancy in HAP [8]. One type of such extended structures can be described as a pair of neighboring oxygen vacancies connected by an O-interstitial, $2V_O + O$. Another 2-nd type is best described as a complex made of an OH-vacancy next to an H-interstitial, $V_{OH} + H$. Two defects of type $2V_O + O$ are singled out and labeled $V_{O(A)}$ and $V_{O(C)}$. They are shown in Figure 10c and 10e, respectively. One $V_{OH} + H$ defect is shown in Figure 10d and is referred to as $V_{O(B)}$.

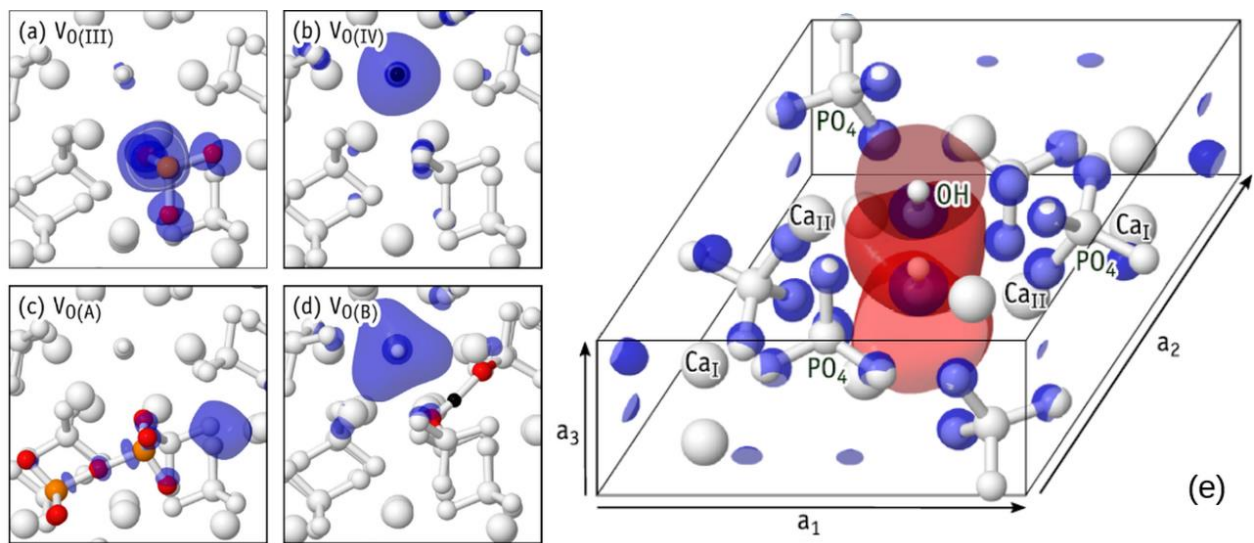


Figure 11. Electron density isosurfaces from the highest occupied Kohn–Sham level of neutral V_O defects in HAP. The density of $V_{O(III)}$ in (a) is representative of $V_{O(I)}$ and $V_{O(II)}$ as well. The density of $V_{O(IV)}$ in (b) shows the case of a missing O(IV) atom, leaving an isolated H atom in the OH channel. The density of extended charged defects $V_{O(A)}$ and $V_{O(B)}$ are shown in (c), (d) (description is in text). Isosurfaces are drawn at constant electron density $n = 0.001 \text{ \AA}^{-3}$. Reprinted with permission from [8]. Copyright (2019) American Chemical Society. (e) Lowest unoccupied Kohn-Sham state (bottom of the conduction band) of a HAP at $k = G$. Blue and red isosurfaces represent $y(r) = +0.02$ and $y(r) = -0.02$ phases of the wave function, respectively. All atoms are shown in white. Reprinted with permission from [7]. (CCC (2018) AIP Publishing).

A dashed circle is used in the figure to highlight the missing OH unit. The highest occupied state of the extended structures is shown in Figure 11c and 11d. They either overlap the void regions of the HAP crystal or the vacant volume of the OH-channel, thus suggesting that they are donors with antibonding character or strong resonance with conduction band states [7].

For relaxations in charge state +2 that started from structures I and III, the final structures were, respectively, A and C. Here, the P atom of the PO_3 unit in $V_{O(I)}$ (or $V_{O(III)}$) moved across the plane defined by the three O atoms to connect to the O atom from the nearest PO_4 moiety. Such a severe relaxation can be explained by electron transfer from a neighboring PO_4^{3-} anion to the empty $P(sp^3)$ orbital of $[PO_3^-]_{PO_4}^{2+}$ in $V_{O(I)}^{2+}$ or $V_{O(III)}^{2+}$ (see Figure 11a) and the subsequent formation a new P–O bond. The result is an extended $[PO_3^{2-}-O-PO_3^{2-}]_{2(PO_4)}^{2+}$ structure shown in Figure 10c and 10e.

When initiating the relaxation in charge state +2 from structures II and IV, the resulting configuration was in both cases $V_{O(B)}^{2+}$. In this charge state, the defect comprises an interstitial H^+ next to a positively charged OH vacancy, that is, $[PO_4^{3-}-H^+-PO_4^{3-}]_{2PO_4^+} + V_{OH}^+$. The proton is located on a high electron density site between two oxygen anions. The net positive charge of the OH vacancy follows from depletion of two electrons from the channel-state represented by the isosurface of Figure 11d. When starting from structure II, Coulomb attraction and subsequent reaction between neighboring OH^- and $[PO_3^-]_{PO_4^{2+}}$ leads to the formation of the $V_{O(B)}^{2+}$ extended structure. Alternatively, when starting from structure IV, a proton in the initial $[H^+]_{OH^{2+}}$ configuration is strongly attracted by O-anions in neighboring PO_4^{3-} moieties, also ending up in $V_{O(B)}^{2+}$ as depicted in Figure 10d.

3.4.4. Kohn–Sham energy levels of neutral V_o defects

Inspection of the Kohn–Sham eigenvalues at $\mathbf{k} = \Gamma$ confirmed that neutral vacancies V_o defects are all donors [8, 37]. The calculations performed in these cases, taking into account the even more accurate B3LYP calculation scheme, showed similar shifts in the energy levels created by defects such as oxygen vacancies of the PO_4 group, and their main contribution, which determines the change in optical properties and the change in the work function, remains at a level of ~ 1 eV or less (Table 4), despite the differences in the calculations of the band gap E_g for initially perfect stoichiometric defect-free HAP.

Table 4. Data for O vacancy from OH and PO_4 in different position and symmetry (errors ± 0.05 eV).

Defect type	PBE				B3LYP			
	$E_g = E_c - E_v$, eV	$\Delta E_g = E_g^* - E_g \sim \Delta\phi$, eV	$E_i - E_v^*$, eV	$E_c^* - E_i = E_i^0$, eV	$E_g = E_c - E_v$, eV	$\Delta E_g = E_g^* - E_g \sim \Delta\phi$, eV	$E_i - E_v^*$, eV	$E_c^* - E_i = E_i^0$, eV
HAP in $P6_3/m$	5.23	-	-	-	7.3	-	-	-
$A0 = A^0_I$ ($V_o(I)$)	5.0674	-0.1626	1.1496 ~ 1.15	3.9178	7.0497	-0.2503	1.4291 ~ 1.43	5.6206
$A0 = A^0_{II}$ ($V_o(II)$)	5.2004	-0.0296	1.3167 ~ 1.32	3.8837	7.2311	-0.0689	1.6512 ~ 1.65	5.5799
$A0 = A^0_{III}$ ($V_o(III)$)	5.1393	-0.0907	1.3811 ~ 1.38	3.7582	7.1333	-0.1667	1.685 ~ 1.68	5.4488
$D0 = D^0_I$ ($V_o(IV)$)	5.3004	+0.0704	0.4189 ~ 0.42	4.8815	7.3842	+0.0842	0.7347 ~ 0.73	6.6495

As it can be seen, regardless of the method of calculation, oxygen vacancies of the OH and PO_4 groups (in the absence of charge in these defects, ie, at $Q = 0$) form a group of energy levels (Figure 12) located close to the top of the valence band and they are donors electrons [8, 48] (electron acceptors, that is, levels with a negative charge, were not found).

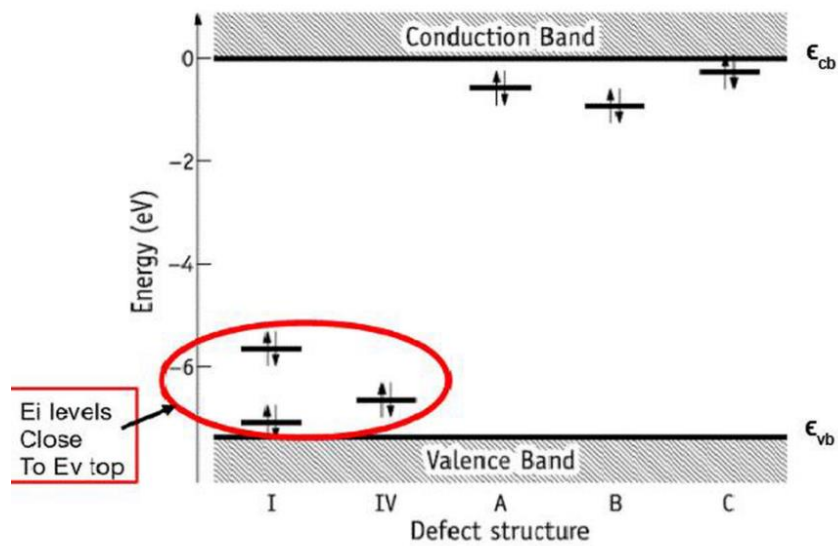


Figure 12. Kohn–Sham energy levels of neutral V_O defects in a HAP supercell at the $k = \Gamma$ point. The defect structure I is also representative of structures II and III (see text). The latter have gap states that deviate from those of $V_{O(I)}$ by less than 0.2 eV [33]. Reprinted and modified with permission from [8]. (Copyright (2019) American Chemical Society).

In this case, the shift of the levels of oxygen vacancies in the PO_4 group is ~ 1.15 – 1.65 eV upward from E_V , and for a vacancy from the OH group, ~ 0.4 – 0.7 eV, and this also corresponds to a change in the electron work function during the formation of such defects. As everyone can see, the positions of these energy levels are not very different (especially in the case of PBE calculations), although in the case of B3LYP these levels are slightly higher than E_V in the direct case. In any case, these deviations are within 1 eV.

It is also important to note that such levels are close at the top of the valence band have recently been observed in experiments on photoelectron emission spectroscopy, and the work function of a photoelectron from HAP was measured for various external influences [2, 4, 5, 53]. In addition, in [53] it was noted that such energy levels (and photoelectrons emitted from these energy levels) can arise under a number of actions on HAP samples (heating and annealing, gamma irradiation, microwave effects, and combined hydrogenation with microwave radiation). In these cases, a sufficiently large number of oxygen vacancies (also in the OH group) can be induced having the lowest energies levels measured from the top of the valence band (see Table 4 and Figure 12).

3.4.5. OH-vacancy in HAP supercell model and some general remarks

Similarly was considered vacancy of one OH group in supercell ($2 \times 2 \times 2 = 8$ unit cell) HAP model. In this case calculation with GGA approximation in hybrid functional PBE and B3LYP was performed using VASP [39] and Quantum ESPRESSO [41].

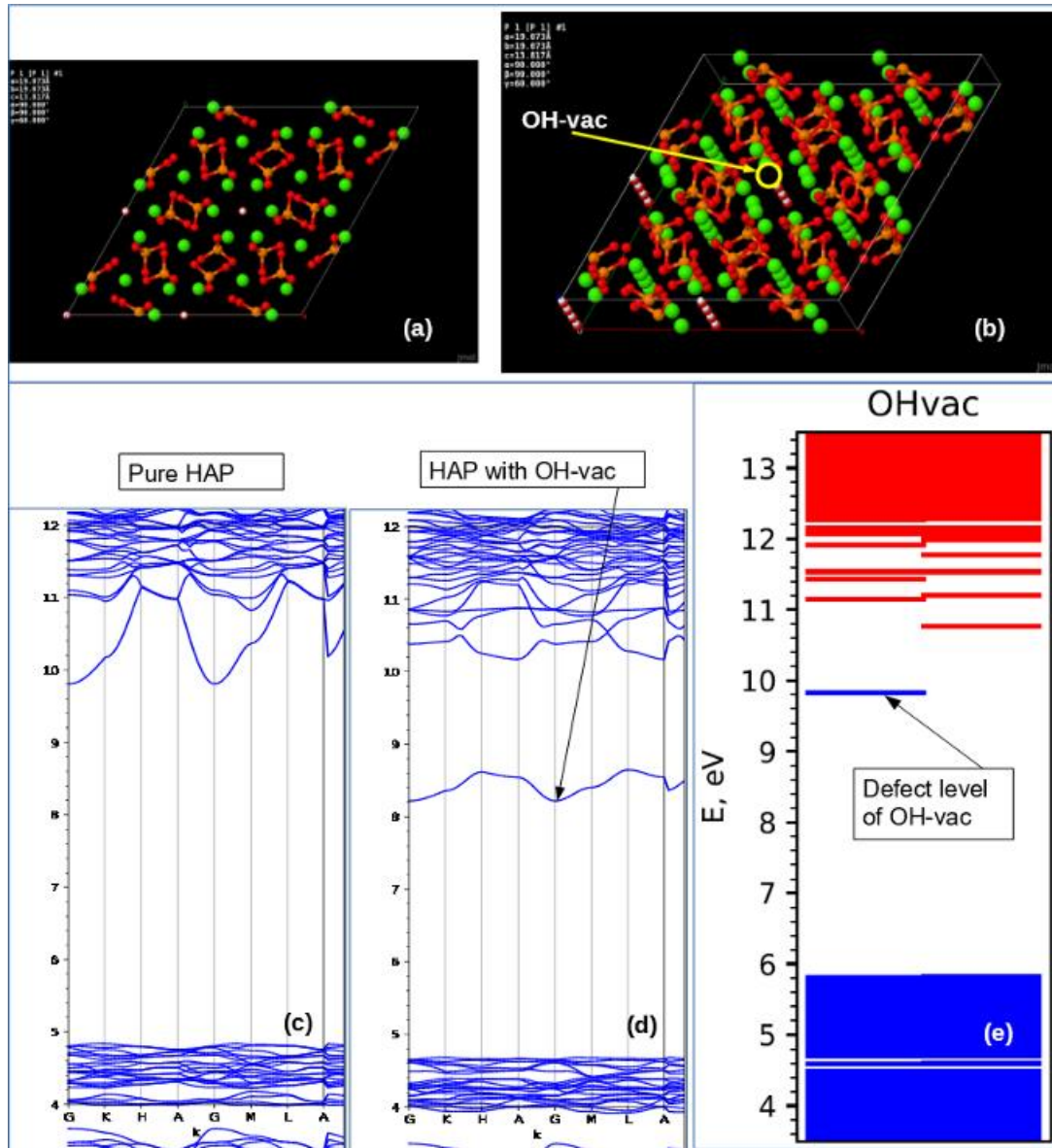


Figure 13. Model of OH-vacancy in HAP supercell: a) top view on HAP supercell; b) OH-vacancy in HAP supercell (iso projection); c) band structure of pure HAP; d) band structure of HAP with OH-vacancy computed using VASP; e) band structure of HAP with defect level from OH-vacancy computed using Quantum ESPRESSO.

Figure 13 show the results obtained in this case. After PBE optimization and B3LYP calculation using VASP energy band structure for HAP with OH-vacancy (Fig. 13b) present following data: $E_v = 0.726$ eV, $E_c = 8.066$ eV and $E_g = E_c - E_v = 8.066 - 0.726 = 7.34$ eV; the defective energy level due to OH-vacancy $E_i = 5.3586$ eV (occupied, spin up) and resulted optical gap from this energy level is equal $E_g^* = E_c - E_i = 8.066 - 5.3586 = 2.7074$ eV. This data is in line with previous data obtained using another similar method in one unit cell model.

In addition, it is important to note that the energy of formation of defects in the HAP crystal [7, 8] was considered and investigated also in the formalism with a chemical potential based on the work [52], where was described the procedure for calculating the energies of the

formation of defects in the similar study. This formalism also takes into account the formation of defects with an excess of electrons Δn_e (with respect to the neutral state) when they capable of capturing/releasing electrons from/to an electronic reservoir with a chemical potential μ_e . The results obtained in this approach allow more correct calculations taking into account the thermodynamics of the formation of a defect with a screened charge as **a quasi-particle** in a crystal [7, 8, 52]. As a result, we obtain corrections to the energies, including the energies of optical properties and transitions, which, in our opinion, turn out to be even closer to those observed experimentally. These generalized data are shown here in Table 5.

Table 5. HAP electronic properties with various vacancies Ovac {V_{O(I)}, V_{O(II)}, V_{O(III)} from PO₄, V_{O(IV)} from OH} as well as V_{OH} vacancy of OH group – in supercell model; for one unit cell model vacancies Ovac notation are the same as in Table 2.2: V_O1 (O6), V_O2 (O15), V_O3 (O30,O35), V_O4 (O24) (all energy in eV).

Unit cell	AIMPRO (LDA), Eg*	VASP-PBE (GGA), Eg*	Super-cell	PBE opt (Eg*= Ec – Ei) (GGA-supercell)		B3LYP opt (Eg*= Ec -Ei) (GGA-supercell)		Spectr.
				Kohn-Sham	Defect as quasiparticle in crystal	Kohn-Sham	Defect as quasiparticle in crystal	
Ovac from Fig.2			Ovac from Fig.10					
V_O1	3.3880 (Eg=4.734)	4.115 (Eg=5.416)	V _{O(I)}	3.9178 (Eg=5.067)	3.7052	5.6206 (Eg=7.05)	4.3375	UVA - UVB
V_O2	3.6057 (Eg=4.562)	4.034 (Eg=5.246)	V _{O(II)}	3.8837 (Eg=5.200)	3.6575	5.5799 (Eg=7.23)	4.3486	
V_O3	3.4677 (Eg=4.768)	4.184 (Eg=5.326)	V _{O(III)}	3.7582 (Eg=5.139)	3.5166	5.4488 (Eg=7.13)	4.1291	
V_O4	3.6057 (Eg=4.562)	-	-	-	-	-	-	
Aver. (O1_4)	3.52± 0.3 (Eg=4.70)	4.11±0.3 (Eg=5.34)	Aver. (I-III)	3.8532±0.2 (Eg=5.14)	3.6264±0.2	5.5498±0.2 (Eg=7.14)	4.2717±0.2	UVA
V_O of OH	5.05 (Eg=5.15)	5.45 (Eg=5.72)	V _{O(IV)}	4.8815	5.0630	6.6495	5.8563	UVC
V _{OH}	2.38-1.67 2.09 1.96 1.83 (Eg=5.49)	1.97- 1.35 1.78 1.63 1.57 (Eg=5.75)	V _{OH}	1.73	1.7372	2.9174 and 2.7074	1.7491 and 2.200	Green-Red
Eg0	4.6	5.26		5.4	5.237	7.34	6.849	

The results obtained convincingly show the primary role of defects such as oxygen vacancies and vacancy of OH group in the formation of actually observed values of the effective optical absorption and excitation bands E_g^* in various samples of HAP materials.

These works are in progress and new results will soon be obtained in this direction of calculating defects in HAP, including, in addition to the types of vacancies here considered, also other defects of the type of insertions and substitutions of some atoms in HAP unit cell lattice.

4. CONCLUSIONS

Computer studies of defects in hydroxyapatite, carried out by various methods, show their significant influence both on the structural and mechanical, as well as on the electronic and optical properties of hydroxyapatite with such defects. And this is very important for practical applications. In this review, we consider in more detail defects such as OH group vacancies and oxygen vacancies from different PO_4 groups and OH groups as well. Calculations performed by different methods showed that these vacancies significantly change, first of all, the electronic and optical properties of HAP. In this case, the vacancy of the entire OH group leads to an entire absorption band in the range $\sim 1.4 - 2.4$ eV (with several DOS peaks). It is close to the red colour of optical spectrum. However, the intensity of these DOS is small compared to the DOS of the top of the valence band. As a result, it is practically impossible to register this range of optical absorption (it is at the level of measurement errors). At the same time, an OH vacancy leads to a noticeable increase in the band gap of the order of $\sim 0.5 - 0.9$ eV. This leads to a change in the optical absorption and also a change in the work of the electron exit, which is recorded in the experiment. For example, it could be at the level $E_g \sim 5.5 - 5.75$ eV, that belong ultraviolet spectrum and which is close to the observed optical absorption of HAP samples with OH vacancies (created in them experimentally upon heating and subsequent cooling).

Oxygen vacancies have rather another optical properties. Oxygen vacancies arising from various oxygen atoms of the PO_4 group and the OH group turn out to be of different types and depend on the symmetry of the corresponding group. As it was shown in [8] that besides neutral O-vacancy here may exist charged oxygen vacancies that form not only point defects, but more complex defects - extended or bridging (in the case of a charge $Q = +2$, Figure 10). The latter reconstructing to point-like defects (at $Q = +1$ and $= 0$). This rearrangement from extended to point defects occurs with bond breaking and causes also optical absorption effects. This transition leads to spontaneous rupture of bridging $P - O - P$ or $O - H - O$ bonds at extended defects and, most likely, explains the onset of absorption at $3.4-4.0$ eV for observing photocatalysis under constant ultraviolet illumination [6, 8]. It is important that these types of structure and the stability of defects strongly depend on the charge states.

It was found that the oxygen vacancies essentially occur in such two distinct forms, either as a simple vacant oxygen site (referred to as structures I-IV, Fig. 10a), or as an oxygen atom replacing two neighbouring oxygen vacancies (bridge or extended structures named as "A-C", Fig. 10c-e) [8]. The former type of vacancies is deep donors, while the latter are shallow donors with rather low ionization energies. No acceptor states (stable negatively charged defects) were found. Vacancy structures I-IV are more stable in the neutral charge state, while bridge

structures A-C are preferred in the double plus charge state. This means that the oxygen vacancy adopts rather different configurations on samples where the Fermi energy is in the upper or the lower half of the band gap. As regarding to the neutral O-vacancy, corresponding inspection of the Kohn-Sham eigenvalues at $k = \Gamma$ confirmed that neutral oxygen vacancy defects are all donors involving the luminescence and absorption of $\sim 3.6 - 4.2$ eV [8, 36, 37].

Further development and more accurate calculation of these electronic properties and optical photoexciting and photocatalytic processes can be made also by addition correct calculations of the electron-electron correlation of the excited electron states taking into account the Frank Condon (FC) relaxation. In [36, 37] these contributions are calculated for the case of the $V_O(IV)$ vacancy in HAP $P6_3$ supercell model and their results showed that FC shift obtained has reasonable values. These investigations should be continued for all other oxygen vacancy types.

However, we must conclude that for any case, irrespective of these FC relaxation processes, the formation of the various types defects in HAP through different oxygen vacancies gives rise to an opportunity of the photo-excitation processes in the close ultraviolet (UV-C) and in the visible light region. These photo-excitation effects obviously produce the photo-catalytic activity of HAP, as well as provide the changes in the photoelectron work function and surface electric potential, that is important for implant covered by HAP. One only needs to introduce a sufficient amount of these oxygen vacancies by some external actions, such as heating/annealing, gamma-irradiation and combined hydrogenation with microwave irradiations [68]. The electron photoexcitation from additional energy levels (with $E_g^* = \sim 3.4 - 4.2$ eV), which arose due to oxygen vacancies inside the forbidden band gap, can provide this electronic and optical properties of the treated HAP samples.

ACKNOWLEDGMENTS

The study was supported by a grant Russian Science Foundation (RSF) No. 21-12-00251.

REFERENCES

- [1] B. D. Ratner, A. S. Hoffman, F.J. Schoen, J.E. Lemons, *Biomaterials Science*. 3rd ed. Oxford: Academic Press, (2013).
- [2] V. Bystrov, A. Bystrova, Yu. Dekhtyar, I. A. Khlusov, V. Pichugin, K. Prosolov, Yu. Sharkeev, Electrical functionalization and fabrication of nanostructured hydroxyapatite coatings. In: A. Iulian, eds. *Bioceramics and Biocomposites: From Research to Clinical Practice*. John Wiley & Sons, Inc., Hoboken, New Jersey, 149-190 (2019).
- [3] B. Leon, J. A. Janson, *Thin calcium phosphate coatings for medical implants*. Berlin: Springer, (2009).
- [4] K. Baltacis, V. Bystrov, A. Bystrova, Yu. Dekhtyar, T. Freivalds, J. Raines, K. Rozenberga, H. Sorokins, M. Zeidaks, Physical fundamentals of biomaterials surface electrical functionalization. [Materials, Special Issue "Recent Advances in Biocoatings", 13 \(20\), 4575 \(2020\)](#).
- [5] V.S. Bystrov, J. Coutinho, A.V. Bystrova, Yu.D. Dekhtyar, R.C. Pullar, A. Poronin, E. Palcevskis, A. Dindune, B. Alkan, C. Durucan, Computational study of the hydroxyapatite structures, properties and defects, [J. Phys. D Appl. Phys. 48, 195302 \(2015\)](#).
- [6] V.S. Bystrov, C. Piccirillo, D.M. Tobaldi, P.M.L. Castro, J. Coutinho, S. Kopyl, R.C. Pullar, Oxygen vacancies, the optical band gap (E_g) and photocatalysis of hydroxyapatite:

- comparing modelling with measured data, [Applied Catalysis B: Environmental](#), **196**, 100-107 (2016).
- [7] L.A. Avakyan, E.V. Paramonova, J. Coutinho, S. Öberg, V.S. Bystrov, L.A. Bugaev, Optoelectronics and defect levels in hydroxyapatite by first-principles, [J. Chem. Phys.](#) **148**, 154706 (2018).
- [8] V. S. Bystrov, L. A. Avakyan, E. V. Paramonova, J. Coutinho, Sub-Band Gap Absorption Mechanisms Involving Oxygen Vacancies in Hydroxyapatite, [J. Chem. Phys.C](#). **123** (8), 4856-4865 (2019).
- [9] V. S. Bystrov, Computational Studies of the Hydroxyapatite Nanostructures, Peculiarities and Properties, [Math. Biol. Bioinform.](#) **12** (1), 14-54 (2017).
- [10] J. Elliott, *Structure and Chemistry of the Apatites and Other Calcium Orthophosphates, Studies in Inorganic Chemistry*, p. 404, Elsevier Science, Amsterdam, (2013).
- [11] J. M. Hughes, M. Cameron, K. D. Crowley, Structural variations in natural F, OH, and Cl apatites. [Am. Mineral.](#), **74**, 870-876 (1989).
- [12] G. Ma, X. Y. Liu, Hydroxyapatite: hexagonal or monoclinic? [Cryst. Growth Des.](#), **9**, 2991-2994 (2009).
- [13] M. I. Kay, R. A. Young, A. S. Posner, Crystal structure of hydroxyapatite, [Nature](#) **204**, 1050 (1964).
- [14] N. Hitmi, C. LaCabanne, R. A. Young, OH- dipole reorientability in hydroxyapatites: effect of tunnel size. [J. Phys. Chem. Solids.](#), **47** (6), 533-546 (1986).
- [15] N. Hitmi, C. LaCabanne, R. A. Young, Oh- reorientability in hydroxyapatites: Effect of F- and Cl-. [J. Phys. Chem. Solids](#), **49** (5), 541-550 (1988).
- [16] S. Nakamura, H. Takeda, K. Yamashita, Proton transport polarization and depolarization of hydroxyapatite ceramics, [J. Appl. Phys.](#) **89** (10), 5386 (2001).
- [17] N. Horiuchi, M. Nakamura, A. Nagai, K. Katayama, K. Yamashita, Proton conduction related electrical dipole and space charge polarization in hydroxyapatite, [J. Appl. Phys.](#), **112**, 074901 (2012).
- [18] S. A. M. Tofail, D. Haverty, K. T. Stanton, J. B. McMonagle, Structural order and dielectric behaviour of hydroxyapatite, [Ferroelectrics](#), **319**, 117-123 (2005).
- [19] K. Matsunaga, A. Kuwabara, First-principles study of vacancy formation in hydroxyapatite, [Phys. Rev. B: Condens. Matter Mater. Phys.](#), **75**, 014102 (2007).
- [20] D. Aronov, M. Chaikina, J. Haddad, A. Karlov, G. Mezinskis, L. Oster, I. Pavlovskaya, G. Rosenman, Electronic states spectroscopy of Hydroxyapatite ceramics, [J. Mater. Sci.: Mater. Med.](#) **18**, 865-870 (2007).
- [21] H. Nishikawa, A high active type of hydroxyapatite for photocatalytic decomposition of dimethyl sulfide under UV irradiation, [J. Mol. Catal. A: Chem.](#), **207**, 149-153 (2004).
- [22] H. Nishikawa, Photo-induced catalytic activity of hydroxyapatite based on photo-excitation, [Phosphorus Res. Bull.](#), **21**, 97-102 (2007).
- [23] A. R. Silin, A. I. Trukhin. *Point defects and elementary excitations in crystalline and glassy SiO₂*, Riga, Zinatne, 244 p. (1985) (in Russian).
- [24] E.V. Paramonova, L.A. Avakyan, V.S.Bystrov, J. Coutinho, Hybrid density functional study of iron impurities in hydroxyapatite. In: *4th International Conference on Nanomaterials Science and Mechanical Engineering (ICNMSME-2021). Book of Abstracts*. UA Editora, Universidade de Aveiro, Aveiro, 115 (2021).
- [25] E.V. Paramonova, L.A. Avakyan, V.S.Bystrov, J. Coutinho, Magnetic iron substitutions in hydroxyapatite: density functional study. In: *2nd International Conference on Nanomaterials Science and Mechanical Engineering. Book of Abstracts. (University of Aveiro, Portugal, July 9-12, 2019)*. UA Editora, Universidade de Aveiro, Aveiro, 67 (2019).
- [26] N. V. Bulina, M. V. Chaikina, I. Yu Prosanov, Mechanochemical Synthesis of Sr-Substituted Hydroxyapatite, [Inorganic Materials](#), **54** (8), 820-825 (2018).
- [27] M. Šupova, Substituted hydroxyapatites for biomedical applications: a review, [Ceram. Int.](#), **41**, 9203-9231 (2015).

- [28] C. Capuccini, P. Torricelli, E. Boanini, M. Gazzano, R. Giardino, A. Bigi, Interaction of Sr-doped hydroxyapatite nanocrystals with osteoclast and osteoblast-like cells, *J. Biomed. Mater. Res., Part A*, **89**, 594–600 (2009).
- [29] V.S. Bystrov, E.V. Paramonova, A.V. Bystrova, L.A. Avakyan, J. Coutinho, S.V. Makarova, N.V. Bulina, Structural and physical properties of Sr-substituted hydroxyapatite: modeling and experiments. In: *4th International Conference on Nanomaterials Science and Mechanical Engineering (ICNMSME-2021). Book of Abstracts. (University of Aveiro, Portugal, July 6, 2021)*. UA Editora, Universidade de Aveiro, Aveiro, 82-83 (2021).
- [30] L. Calderin, M. J. Stott, A. Rubio, Electronic and crystallographic structure of apatites. *Phys. Rev. B: Condens. Matter Mater. Phys.*, **67**, 134106 (2003).
- [31] P. Rulis, L. Ouyang, W. Y. Ching, Electronic structure and bonding in calcium apatite crystals: Hydroxyapatite, fluorapatite, chlorapatite, and bromapatite. *Phys. Rev. B: Condens. Matter Mater. Phys.*, **70**, 155104 (2004).
- [32] P. Rulis, H. Yao, L. Ouyang, W. Y. Ching, Electronic structure, bonding, charge distribution, and x-ray absorption spectra of the (001) surfaces of fluorapatite and hydroxyapatite from first principles. *Phys. Rev. B: Condens. Matter Mater. Phys.*, **76**, 245410 (2007).
- [33] D. Haverty, S. A. M. Tofail, K. T. Stanton, J. B. McMonagle, Structure and stability of hydroxyapatite: density functional calculation and Rietveld analysis. *Phys. Rev. B: Condens. Matter Mater. Phys.*, **71**, 094103 (2005).
- [34] A. Slepko, A. A. Demkov, First-principles study of the biomineral hydroxyapatite. *Phys. Rev. B: Condens. Matter Mater. Phys.*, **84**, 134108 (2011).
- [35] M. Corno, C. Busco, B. Civalleri, and P. Ugliengo, Periodic *ab initio* study of structural and vibrational features of hexagonal hydroxyapatite $\text{Ca}_{10}(\text{PO}_4)_6(\text{OH})_2$, *Phys. Chem. Chem. Phys.* **8**, 2464 (2006).
- [36] V. S. Bystrov, Jose Coutinho, L. A. Avakyan, A.V. Bystrova, E.V. Paramonova, Piezoelectric, ferroelectric, optoelectronic phenomena in hydroxyapatite by first-principles and with various defects, *Nanomaterials Science & Engineering* **1** (1), 10-21 (2019).
- [37] V. S. Bystrov, J. Coutinho, L. A. Avakyan, A. V. Bystrova, E. V. Paramonova, Piezoelectric, ferroelectric, and optoelectronic phenomena in hydroxyapatite with various defect levels, *Ferroelectrics* **550**, 45-55 (2020).
- [38] AIMPRO, (2010). [<http://aimpro.ncl.ac.uk/>] (Accessed February 2016).
- [39] VASP (Vienna Ab initio Simulation Package), [<https://www.vasp.at/>] (Accessed July 2019).
- [40] HyperChem:Tools for Molecular modeling (release 8). Gainesville: Hypercube, Inc. 2002.
- [41] Quatum ESPRESSO, [<https://www.quantum-espresso.org/>] (Accessed July 2021)
- [42] P. R. Britney, R. Jones, LDA Calculations Using a Basis of Gaussian Orbitals. *Phys. Status Solidi B: Basic Res.*, **217**, 131–171 (2000).
- [43] P. R. Briddon, M. J. Rayson, Accurate Kohn–Sham DFT with the Speed of Tight Binding: Current Techniques and Future Directions in Materials Modeling. *Phys. Status Solidi B.*, **248** (6), 1309–1318 (2011).
- [44] R. M. Martin, L. Reining, D. M. Ceperley, *Interacting Electrons: Theory and Computational Approaches*. Cambridge: Cambridge University Press, (2016).
- [45] G. Kresse, J. Hafner, *Ab initio* molecular-dynamics simulation of the liquid-metal-amorphous-semiconductor transition in germanium, *Phys. Rev. B: Condens. Matter Mater. Phys.*, **49**, 14251–14269 (1994).
- [46] G. Kresse, J. Furthmüller, Efficient iterative schemes for *ab initio* total-energy calculations using a plane-wave basis set. *Phys. Rev. B: Condens. Matter Mater. Phys.*, **54**, 11169–11186 (1996).
- [47] G. Kresse, D. Joubert, From ultrasoft pseudopotentials to the projector augmented-wave method. *Phys. Rev. B: Condens. Matter Mater. Phys.*, **59**, 1758–1775 (1999).

- [48] J. P. Perdew, K. Burke, M. Ernzerhof, Generalized Gradient Approximation Made Simple. [*Phys. Rev. Lett.*, **77**, 3865–3868 \(1996\).](#)
- [49] C. Lee, W. Yang, R. G. Parr, Development of the Colle-Salvetti correlation-energy formula into a functional of the electron density. [*Phys. Rev. B: Condens. Matter Mater. Phys.*, **37**, 785–789 \(1988\).](#)
- [50] A. D. Becke, A new mixing of Hartree-Fock and local density functional theories. [*J. Chem. Phys.*, **98**, 1372–1377 \(1993\).](#)
- [51] P. E. Blöchl, Projector augmented-wave method. [*Phys. Rev. B: Condens. Matter Mater. Phys.*, **50**, 17953–17979 \(1994\).](#)
- [52] G.-X. Qian, R. M. Martin, D. J. Chadi, First-principles study of the atomic reconstructions and energies of Ga- and As-stabilized GaAs(100) surfaces, [*Phys. Rev. B: Condens. Matter Mater. Phys.* **38**, 7649-7663 \(1988\).](#)
- [53] A. V. Bystrova, Yu. Dekhtyar, A. I. Popov, J. Coutinho, V.S. Bystrov, Modified Hydroxyapatite Structure and Properties: Modeling and Synchrotron Data Analysis of Modified Hydroxyapatite Structure, [*Ferroelectrics* **475**\(1\), 135-147 \(2015\).](#)
- [54] J. Heyd, G. E. Scuseria, and M. Ernzerhof, Hybrid functionals based on a screened Coulomb potential, [*J. Chem. Phys.*, **118**, 8207 \(2003\).](#)
- [55] N. V. Bulina, S. V. Makarova, I. Yu. Prosanov, O. B. Vinokurova, N. Z. Lyakhov, Structure and thermal stability of fluorhydroxyapatite and fluorapatite obtained by mechanochemical method, [*Journal of Solid State Chemistry*, **282**, 121076 \(2020\).](#)
- [56] M.A. Pogosova, D.I. Provotorov, A.A. Eliseev, M. Jansen, P.E. Kazin, Synthesis and characterization of the Bi-for-Ca substituted copper-based apatite pigments, [*Dyes and Pigments*, **113**, 96-101 \(2015\).](#)
- [57] S. Gomes, G. Renaudin, A. Mesbah, E. Jallot, C. Bonhomme, F. Babonneau, J. M. Nedelec, Thorough analysis of silicon substitution in biphasic calcium phosphate bioceramics: a multi-technique study. [*Acta Biomater.* **6** \(8\), 3264-74 \(2010\).](#)
- [58] J. L. Katz, K. Ukraincik, On the anisotropic elastic properties of hydroxyapatite, [*Journal of Biomechanics*, **4** \(9\), 221-227 \(1971\).](#) [https://doi.org/10.1016/0021-9290\(71\)90007-8](https://doi.org/10.1016/0021-9290(71)90007-8).
- [59] Gilmore, R.S., Katz, J.L. Elastic properties of apatites, [*J. Mater. Sci.* **17**, 1131–1141 \(1982\).](#)
- [60] J. Paier, M. Marsman, and G. Kresse, Why does the B3LYP hybrid functional fail for metals? [*J. Chem. Phys.*, **127**, 024103 \(2007\).](#)
- [61] F. Birch, Finite Elastic Strain of Cubic Crystals, [*Phys. Rev.* **71**, 809 \(1947\).](#)
- [62] A. A. Mostofi, J. R. Yates, G. Pizzi, Y.-S. Lee, I. Souza, D. Vanderbilt, and N. Marzari, An updated version of wannier90: A tool for obtaining maximally-localised Wannier functions, [*Comput. Phys. Commun.*, **185**, 2309 \(2014\).](#)
- [63] A. J. Garza and G. E. Scuseria, Predicting Band Gaps with Hybrid Density Functionals, [*J. Phys. Chem. Lett.*, **7**, 4165 \(2016\).](#)
- [64] D. Prendergast, J. C. Grossman, and G. Galli, The electronic structure of liquid water within density-functional theory, [*J. Chem. Phys.*, **123**, 014501 \(2005\).](#)
- [65] E. A. Engel, B. Monserrat, and R. J. Needs, Vibrational renormalisation of the electronic band gap in hexagonal and cubic ice, [*J. Chem. Phys.*, **143**, 244708 \(2015\).](#)
- [66] F. Salehli, A. O. Aydin, D. Chovan, S. Kopyl, V. Bystrov, D. Thompson, S. A. M. Tofail, A. Kholkin, Nanoconfined water governs polarization-related properties of self-assembled peptide nanotubes, [*Nano Select*, **2**, 817–829 \(2021\).](#)
- [67] V. Bystrov, J. Coutinho J., P. Zelenovskiy, A. Nuraeva, S. Kopyl, O. Zhulyabina. V. Tverdislov, Structures and properties of the self-assembling diphenylalanine peptide nanotubes containing water molecules: modeling and data analysis, [*Nanomaterials*, **10** \(10\), 1999 \(2020\).](#)
- [68] V.S. Bystrov, E.V. Paramonova, Yu.D. Dekhtyar, A. V. Bystrova, R.C. Pullar, S. Kopyl, D.M. Tobaldi, C. Piccirillo, L.A. Avakyan, J. Coutinho, Surface modified hydroxyapatites with various functionalized nanostructures: Computational studies of the vacancies in HAp. [*Ferroelectrics*, **509**, 105 \(2017\).](#)



Title

4th International Conference on Nanomaterials Science
and Mechanical Engineering
Conference proceedings

Editors

Igor Bdikin
Gil Alberto Batista Gonçalves
Gonzalo Guillermo Otero Irueta
Raul Simões

Publisher

UA Editora
Universidade de Aveiro

1st edition – September 2021

ISBN

978-972-789-707-0

